THESIS FOR THE DEGREE OF DOCTOR OF PHILOSOPHY IN SOLID AND STRUCTURAL MECHANICS

Macroscale Modelling of 3D-Woven Composites: Inelasticity, Progressive Damage and Final Failure

CAROLYN ODDY

Department of Industrial and Materials Science
Division of Material and Computational Mechanics
CHALMERS UNIVERSITY OF TECHNOLOGY

Göteborg, Sweden 2022

Macroscale Modelling of 3D-Woven Composites: Inelasticity, Progressive Damage and Final Failure
CAROLYN ODDY
ISBN 978-91-7905-683-4

Doktorsavhandlingar vid Chalmers tekniska högskola
Ny serie nr. 5149
ISSN 0346-718X
Department of Industrial and Materials Science
Division of Material and Computational Mechanics
Chalmers University of Technology
SE-412 96 Göteborg
Sweden
Telephone: +46 (0)31-772 1000

Cover:
Comparing experimental and simulated shear strain distributions in an Iosipescu test.

Chalmers Reproservice
Göteborg, Sweden 2022

Macroscale Modelling of 3D-Woven Composites: Inelasticity, Progressive Damage and Final Failure

CAROLYN ODDY
Department of Industrial and Materials Science
Division of Material and Computational Mechanics
Chalmers University of Technology

Abstract

Composites with 3D-woven reinforcement have been slowly making their way into different industrial applications. The interlacement of yarns, not only in-plane but also through-thickness, means that in many applications 3D-woven composites can outperform their laminated counterparts. In particular, this includes increased out-of-plane stiffness and strength, damage tolerance and specific energy absorption properties. The widespread adoption of 3D-woven composites in industry however, requires the development of accurate and efficient computational models that can capture the material behaviour.

In terms of computational efficiency, the most promising choice is to treat the material as a homogeneous and anisotropic solid. This is referred to as a macroscale model. Developing a macroscale model, which can predict how 3D-woven composites deform and eventually fail, is the main focus of this work. Particular attention is given to predicting the relevant non-linear behaviours that lead to energy absorption.

A framework for modelling the mechanical response of 3D-woven composites on the macroscale is presented. The proposed framework decomposes the stress and strain tensors into two main parts motivated by the material architecture. This allows for a convenient separation of the modelling of the shear behaviour from the modelling of the behaviour along each of the reinforcement directions. In particular, this division allows for a straightforward addition and modification of various non-linear phenomena observed in 3D-woven composites. As a next step, material modelling approaches are considered and added to the framework in order to capture these non-linear phenomena. This includes the use of a viscoelastic model as well as a combined elasto-plastic and continuum damage model to capture the development of permanent deformations and stiffness reduction mechanisms. Finally, an anisotropic phase-field model extension is developed in order to induce local softening and failure in a way which does not induce spurious mesh-dependencies in finite element analyses. The model predictions are compared to experimental tests and show good agreement.

The aim has been to develop a model that allows the constitutive relations to be identified directly from uniaxial cyclic stress-strain tests without the need for complex calibration schemes. However, characterising the out-of-plane behaviour is not trivial. Therefore, the current work also explores the use of high-fidelity mesoscale models as an additional source of data for model calibration and validation.

Keywords: 3D-woven composites, Anisotropy, Inelasticity, Damage, Phase-field, Failure

Preface

Nothing is ever accomplished by a single individual, and this thesis is no exception. There are so many thank yous that need to be given for all of the help and support that went into making this thesis. Starting from the beginning, the main reason why I ended up at Chalmers goes back more than thirty years. My parents jumped on the chance to spend a few months living and working in Luleå, a small town in northern Sweden. The connections and friendships that they made, gave me the opportunity to move from Canada to Sweden after finishing high school. What I really thought would be one year abroad quickly turned into a three year Bachelors degree at Linnéuniversitetet in Växjö, a two years Masters degree at Chalmers and the start of five years as a PhD student.

I would like to thank my brother, sister and parents for their support and help along the way. My mum in particular is a huge part of who I am and what I've accomplished. I would also like to express my thanks to my bonuspappa Lennart, who not only welcomed me to Sweden but who is also the main reason I was able to manoeuvre from math to the Applied Mechanics Programme at Chalmers.

I had the pleasure of being involved in two projects during my PhD. I would like to thank the FiberDuk project partners and in particular my co-authors Tomas Ekermann, Stefan Hallström and Fredrik Stig. Your knowledge and capabilities have made this work possible. I am also fortunate enough to have had the opportunity to travel for a study visit to the Bristol Composites Institute as part of the VIRTEST-3D project. Many thanks to Ioannis Topalidis, Stephen Hallett and most importantly Bassam El-Said for welcoming me so warmly. The FiberDuk project was supported by the Swedish Energy Agency under contract 2016-008713, while the VIRTEST-3D project was funded by Chalmers' Area of Advance in Materials Science under contract 2021-0037. Computational resources at C3SE, provided by the Swedish National Infrastructure for Computing (SNIC) were also used. All are gratefully acknowledged.

I would like to thank all of my teachers, past and present. Most importantly though, I would like to thank my supervisors Martin Fagerström and Magnus Ekh for their patience, support and guidance. You both have a gift for making sure to develop the individual behind the research. To old and new friends, especially those at the division, thank you. Being able to eat lunch, have a coffee, drop by your offices and laugh everyday is really something special. Finally, I would like to thank Roeland, who's been by my side for the past eight years. You know just how much of this is because of you.

Thesis

This thesis consists of an extended summary (Part I) and the following appended papers (Part II):

Paper A C. Oddy, T. Ekermann, M. Ekh, M. Fagerström, S. Hallström and F. Stig. Predicting damage initiation in 3D fibre-reinforced composites: The case for strain-based criteria. *Composite Structures* 230 (2019), 111336.

Paper B C. Oddy, T. Ekermann, M. Ekh, M. Fagerström, and S. Hallström. A framework for macroscale modelling of inelastic deformations in 3D-woven composites. *Mechanics of Materials* 160 (2021), 103856.

Paper C C. Oddy, M. Ekh, and M. Fagerström. Macroscale modelling of 3D-woven composites: Elasto-plasticity and progressive damage. *International Journal of Solids and Structures* 250 (2022), 111696.

Paper D C. Oddy, M. Ekh, and M. Fagerström. Phase-field modelling of failure in 3D-woven composites. *To be submitted.*

Paper E C. Oddy, I. Topalidis, B. El Said, M. Ekh, S. Hallett and M. Fagerström. Calibrating macroscale models of 3D-woven composites: complementing experimental testing with high fidelity mesoscale models. *In: Proceedings of the 20th European Conference on Composite Materials ECCM20 (Lausanne, Switzerland, 26-30 June 2022.)*

Contents

Part I
Extended Summary

1 Introduction

Composite preforms with three-dimensional (3D) reinforcements first started appearing in the 1970s. As discussed by Tong et al. [1], their development was driven by a need for reduced fabrication costs, increased through-thickness mechanical properties and improved impact damage tolerance. Currently, the reported benefits of 3D-woven composites are broad and encompass aspects relating to not only improved material integrity, but also benefits in manufacturing and in design flexibility.

When it comes to the material's integrity, Stig and Hallström [2] have shown that the inherent nature of the through-thickness reinforcements suppresses delamination. This in turn increases out-of-plane strength and stiffness properties when compared to traditional laminated composites. Composites with 3D-woven reinforcements have also shown increased fracture toughness and damage tolerance, see Bogdanovich [3]. Furthermore, both Khokar et al. [4] and Kazemahvazi et al. [5] have demonstrated promising energy absorption capabilities. Khokar et al. in particular, compared a 3D-woven carbon fibre reinforced polymer (CFRP) I-beam against a steel I-beam with the same geometry under four-point bending. The results, illustrated in Figure 1.1, show that the specific energy absorption (i.e. energy per unit mass) of the CFRP I-beam was up to three times higher than its steel counterpart. It also shows that the through-thickness reinforcements allowed for a stable and progressive damage growth in a quasi-ductile manner.

Along with improved material performance over traditional laminated composites, there are additional benefits to the use of 3D-woven composites. One important advantage is that complex woven preforms can be produced in a near net-shape. As discussed by Mouritz et al. [6], this can reduce material waste, the need for joining and machining and

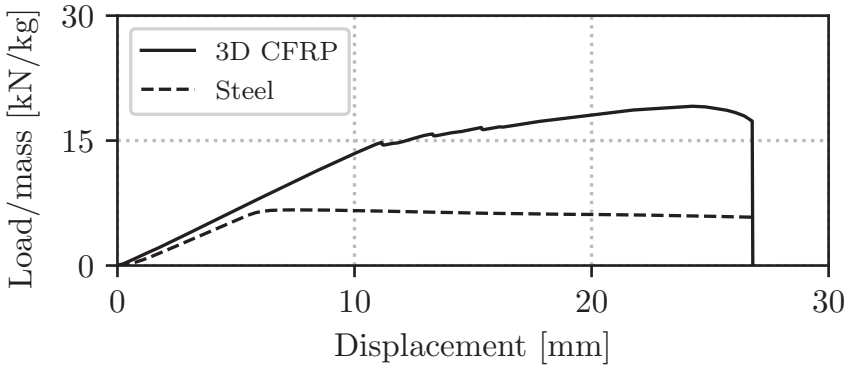

Figure 1.1: *Specific load - displacement curves of a 3D-CFRP and Steel I-Beam with the same dimensions under four point bending. From Khokar et al. [4].*

the amount of material handling during lay-up. The flexibility of the weaving process also creates an impressive design space. According to Whitney and Chou [7] many weave parameters can be changed, which affects the overall behaviour of the material. This includes among other things: the fibre type, the yarn size, the tension in the yarns, the tightness of the yarns and the number of warp and weft yarns per unit width and length. Further, it is possible to produce preforms with various cross-sectional shapes whose weave patterns changes from one part of the structure to the next. When done strategically, it is possible to truly optimise a component to its desired use.

With all of their potential benefits, 3D-woven composites are slowly making their appearance across multiple industries. Within the aerospace industry for example, 3D-woven composites are used as fan blades in engines and in the landing gear braces for the Boeing 787, cf. DeLuycker et al. [8] and Nathan [9]. Their use has also been reported by Tong et al. [1] within marine, civil infrastructure and medical applications. The potential for further applications within the automotive industry also exist, one possibility being in intrusion protection systems. However, in order to further drive the use of 3D-woven composites in industry, efficient modelling techniques are required. The goal of this work is to therefore develop a macroscale phenomenologically based model to predict how 3D-woven composites behave and eventually fail under mechanical loads. This overall goal will lead to the five research objectives identified in Section 1.2.

1.1 Classification of 3D-Woven Composites and Considered Materials

Many different types of fibre-reinforced composites exist, each having their own benefits and drawbacks. This includes among others, composites with unidirectional (UD) fibre-reinforcements, non-crimp fabrics, 2D-woven textiles and 3D fibre-reinforcements. In the most broad sense, 3D fibre-reinforced composites are characterised by the use of through-thickness reinforcements that improve out-of-plane properties. According to Tong et al. [1], 3D fibre-reinforced composites can be classified into six main groups, based on the manufacturing of their preforms. These six preform groups are: braided, knit, stitched, z-pinned, non-woven and, finally, woven. As the title of this thesis suggests, 3D-woven composites are the main focus of the present study.

Generally speaking, 3D-woven composites are characterised by the intertwining of reinforcement yarns in 3D-space. In particular, this means that unlike their UD and 2D-woven counterparts, 3D-woven composites have reinforcement yarns that run through the thickness of the material. The way in which the through-thickness yarns are interlaced in the woven substructure can however vary. This variation means that 3D-woven composites are usually further subdivided into different groups. As discussed by Gereke and Cherif [10], one strategy is to classify them as layer-to-layer angle interlocks, through-the-thickness angle interlocks and orthogonal weaves. These groups are illustrated in Figure 1.2.

Different terminology is used to refer to each yarn group. Warp yarns (illustrated in blue in Figure 1.2) indicate the main weaving direction of the material. Layer-to-layer angle interlocks shown in Figure 1.2a are classified by warp yarns being woven through multiple layers of what are referred to as weft yarns (shown in red). The weft yarns

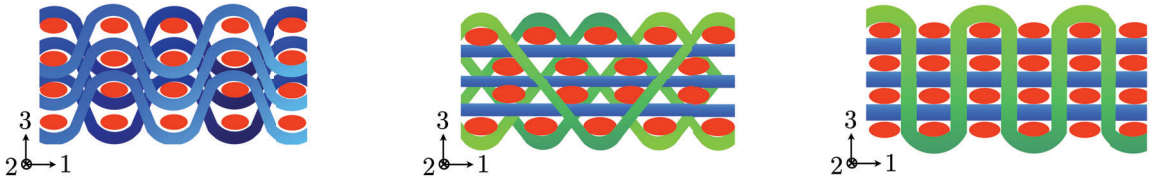

(a) *Layer-to-layer angle interlock* (b) *Through-the-thickness angle interlock* (c) *Orthogonal weave*

Figure 1.2: *Illustration of 3D-woven preform types.*

generally run perpendicularly to the nominal direction of the warp yarns. In through-the-thickness angle interlocks, illustrated in Figure 1.2b, a third reinforcement direction is introduced. What are usually referred to as binder yarns (illustrated in green) are woven in a V-shape through multiple layers of warp and weft yarns. Finally, orthogonal weaves (Figure 1.2c) once again have a third yarn direction running vertically through layers of warp and weft yarns. This third yarn direction is referred to as binder, and in some cases, vertical weft yarns.

Note that from this point forward the reinforcement directions will be indicated using a 123-coordinate system. As shown in Figure 1.2, the nominal orientation of the warp yarns, horizontal weft yarns and vertical weft yarns (or through thickness direction in the layer-to-layer or angle interlock) are denoted using 1,2 and 3, respectively.

Three different 3D-woven composite materials will be introduced and discussed throughout this work. They are:

1. **FiberDuk**: *An orthogonal 3D-woven glass fibre reinforced epoxy composite.* The **FiberDuk** material is an orthogonal woven composite manufactured by Biteam AB. It should be highlighted, that Biteam's preforms are truly woven in three-dimensions. As shown in Figure 1.3a, warp, horizontal weft and vertical weft yarns all interlace one another in a grid like pattern. A number of images of the test coupons are also shown in Figure 1.3a. This is a highly unbalanced weave, meaning that the properties in the warp and weft directions vary drastically. Further, the size of the representative unit cell is also given in Figure 1.3a. This 3D-woven composite was manufactured as part of the FiberDuk (Ductile fibre reinforced composites) project funded by the Swedish Energy Agency. The main project aim was to gain a better understanding of the failure mechanisms of 3D-woven composites and to develop an efficient and industrially applicable computational model to describe how they deform and eventually fail. All experimental testing was carried out by project partners at KTH Royal Institute of Technology, while model development took place at Chalmers University of Technology. The FiberDuk material is the primary 3D-woven composite that is analysed in **Paper B**, **Paper C** and **Paper D**.

2. **CERFAC**: *An orthogonal 3D-woven carbon fibre reinforced epoxy composite.* This weave was also manufactured by Biteam AB using an orthogonal weaving pattern. This material was woven and tested as part of the CERFAC (Cost Effective Reinforcement of Fastener Areas in Composites) project funded by the European

Commission. More information can be found in Stig [11]. As part of the CERFAC project, they developed a methodology to generate mesoscale models of the weave architecture to predict (among other things) the elastic properties of 3D-woven materials. A mesoscale model of this plane weave is used in **Paper A**. It has the same weave pattern as the **FiberDuk** material, however is woven using carbon fibre yarns instead of glass fibre.

3. **BAM**: *A layer-to-layer 3D-woven carbon fibre composite.* The BAM layer-to-layer material is relatively balanced, meaning that the warp and weft directions show comparatively similar material properties. Again, the size of the representative unit cell along with an image of tensile specimens are given in Figure 1.3b. This weave was first developed as part of the BAM (Breakthrough Aerospace Materials) project. The BAM project was funded by InnovateUK. It sought to enhance many aspects related to 3D-woven composites, from design to manufacturing. This resulted in the development of a high fidelity mesoscale model which considers the impregnated yarns, the matrix pockets that surround them as well as the inelastic and stiffness degrading phenomena they both exhibit. More recently, this material and its mesoscale model have been used in a project given the name **VIRTEST-3D** (VIRtual TESTing of 3D-Woven Composites: From Weaving Architecture to Component Performance). The project is primarily funded by the Chalmers Area of Advance in Materials Science. VIRTEST-3D involved project partners from both the Bristol Composites Institute as well as Chalmers University of Technology. The BAM layer-o-layer material was analysed in **Paper E**.

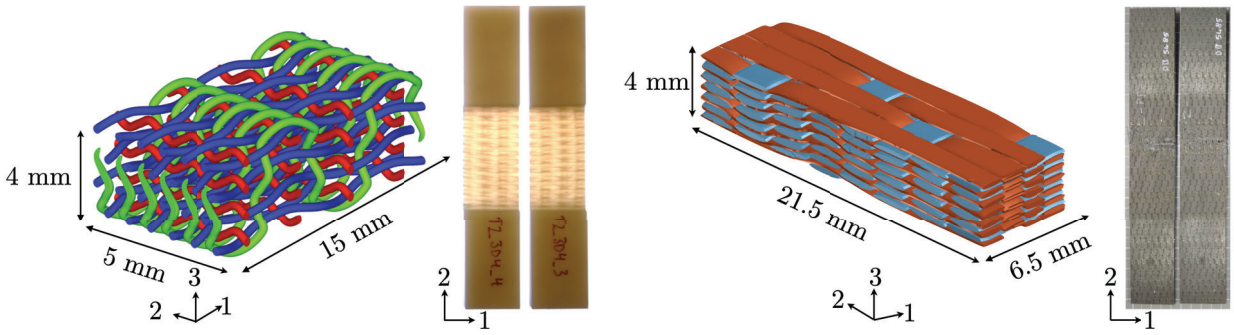

(a) *FiberDuk.* (b) *BAM.*

Figure 1.3: *Weave architecture and tensile test coupons from different from different material systems.*

1.2 Research Scope

The substructure of 3D-woven composites creates a material which is hierarchical in nature. Typically, for these materials, three different length scales can be distinguished. They are illustrated in Figure 1.4. The finest scale relevant for a continuum model, the microscale, describes the impregnated yarns in terms of single fibre filaments embedded in a matrix material. The mesoscale on the other hand, describes the woven architecture of the yarns and the matrix pockets that surround them. Finally, the macroscale describes the material on a structural level as a homogeneous (but anisotropic) solid.

Explicitly considering the micro and/or mesoscale allows for the careful consideration of important subscale behaviours. This has one main drawback - computational cost. Modelling large structural components with so much detail is simply not computationally feasible for the time being. Due to their computational efficiency and industrial applicability, this research work will take on a macroscale view of 3D-woven composites. **The overall research objectives are summarised as follows:**

1. **Develop a phenomenologically based macroscale model to predict how 3D-woven composites deform and eventually fail under mechanical loading.**

2. **Determine appropriate material modelling techniques such that the macroscale model can predict the inelastic processes that lead to energy absorption.**

3. **Propose calibration schemes of the models with clear guidelines, that link material parameters to distinct experimental test.**

4. **Implement the proposed model in a commercial finite element (FE) software in order to facilitate knowledge transfer to industry.**

5. **Validate the model against experimental results.**

The term phenomenological here gives an important indication to how the macroscale model has been developed. McMullin [12] gives a thorough discussion and differentiates

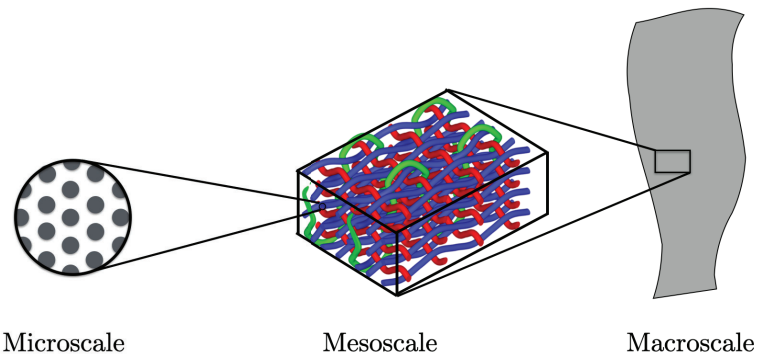

Figure 1.4: *Illustration of the micro, meso and macroscales.*

between empirical, phenomenological and physically-based modelling theories. Paraphrasing his discussion, phenomenological models aim to capture the phenomena leading to certain behaviours. In their purest form phenomenological models, give no description or regard to what subscale, physical mechanisms are behind each phenomenon.

The development of the considered phenomenological macroscale model has taken place in steps for three main regions. These regions can be motivated and visualised by an idealised force-displacement curve for a component test shown in Figure 1.5. This figure introduces the terminology that will be referred to from this point forward. It is also important to distinguish between the behaviour shown at a local material point (stress-strain) vs. the global structure (force-displacement).

The first region is characterised by linear (but possibly anisotropic) elastic behaviour. Following this, in region II, the force-displacement curve begins to show a non-linear response. Experimental results show that this non-linear behaviour is due to a combination of stiffness degrading as well as permanent deformation developing mechanisms. This means that for model development damage and inelasticity must be considered. Finally, at some point locally in the structure, failure will initiate[1]. This is the start of region III. It is however important to consider that for 3D-woven composites, this does not necessarily mean that the component has failed. On the material point level, it is therefore also important to develop a model which can show a complete degradation of the material properties. This eventually leads to softening (i.e. a load drop) of the global component behaviour and final failure of the component.

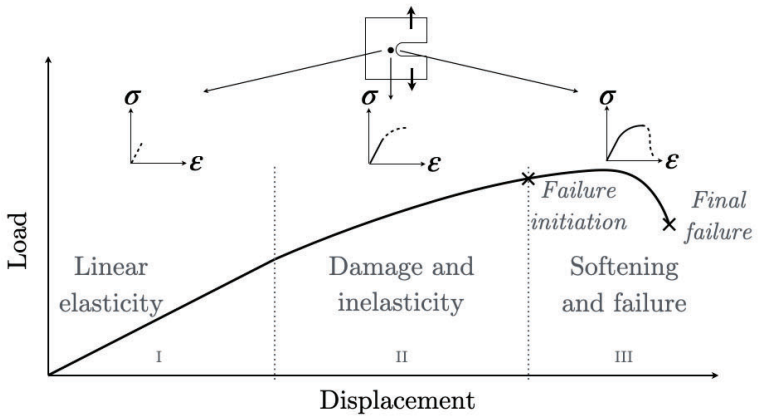

Figure 1.5: *The characteristic regions of a force-displacement curve used to guide the macroscale model development.*

1.3 Thesis Layout

The chapters which follow are dedicated, in turn, to each of the three regions described in Figure 1.5. Details regarding model development will be explained along with how each region is connected to the appended papers and research objectives. Further, test methods to characterise the required material properties experimentally will be discussed

[1]This point is referred to in **Paper A** as damage initiation. It is highlighted that this is simply a case of learning as you go, and should actually be referred to as failure initiation.

along with limitations and assumptions that exist in the model. Finally in terms of each region, places for improvement and recommendations for future work will be given. A few key limitations, valid for all regions that were considered during the development of the macroscale model are:

- It has been assumed that for all regions, the material behaviour can be described using an orthotropic stiffness tensor.
- Only the tensile and shear behaviours of the materials have been considered. The model in its current state has not been developed to handle compressive loading.
- The experimental tests that the models are based on were carried out at strain rates between 1%/min - 10%/min. Therefore the restriction to quasi-static loading has been made.
- Only small strain theory has been considered, i.e. geometrical non-linearities have not been accounted for.

2 Region I: Orthotropic Elasticity

For materials like steel, that can be considered isotropic in standard applications, only two properties are required to characterise the elastic behaviour; a Young's modulus $E = 210$ GPa and a Poisson's ratio $\nu = 0.3$. When a material is isotropic, it means that it gives the same behavioural response regardless of how the material is oriented with respect to the loading direction.

While polymers can generally be considered isotropic, the addition of reinforcement fibres creates a material with a strong directional preference. In unidirectional composites, the fibre direction is significantly stiffer and stronger than its counterparts. At the ply level however, as shown in Figure 2.1, there is one plane that is typically considered as isotropic. Materials that possess a single plane of isotropy are referred to as being transversely isotropic, and require five properties to describe their elastic behaviour. It is here that the local (material) reference frame can be introduced. Consider a transversely isotropic material, where the preferred material direction (in this case the fibre direction) is defined by the 1-axis. This is illustrated in Figure 2.1. The required stiffness properties are then the Young's modulus in the fibre direction E_1, the Young's modulus transverse to the fibre direction $E_2 = E_3$ and the shear modulus in the non-isotropic planes $G_{12} = G_{13}$. The final two properties are the Poisson's ratios ν_{23} and $\nu_{12} = \nu_{13}$.

As fibre reinforcement architectures become more complex, as with 3D-woven composites, transverse isotropy is no longer a valid assumption. Another more general option, is the adoption of an orthotropic description of the elastic material behaviour. One of the main assumptions in this paper is that the considered 3D-woven composites can, in a homogenised sense, be described as an orthotropic material. By definition, orthotropic materials have three preferred directions, each with unique material properties. Orthotropic materials therefore require nine elastic properties. As shown in Figure 2.1, once again, the local material frame is introduced. The nominal warp, horizontal weft and vertical weft direction for an orthogonal weave are denoted by 1, 2 and 3 respectively. The nine elastic

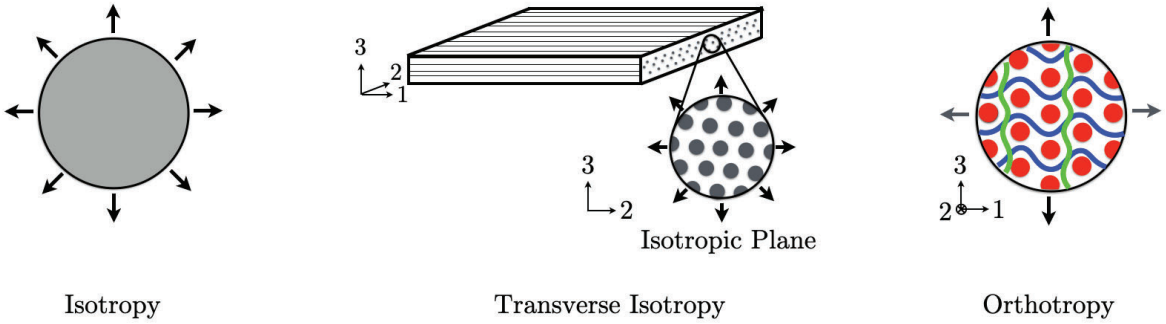

Figure 2.1: *An illustration of isotropy, transverse isotropy and orthotropy.*

properties are then three Young's moduli for the reinforcement directions E_1, E_2, E_3, three stiffness moduli in shear G_{12}, G_{23}, G_{13} and three Poisson's ratios ν_{12}, ν_{23} and ν_{13}.

2.1 Orthotropic Stiffness and Structural Tensors

From the nine elastic properties, the elastic constitutive stiffness relationship in the local material frame, can be expressed in Voigt form as

$$\begin{bmatrix} \sigma_{11} \\ \sigma_{22} \\ \sigma_{33} \\ \sigma_{12} \\ \sigma_{23} \\ \sigma_{13} \end{bmatrix} = \begin{bmatrix} \frac{E_1\,(1-\nu_{32}\nu_{23})}{\Delta} & \frac{E_1\,(\nu_{21}+\nu_{31}\nu_{23})}{\Delta} & \frac{E_1\,(\nu_{31}+\nu_{21}\nu_{32})}{\Delta} & 0 & 0 & 0 \\ \frac{E_2\,(\nu_{12}+\nu_{13}\nu_{32})}{\Delta} & \frac{E_2\,(1-\nu_{31}\nu_{13})}{\Delta} & \frac{E_2\,(\nu_{32}+\nu_{31}\nu_{12})}{\Delta} & 0 & 0 & 0 \\ \frac{E_3\,(\nu_{13}+\nu_{12}\nu_{23})}{\Delta} & \frac{E_3\,(\nu_{23}+\nu_{13}\nu_{21})}{\Delta} & \frac{E_3\,(1-\nu_{12}\nu_{21})}{\Delta} & 0 & 0 & 0 \\ 0 & 0 & 0 & G_{12} & 0 & 0 \\ 0 & 0 & 0 & 0 & G_{23} & 0 \\ 0 & 0 & 0 & 0 & 0 & G_{13} \end{bmatrix} \begin{bmatrix} \epsilon_{11} \\ \epsilon_{22} \\ \epsilon_{33} \\ \gamma_{12} \\ \gamma_{23} \\ \gamma_{13} \end{bmatrix} \tag{2.1}$$

where

$$\Delta = 1 - \nu_{12}\nu_{21} - \nu_{23}\nu_{32} - \nu_{31}\nu_{13} - 2\nu_{12}\nu_{23}\nu_{31}. \tag{2.2}$$

Describing the elastic behaviour of 3D-woven composites using the constitutive relationship in Equation (2.1) works perfectly, as long as the local material frame stays aligned with the global coordinate axis. The global coordinate system will be denoted by an $xyz-$system from this point forward. One of the main benefits of 3D-woven composites however, is that an entire component can be woven in near net-shape. This means that the local reinforcement directions can generally vary over a 3D-woven composite component. In order to deal with the varying material orientation, two main options are available to express the stiffness tensor in a global xyz-system. The first option is point-wise coordinate transformations using transformation matrices for 3D space. This requires the definition of three angles, cf. Bunge angles [13]. The second option, and the one considered here, is the use of structural tensors. The orientation of the material is then defined based on the three vectors describing the nominal orientation of each reinforcement direction.

Before the structural tensor based formulation of the orthotropic stiffness tensor can be fully introduced, a slight modification to the way the elastic properties are expressed is required. Nine new elastic properties must be introduced. Specifically, they are denoted by ϕ_{IJ} and φ_I for $I = 1, 2, 3$ and $J = 1, 2, 3$. These parameters once again represent the elastic behaviour of the material in the local 123-frame of reference. The stiffness tensor in Equation (2.1) can then alternatively be expressed as

$$\underline{\underline{\mathbb{E}}} = \begin{bmatrix} \phi_{11}+\varphi_1 & \phi_{12} & \phi_{13} & 0 & 0 & 0 \\ \phi_{12} & \phi_{22}+\varphi_2 & \phi_{23} & 0 & 0 & 0 \\ \phi_{13} & \phi_{23} & \phi_{33}+\varphi_3 & 0 & 0 & 0 \\ 0 & 0 & 0 & 1/4\,(\varphi_1+\varphi_2) & 0 & 0 \\ 0 & 0 & 0 & 0 & 1/4\,(\varphi_2+\varphi_3) & 0 \\ 0 & 0 & 0 & 0 & 0 & 1/4\,(\varphi_3+\varphi_1) \end{bmatrix}. \tag{2.3}$$

In a practical application, the values of ϕ_{IJ} and φ_I can be found from values of E_1, E_2, E_3, G_{12}, G_{23}, G_{13}, ν_{12}, ν_{23} and ν_{13} by simply comparing Equations (2.3) and (2.1).

The next step towards the structural tensor based representation of orthotropy is the introduction of three vectors $\boldsymbol{a}^1$, $\boldsymbol{a}^2$ and $\boldsymbol{a}^3$. These are unit length vectors and are assumed to be orthogonal to each other. The vector $\boldsymbol{a}^1$ is chosen to describe the nominal orientation of the warp yarns. Similarly $\boldsymbol{a}^2$ should describe the nominal direction of the horizontal weft yarns. In the case of an orthogonal weave, the vector $\boldsymbol{a}^3$ describes the direction of the vertical weft yarns. Otherwise, for a layer-to-layer interlock weave, $\boldsymbol{a}^3$ should simply describe the out-of-plane direction. From this point forward, the model formulations will largely speaking be carried out in tensor notation.

From the three vectors describing the reinforcement orientation, three corresponding second order structural tensors can be expressed. They are

$$\boldsymbol{A}^1 = \boldsymbol{a}^1 \otimes \boldsymbol{a}^1, \quad \boldsymbol{A}^2 = \boldsymbol{a}^2 \otimes \boldsymbol{a}^2 \quad \text{and} \quad \boldsymbol{A}^3 = \boldsymbol{a}^3 \otimes \boldsymbol{a}^3. \tag{2.4}$$

Further, from the second order tensors, three fourth order tensors can be introduced where

$$\mathbb{A}^I = \frac{1}{2}\left(\boldsymbol{A}^I \bar{\otimes} \boldsymbol{I} + \boldsymbol{I} \bar{\otimes} \boldsymbol{A}^I\right), \text{ for } I = 1, 2, 3 \tag{2.5}$$

and $\boldsymbol{I}$ is the second order identity tensor. Note that the non-standard $\bar{\otimes}$ operator expresses the operation $(\boldsymbol{A}\bar{\otimes}\boldsymbol{B})_{ijkl} = A_{ik}B_{jl}$ in index notation. These second and fourth order structural tensors have a number of properties which will come in handy during future tensor manipulations:

- $\boldsymbol{A}^1 + \boldsymbol{A}^2 + \boldsymbol{A}^3 = \boldsymbol{I}$.
- $\boldsymbol{A}^I : \boldsymbol{A}^J = \delta^{IJ}$, i.e. the Kronecker delta where $\delta^{IJ} = \begin{cases} 1 & \text{if } I = J \\ 0 & \text{if } I \neq J \end{cases}$
- $\boldsymbol{A}^I \cdot \boldsymbol{A}^J = \delta^{IJ}\boldsymbol{A}^I$.

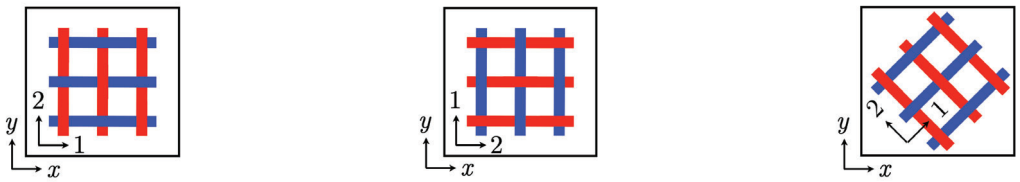

(a) $\boldsymbol{a}^1 = [1\,0\,0]^T$, $\boldsymbol{a}^2 = [0\,1\,0]^T$, $\boldsymbol{a}^3 = [0\,0\,1]^T$. (b) $\boldsymbol{a}^1 = [0\,1\,0]^T$, $\boldsymbol{a}^2 = [1\,0\,0]^T$, $\boldsymbol{a}^3 = [0\,0\,1]^T$. (c) $\boldsymbol{a}^1 = \left[\sqrt{2}/2\ \sqrt{2}/2\ 0\right]^T$, $\boldsymbol{a}^2 = \left[-\sqrt{2}/2\ \sqrt{2}/2\ 0\right]^T$, $\boldsymbol{a}^3 = [0\,0\,1]^T$.

Figure 2.2: *A schematic illustrating different orientations of the reinforcement aligned coordinate system.*

- $\mathbb{A}^I : \boldsymbol{A}^J = \delta^{IJ}\boldsymbol{A}^I$.

Finally, using structural tensors, the orthotropic elastic stiffness in the global $xyz-$system is given by

$$\mathbb{E} = \sum_{I=1}^{3} \varphi_I \mathbb{A}^I + \sum_{I=1}^{3}\sum_{J=1}^{3} \phi_{IJ}\boldsymbol{A}^I \otimes \boldsymbol{A}^J. \tag{2.6}$$

For clarity, if the reinforcement directions are aligned with the global coordinate axes as shown in Figure 2.2a (i.e. $\boldsymbol{a}^1 = [1\,0\,0]^T$, $\boldsymbol{a}^2 = [0\,1\,0]^T$ and $\boldsymbol{a}^3 = [0\,0\,1]^T$) then Equation (2.6) gives Equation (2.3) in Voigt form. On the other hand if the reinforcements are rotated in the manner shown in Figure 2.2b (i.e. $\boldsymbol{a}^1 = [0\,1\,0]^T$, $\boldsymbol{a}^2 = [1\,0\,0]^T$ and $\boldsymbol{a}^3 = [0\,0\,1]^T$) then in Voigt form Equation (2.6) is expressed as

$$\underline{\mathbb{E}} = \begin{bmatrix} \phi_{22}+\varphi_2 & \phi_{12} & \phi_{23} & 0 & 0 & 0 \\ \phi_{12} & \phi_{11}+\varphi_1 & \phi_{13} & 0 & 0 & 0 \\ \phi_{23} & \phi_{13} & \phi_{33}+\varphi_3 & 0 & 0 & 0 \\ 0 & 0 & 0 & 1/4\,(\varphi_1+\varphi_2) & 0 & 0 \\ 0 & 0 & 0 & 0 & 1/4\,(\varphi_1+\varphi_3) & 0 \\ 0 & 0 & 0 & 0 & 0 & 1/4\,(\varphi_2+\varphi_1) \end{bmatrix}. \tag{2.7}$$

2.2 A Constitutive Framework for 3D-Woven Composites

In the 1980s, Spencer [14] suggested that for UD composites, the constitutive stress-strain relationship can be divided into different parts. This included one term describing the reinforcement direction, one term containing a contribution of volumetric nature and a term with the remaining components. This is discussed in more detail in **Paper B**. A large benefit to such an approach, is that it provides a way to organise your thoughts in a

modular fashion. This helps determine which material constituents govern what material behaviours and in turn what impact they have on each stress and strain component based on loading direction. A number of authors including Nedjar [15], Vogler et al. [16], Camanho et al. [17] all built off of Spencer's constitutive framework. One major focus of **Paper B**, was proposing an equivalent framework for 3D-woven composites.

In the proposed framework, the stress $\boldsymbol{\sigma}$ is separated into four terms. The first contains the stress component in shear and is denoted $\boldsymbol{s}$. The remaining three contain the stress component in the reinforcement direction. Then

$$\boldsymbol{\sigma} = \boldsymbol{s} + \sum_{I=1}^{3} (\boldsymbol{\sigma} : \boldsymbol{A}^I)\boldsymbol{A}^I. \tag{2.8}$$

Again, 1,2,3 represents the warp direction, horizontal weft direction and vertical weft (or out-of-plane) direction respectively. In matrix form, when $\boldsymbol{a}^1 = [1\,0\,0]^T$, $\boldsymbol{a}^2 = [0\,1\,0]^T$ and $\boldsymbol{a}^3 = [0\,0\,1]^T$ this is equivalent to

$$\boldsymbol{\sigma} = \underbrace{\begin{bmatrix} 0 & \sigma_{xy} & \sigma_{xz} \\ \sigma_{xy} & 0 & \sigma_{yz} \\ \sigma_{xz} & \sigma_{yz} & 0 \end{bmatrix}}_{\boldsymbol{s}} + \underbrace{\begin{bmatrix} \sigma_{xx} & 0 & 0 \\ 0 & 0 & 0 \\ 0 & 0 & 0 \end{bmatrix}}_{(\boldsymbol{\sigma}:\boldsymbol{A}^1)\boldsymbol{A}^1} + \underbrace{\begin{bmatrix} 0 & 0 & 0 \\ 0 & \sigma_{yy} & 0 \\ 0 & 0 & 0 \end{bmatrix}}_{(\boldsymbol{\sigma}:\boldsymbol{A}^2)\boldsymbol{A}^2} + \underbrace{\begin{bmatrix} 0 & 0 & 0 \\ 0 & 0 & 0 \\ 0 & 0 & \sigma_{zz} \end{bmatrix}}_{(\boldsymbol{\sigma}:\boldsymbol{A}^3)\boldsymbol{A}^3}. \tag{2.9}$$

It is here, where the notation $T^I = \boldsymbol{\sigma} : \boldsymbol{A}^I$ is introduced. Conceptually, this means that that T^I denotes the normal stress component along each reinforcement direction I. This means that the stress $\boldsymbol{s}$ does not contribute to the normal stresses along the reinforcement directions, i.e. $\boldsymbol{s} : \boldsymbol{A}^I = 0$. To further help with understanding, consider the case where the reinforcement yarns in the 12-plane are oriented at 45° to the xy-system illustrated in Figure 2.2c. Then

$$T^1\boldsymbol{A}^1 = \left(\frac{\sigma_{xx} + \sigma_{yy}}{2} + \sigma_{xy}\right) \begin{bmatrix} 0.5 & 0.5 & 0 \\ 0.5 & 0.5 & 0 \\ 0 & 0 & 0 \end{bmatrix} \tag{2.10}$$

$$T^2\boldsymbol{A}^2 = \left(\frac{\sigma_{xx} + \sigma_{yy}}{2} - \sigma_{xy}\right) \begin{bmatrix} 0.5 & -0.5 & 0 \\ -0.5 & 0.5 & 0 \\ 0 & 0 & 0 \end{bmatrix} \tag{2.11}$$

$$T^3\boldsymbol{A}^3 = \sigma_{zz} \begin{bmatrix} 0 & 0 & 0 \\ 0 & 0 & 0 \\ 0 & 0 & 1 \end{bmatrix}. \tag{2.12}$$

The strain can be split in a similar manner, where

$$\boldsymbol{\epsilon} = \boldsymbol{e} + \sum_{I=1}^{3} (\boldsymbol{\epsilon} : \boldsymbol{A}^I)\boldsymbol{A}^I. \tag{2.13}$$

In this case $\boldsymbol{e}$ denotes the shear components of the strain tensor, whereas term $\boldsymbol{\epsilon} : \boldsymbol{A}^I$ gives the magnitude of the normal strain component along each reinforcement direction. Again, this means that $\boldsymbol{e} : \boldsymbol{A}^I = 0$.

A fourth order tensor that will come in handy in the future is $\mathbb{Q}$. This tensor allows $\boldsymbol{s}$ and $\boldsymbol{e}$ to be directly isolated from the full stress and strain tensors by the operation

$$\boldsymbol{s} = \mathbb{Q} : \boldsymbol{\sigma} \quad \text{and} \quad \boldsymbol{e} = \mathbb{Q} : \boldsymbol{\epsilon}, \tag{2.14}$$

where

$$\mathbb{Q} = \mathbb{I} - \sum_{I=1}^{3} \boldsymbol{A}^I \otimes \boldsymbol{A}^I \tag{2.15}$$

and $\mathbb{I}$ is the fourth order identity tensor. It follows (from some manipulations) that the tensor $\mathbb{Q}$ has the properties $\mathbb{Q} : \boldsymbol{A}^I = \boldsymbol{0}$ and $\mathbb{Q} : \mathbb{A}^I = \mathbb{A}^I$.

The final step in developing the proposed constitutive framework for 3D-woven composites is the combination of the stress decomposition in Equation (2.8), the strain decomposition in Equation (2.13) and the expression for the orthotropic stiffness tensor in Equation (2.6). Beginning with the definition of $\boldsymbol{s}$, it is possible to expresses

$$\begin{aligned}
\boldsymbol{s} &= \mathbb{Q} : \boldsymbol{\sigma} \\
&= \mathbb{Q} : \mathbb{E} : \boldsymbol{\epsilon} \\
&= \sum_{I=1}^{3} \varphi_I \left(\mathbb{A}^I - \boldsymbol{A}^I \otimes \boldsymbol{A}^I \right) : \boldsymbol{\epsilon} \\
&= \sum_{I=1}^{3} \varphi_I \mathbb{A}^I : \boldsymbol{e}.
\end{aligned} \tag{2.16}$$

It can be highlighted here, that a main feature of this decomposition is that $\boldsymbol{s}$ can be obtained directly from $\boldsymbol{e}$. Continuing with the reinforcement related terms, it can be found that

$$\begin{aligned}
T^I \boldsymbol{A}^I &= \left(\boldsymbol{\sigma} : \boldsymbol{A}^I \right) \boldsymbol{A}^I \\
&= \left(\mathbb{E} : \boldsymbol{\epsilon} : \boldsymbol{A}^I \right) \boldsymbol{A}^I \\
&= \left(\varphi_I \left(\boldsymbol{\epsilon} : \boldsymbol{A}^I \right) + \sum_{J=1}^{3} \phi_{IJ} \left(\boldsymbol{\epsilon} : \boldsymbol{A}^J \right) \right) \boldsymbol{A}^I \\
&= \varphi_I \boldsymbol{A}^I \otimes \boldsymbol{A}^I : \boldsymbol{\epsilon} + \frac{1}{2} \sum_{J=1}^{3} \phi_{IJ} \left(\boldsymbol{A}^I \otimes \boldsymbol{A}^J + \boldsymbol{A}^J \otimes \boldsymbol{A}^I \right) : \boldsymbol{\epsilon}.
\end{aligned} \tag{2.17}$$

In summary, the proposed constitutive framework can therefore be expressed as

$$\boldsymbol{\sigma} = \underbrace{\mathbb{E}_m : \boldsymbol{e}}_{\text{shear}} + \underbrace{\mathbb{E}_{f1} : \boldsymbol{\epsilon}}_{\text{warp}} + \underbrace{\mathbb{E}_{f2} : \boldsymbol{\epsilon}}_{\text{h. weft}} + \underbrace{\mathbb{E}_{f3} : \boldsymbol{\epsilon}}_{\text{v. weft}}, \tag{2.18}$$

where

$$\mathbb{E}_m = \sum_{I=1}^{3} \varphi_I \mathbb{A}^I, \text{ and } \mathbb{E}_{fI} = \varphi_I \boldsymbol{A}^I \otimes \boldsymbol{A}^I + \frac{1}{2} \sum_{J=1}^{3} \phi_{IJ} \left(\boldsymbol{A}^I \otimes \boldsymbol{A}^J + \boldsymbol{A}^J \otimes \boldsymbol{A}^I \right). \tag{2.19}$$

Again, each term will govern the constitutive behaviour of either a reinforcement direction or in shear. In Voigt form, when $\boldsymbol{a}^1 = \begin{bmatrix}1 & 0 & 0\end{bmatrix}^T$, $\boldsymbol{a}^2 = \begin{bmatrix}0 & 1 & 0\end{bmatrix}^T$ and $\boldsymbol{a}^3 = \begin{bmatrix}0 & 0 & 1\end{bmatrix}^T$, Equation (2.18) is given by

$$\begin{bmatrix}\sigma_{xx}\\ \sigma_{yy}\\ \sigma_{zz}\\ \sigma_{xy}\\ \sigma_{yz}\\ \sigma_{xz}\end{bmatrix} = \begin{bmatrix}\varphi_1 & 0 & 0 & 0 & 0 & 0\\ 0 & \varphi_2 & 0 & 0 & 0 & 0\\ 0 & 0 & \varphi_3 & 0 & 0 & 0\\ 0 & 0 & 0 & \frac{\varphi_1+\varphi_2}{4} & 0 & 0\\ 0 & 0 & 0 & 0 & \frac{\varphi_2+\varphi_3}{4} & 0\\ 0 & 0 & 0 & 0 & 0 & \frac{\varphi_1+\varphi_3}{4}\end{bmatrix}\begin{bmatrix}0\\0\\0\\ \gamma_{xy}\\ \gamma_{yz}\\ \gamma_{xz}\end{bmatrix} + \begin{bmatrix}\phi_{11}+\varphi_1 & \frac{\phi_{12}}{2} & \frac{\phi_{13}}{2} & 0 & 0 & 0\\ \frac{\phi_{12}}{2} & 0 & 0 & 0 & 0 & 0\\ \frac{\phi_{13}}{2} & 0 & 0 & 0 & 0 & 0\\ 0 & 0 & 0 & 0 & 0 & 0\\ 0 & 0 & 0 & 0 & 0 & 0\\ 0 & 0 & 0 & 0 & 0 & 0\end{bmatrix}\begin{bmatrix}\epsilon_{xx}\\ \epsilon_{yy}\\ \epsilon_{zz}\\ \gamma_{xy}\\ \gamma_{yz}\\ \gamma_{xz}\end{bmatrix}$$
$$+ \begin{bmatrix}0 & \frac{\phi_{12}}{2} & 0 & 0 & 0 & 0\\ \frac{\phi_{12}}{2} & \phi_{22}+\varphi_2 & \frac{\phi_{23}}{2} & 0 & 0 & 0\\ 0 & \frac{\phi_{23}}{2} & 0 & 0 & 0 & 0\\ 0 & 0 & 0 & 0 & 0 & 0\\ 0 & 0 & 0 & 0 & 0 & 0\\ 0 & 0 & 0 & 0 & 0 & 0\end{bmatrix}\begin{bmatrix}\epsilon_{xx}\\ \epsilon_{yy}\\ \epsilon_{zz}\\ \gamma_{xy}\\ \gamma_{yz}\\ \gamma_{xz}\end{bmatrix} + \begin{bmatrix}0 & 0 & \frac{\phi_{13}}{2} & 0 & 0 & 0\\ 0 & 0 & \frac{\phi_{23}}{2} & 0 & 0 & 0\\ \frac{\phi_{13}}{2} & \frac{\phi_{23}}{2} & \phi_{33}+\varphi_3 & 0 & 0 & 0\\ 0 & 0 & 0 & 0 & 0 & 0\\ 0 & 0 & 0 & 0 & 0 & 0\\ 0 & 0 & 0 & 0 & 0 & 0\end{bmatrix}\begin{bmatrix}\epsilon_{xx}\\ \epsilon_{yy}\\ \epsilon_{zz}\\ \gamma_{xy}\\ \gamma_{yz}\\ \gamma_{xz}\end{bmatrix}. \tag{2.20}$$

2.3 Required Experimental Tests and Model Results

Characterising the complete elastic behaviour of an orthotropic material goes back to determining a combination of nine independent parameters, often in terms of the set: E_1, E_2, E_3, G_{12}, G_{23}, G_{13}, ν_{12}, ν_{23} and ν_{13}. In fact, some of the earliest modelling approaches for 3D-woven composites focused on predicting these elastic material properties using analytic methods. Whitney and Chou [7] for example, presented a model to predict in-plane elastic properties by creating a geometric unit cell that they then divided into smaller microcells to form an inclined laminate. Yushanov and Bogdanovich [18] on the other hand developed an analytic approach to predict elastic stiffness in all three directions. Their method, known as the Generalised Modified Matrix Method, is based on local spatial averaging of the reinforcement paths.

Experimentally, some of these properties, i.e. E_1, E_2, ν_{12}, can be determined with relative ease using standardised test methods. For example, ASTM D3039 [19], ISO 527-4 [20] as well as AITM 1-0007 [21] all lay out guidelines for determining the in-plane tensile properties of fibre-reinforced polymer matrix composites. In each test standard, the general premise is the same: from an infused plate, cut out tensile specimens with either the warp or weft yarns running in the loading direction. The test specimens should be dimensioned such that multiple representative unit cells fit across the gauge region. From the force reading of the tensile test machine and the cross section area of the test sample, a global axial stress measure can be computed. Similarly, using either an extensometer or digital image correlation (DIC) software a global axial strain measure can be found. Depending on the capability of the available DIC software, it can even be possible to track the out-of-plane contraction of the test specimen and compute ν_{23} and ν_{13}.

Figures 2.3a and 2.3b show the approximate dimensions of tensile test specimens for the **FiberDuk** material along with the experimental spread of obtained stress-strain curves.

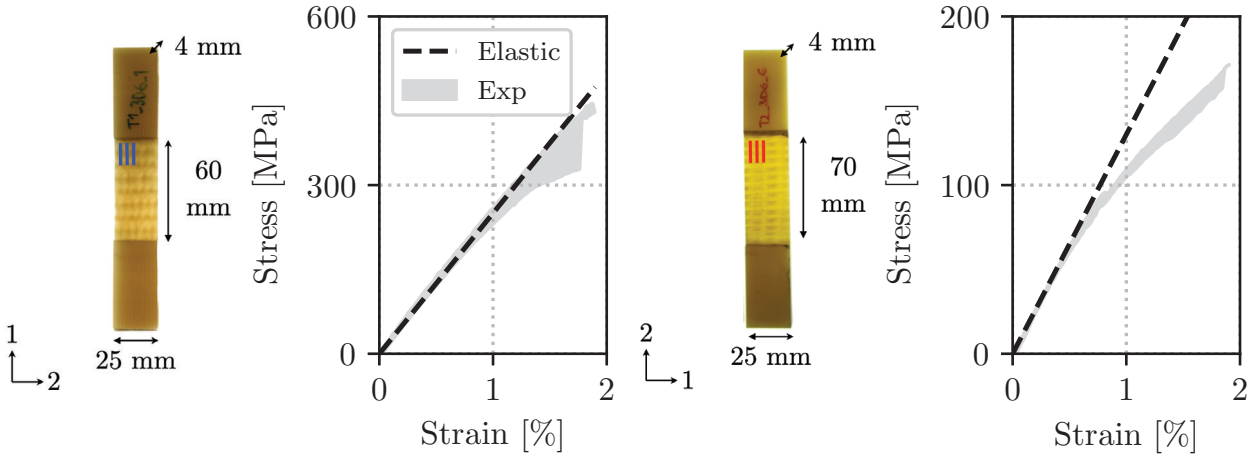

(a) *Tensile warp loading.* (b) *Tensile horizontal weft loading.*

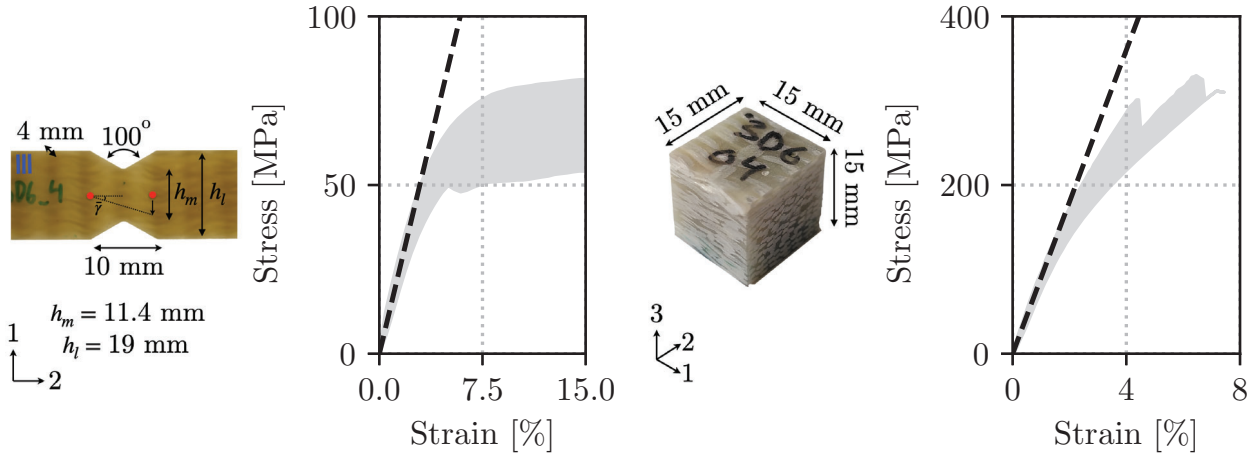

(c) *In-plane shear loading.* (d) *Compressive out-of-plane loading.*

Figure 2.3: *Experimental results for monotonic loading of the* ***FiberDuk*** *material. The spread of experimental results is shown in grey, while the elastic stiffness is illustrated in black.*

The computed elastic stiffness moduli are also illustrated in Figure 2.3 and summarised in Table 2.1. As previously discussed, the **FiberDuk** material is highly unbalanced. As a consequence, the elastic stiffness in the warp direction is close to double the elastic stiffness in the weft direction. For comparison, the same data for the **BAM** material is given by Figures 2.4a, 2.4b and Table 2.1. The **BAM** material shows a far more balanced behaviour. The variation between E_1 and E_2 is minimal in comparison to the **FiberDuk** material system. Further, as would be expected, the use of carbon-fibre reinforcement yarns creates a material which is far stiffer than its glass fibre reinforced counterpart.

In terms of increased complexity, what follows next is determining the in-plane shear elastic stiffness, G_{12}, of 3D-woven composites. Three main test standards are generally used in the literature: the Iosipescu test (ASTM D5379 [22]), the V-Notched Rail test (ASTM D7078 [23]) and the 45° off-axis tensile test. The Iosipescu test has been widely used since the 1980's and was standardised by ASTM in 1993. The Iosipescu test standard was used in the **FiberDuk** project. An image of the test sample is shown in Figure 2.3c

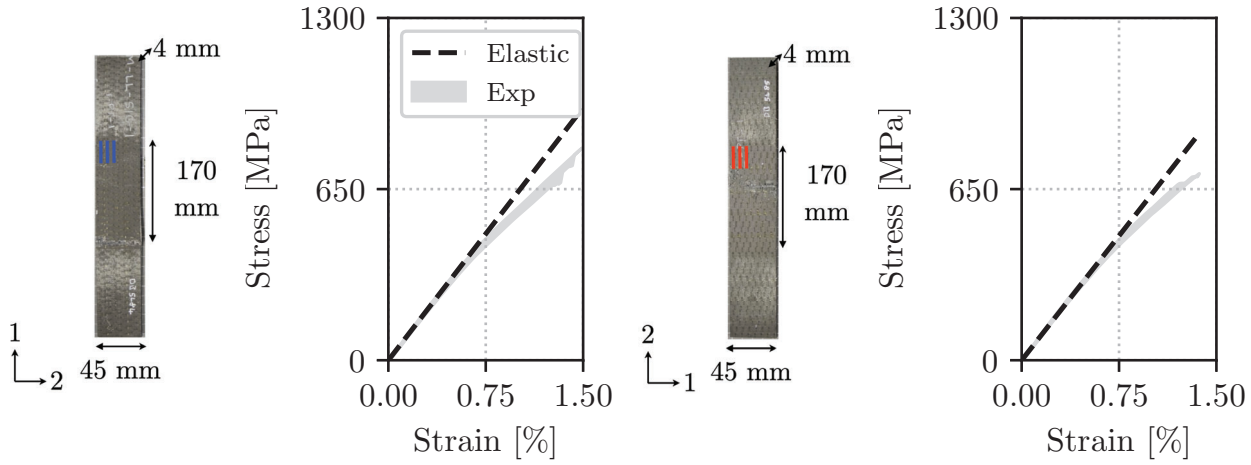

(a) *Tensile warp loading.*

(b) *Tensile weft loading.*

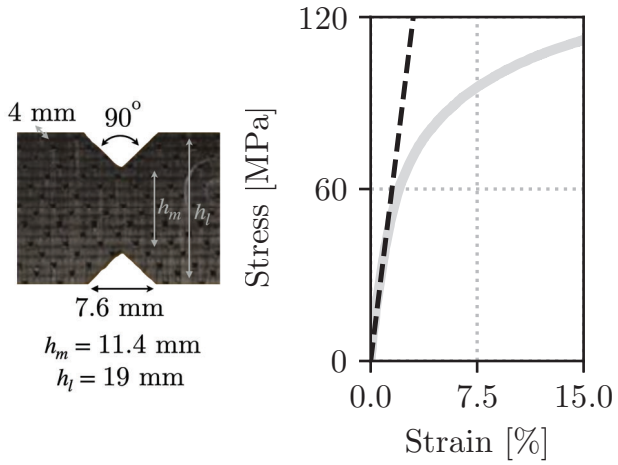

(c) *In-plane shear loading.*

Figure 2.4: *Experimental results for monotonic loading of the* ***BAM*** *material. The spread of experimental results is shown in grey, while the elastic stiffness is illustrated in black.*

along with specimen dimensions and the experimental spread of the stress-strain curves. In a testing rig, the edges of the test sample are clamped and the right hand side side is moved downwards. This creates a narrow band of uniform shear strain in the gauge region.

Another important, but challenging question with this test is related to how the shear strain should be measured. One possibility is to use DIC software to average the shear strain over a certain region. Determining this region, however, is a delicate task and can lead to diverse results. In the **FiberDuk** project, a strain measure was instead computed by tracking the relative vertical displacement of two points located on the edges of the gauge region. These are illustrated with red dots in Figure 2.3c along with the angle between them $\bar{\gamma}$. Then, assuming linear elasticity and that the shear force in each cross section is the same, it can be shown that theoretically, that the shear strain in the gauge

region is

$$\gamma = \frac{2\bar{\gamma}}{1 + \frac{h_m}{h_l}}. \tag{2.21}$$

The shear stress on the other hand is computed based on the vertical force measured by the testing rig and the cross-section area at the narrowest part of the gauge region. The obtained shear stiffness is given in Table 2.1. It can be seen in Figure 2.3c that the elastic region of the stress-strain curve is fairly consistent between the test samples.

The in-plane shear stiffness of the **BAM** material was originally characterised using a V-Notched Rail test. The principal features of the V-Notched Rail and Iosipescu test specimen are the same. The most noticeable difference is the test fixture which clamps the specimen faces instead of the edges. An image of a test sample clamped in the rig is shown in Figure 2.4c along with the obtained stress-strain curve. The shear stiffness is summarised in Table 2.1. More recently, the decision was made that under the VIRTEST-3D project, the relatively balanced nature of the BAM material would be exploited. To this end, 45° off-axis tensile specimens will be considered. The shear stress and strain in the local system can be extracted as

$$\sigma_{12} = \frac{1}{2}\sigma_{xx} \quad \text{and} \quad \gamma_{12} = \epsilon_{yy} - \epsilon_{xx}. \tag{2.22}$$

The strains ϵ_x and ϵ_y can be computed using DIC software to average the strains over the gauge region. It is important to note that this method is only applicable for balanced weaves. Otherwise, the tensile specimen will deform in an 's' shape. This means that the strain and stress fields can no longer be considered uniform and Equation (2.22) becomes invalid. Otherwise, as discussed by Tarnopol'skii and Kincis [24], a different angle can be chosen such that the ratio of shear to normal deformation is optimised and modifications to the grips can be made to avoid this 's' shaped deformation mode.

The remaining elastic properties, E_3, G_{23} and G_{13} are the most challenging to characterise. There's a certain amount of irony in this fact. One of the main selling features of 3D-woven composites is their out-of-plane properties, which are the most difficult to determine. Manufacturing a tensile test sample to compute E_3 with sufficient dimension is not a trivial task, and is commonly overcome by adding adhesively joined load introduction tabs. This is further complicated given that the out-of-plane strength of a 3D-woven composite is substantially higher than the strength of adhesives. The **FiberDuk** project elected to estimate E_3 using an out-of-plane compression test, the results of which are shown in Figure 2.3d and Table 2.1. Further, while test methods for determining out-of-plane shear stiffness do exist, c.f. Pettersson et al. [25], the size of the unit cell again introduces complexities. Ensuring that a representative number of unit cells exist in the gauge region is not possible using a standard test rig. For the **FiberDuk** material, it was simply assumed that the out-of-plane shear stiffness values were equivalent to the in-plane value.

A promising method to circumvent the challenges associated with characterising the out-of-plane behaviour of 3D-woven composites is explored in **Paper E**. The main research question of this work is whether high-fidelity mesoscale models can be used to generate virtual calibration data for macroscale models. A schematic of the voxelised

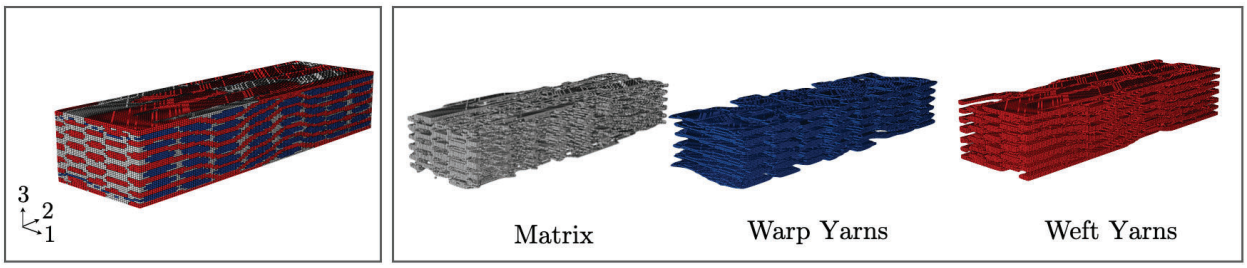

Figure 2.5: *Illustration of the mesoscale RVE of the* ***BAM*** *material.*

mesoscale finite element model developed by Topalidis et al. [26] at the Bristol Composites Institute, is shown in Figure 2.5. Two distinct user-defined material subroutines have been developed, one for each material constituent, i.e. impregnated yarn and matrix. By loading this RVE is six unique deformation modes and computing the homogenising stress and strain fields, it is possible to determine the full orthotropic material stiffness tensor. From this stiffness tensor, the 9 elastic material properties can be found. They are also summarised in Table 2.1 and show good agreement to in-plane properties determined experimentally.

Table 2.1: Elastic parameters for the **FiberDuk** and **BAM** material.

FiberDuk	Stiffness	E_1	25 [GPa]	E_2	13 [GPa]	E_3	9 [GPa]
	Shear stiffness	G_{12}	1.8 [GPa]	G_{13}	1.8 [GPa]	G_{23}	1.8 [GPa]
	Poisson's ratio	ν_{12}	0.21 [-]	ν_{13}	0.30 [-]	ν_{23}	0.30 [-]
BAM	Stiffness	E_1	64 [GPa]	E_2	63 [GPa]		
Experimental	Shear stiffness	G_{12}	4.0 [GPa]				
BAM	Stiffness	E_1	76 [GPa]	E_2	62 [GPa]	E_3	10 [GPa]
RVE analysis	Shear stiffness	G_{12}	3.9 [GPa]	G_{13}	3.2 [GPa]	G_{23}	3.7 [GPa]
	Poisson's ratio	ν_{12}	0.06 [-]	ν_{13}	0.38 [-]	ν_{23}	0.46 [-]

2.4 Limitations and Future Work

The headline of this section "Orthotropic Elasticity" highlights one of the earliest assumptions that was made at the start of this research project. For the developed macroscale model to be applicable to a given 3D-woven composite, it must be possible to describe the composite's behaviour using an orthotropic stiffness tensor. Evaluating and verifying all possible terms in a fully anisotropic stiffness tensor experimentally would not be a trivial task. In particular it would require the characterisation of complex couplings between in-plane, out-of-plane, normal and shear behaviours. The use of mesoscale models again, opens up for the possibility to quickly evaluate the overall anisotropy produced by a reinforcement architecture.

The symmetrised [1] elastic stiffness tensor (in the local material frame) produced by the mesoscale model of the **BAM** material is

$$\underline{\mathbb{E}}_{BAM} = \begin{bmatrix} 77.5 & 6.37 & 4.18 & 0.008 & -0.001 & 0.003 \\ 6.37 & 67.8 & 4.91 & -0.0003 & -0.009 & -0.019 \\ 4.18 & 4.91 & 10.2 & -0.001 & -0.002 & -0.0004 \\ 0.008 & -0.0003 & -0.001 & 3.92 & -0.001 & -0.001 \\ -0.001 & -0.009 & -0.002 & -0.001 & 3.17 & -0.001 \\ 0.003 & -0.019 & -0.0004 & -0.001 & -0.001 & 3.71 \end{bmatrix} \text{[GPa]}, \quad (2.23)$$

in Voigt form. The upper right quadrant and lower left quadrant of the stiffness tensor are not exactly zero. The overall magnitude in comparison to the remaining values is however minimal. Similarly, analysing an internal unit cell of the **CERFAC** material gives

$$\underline{\mathbb{E}}_{CERFAC} = \begin{bmatrix} 72.4 & 6.67 & 6.64 & -0.012 & 0.003 & 0.008 \\ 6.67 & 13.3 & 4.50 & -0.006 & 0.006 & -0.016 \\ 6.64 & 4.50 & 13.4 & -0.003 & 0.002 & -0.022 \\ -0.012 & -0.006 & -0.003 & 3.84 & -0.004 & 0.006 \\ 0.003 & 0.006 & 0.002 & -0.004 & 3.87 & -0.002 \\ 0.008 & -0.016 & -0.022 & 0.006 & -0.002 & 1.98 \end{bmatrix} \text{[GPa]}. \quad (2.24)$$

In both cases, assuming orthotropic elasticity is reasonable, but one should be cautious when approaching new material systems. Further, there is an indication for both material systems that assuming a constant shear stiffness in all planes is not ideal.

It should be noted that while the **CERFAC** and **FiberDuk** material have the same weave architecture, they use different yarn types which will have an impact on their overall behaviour. In the future a similar analysis should be carried out for a dedicated mesoscale model of the **FiberDuk** material.

3 Region II: Inelasticity and Progressive Damage

Following a region of relative linearity, 3D-woven composites begin to show non-linear behaviours. These non-linearities can be due to a number of different mechanisms at different scales. For example, microscale cracks can form within the yarns, in the matrix pockets and/or the interfaces between them. As the matrix properties deteriorate, yarns can also straighten and deform within the composite. Another source of non-linearity can be the material constituents themselves. Many common polymer matrices show prominent non-linear behaviours on their own cf. Woo et al. [27], Saseendran et al. [28] or Bardella [29].

As previously discussed, a phenomenological model aims to simply mimic the non-linear phenomena that these subscale behaviours cause. Figure 3.1 shows the stress-strain curve

[1] The raw stiffness tensor showed minor asymmetry, however was symmetrised given $\underline{\mathbb{E}}_{sym} = \frac{1}{2}\left(\underline{\mathbb{E}} + \underline{\mathbb{E}}^T\right)$

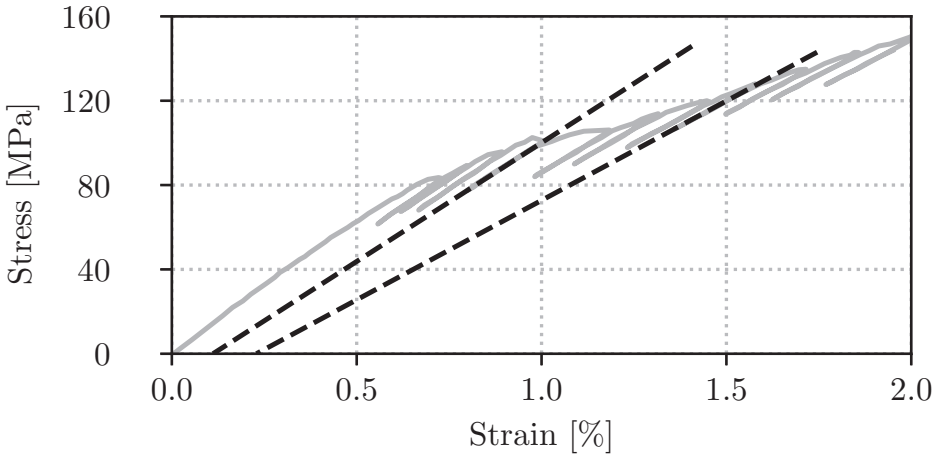

Figure 3.1: *Illustration of the stiffness reduction and permanent strain development of the* ***FiberDuk*** *material loaded cyclically in the horizontal weft direction.*

results for a tensile test in the horizontal weft direction of the **FiberDuk** material. More importantly, the material sample is loaded and unloaded cyclically throughout the test. This brings us to the main punch-line of the entire section. By extending the unloading curves (shown with a dotted line) to the horizontal-axis it is apparent that the material is showing a progressive loss of stiffness and development of permanent strain. These are the phenomena that the macroscale model must predict using traditional constitutive material modelling techniques.

3.1 Characterising Constitutive Models

Choosing a constitutive model, or combination of constitutive models for a given material, can be a challenging task. On one hand, the choice of constitutive model(s) should be tied to objective observations made during a testing campaign. On the other hand, there is a certain level of personal subjectivity that can relate to the desired level of complexity in a material model and in the available experimental results. When choosing constitutive models for region II, the distinction can be made between two main groups. Continuum damage models allow for the reduction in material stiffness while inelasticity models allow for the progressive development of permanent (i.e. inelastic) strain.

Material models for inelasticity can be further subdivided into different categories. According to Haupt [30], material behaviours (excluding damage) and their corresponding constitutive models can be classified by four main categories: elasticity, plasticity, viscoelasticity and viscoplasticity. They are illustrated in Figure 3.2 along with one-dimensional rheological models that help describe the physical significance of each individual theory. They are classified as follows:

- **Elasticity:** *rate-independent material behaviour without hysteresis.* Elasticity is the simplest of constitutive models. It restricts itself to the idea that a material element will revert to its initial configuration once any external loads are removed. Further, it will load and unload along the same path, meaning that no energy is

dissipated. Elasticity, which was the main focus of Section 2, can be represented rheologically by a spring with stiffness E. In the case of linear elasticity, the spring stiffness is constant, and the constitutive stress-strain relationship is given by

$$\sigma = E\epsilon. \tag{3.1}$$

- **Viscoelasticity:** *rate-dependent material behaviour without equilibrium hysteresis.* As the name suggests, viscoelasticity involves the combination of both elastic and viscous properties. A viscoelastic material loads and unloads along different paths and gives permanent deformation. Viscoelastic materials show rate-dependence, meaning that their constitutive behaviour varies depending on how quickly or slowly loading takes place, i.e. the higher the strain rate, the stiffer the response. These materials also show what is known as relaxation and creep. When a viscoelastic material is loaded to a certain strain and held at that strain level, the stress in the material will slowly decrease. This is relaxation. Creep on the other hand describes a phenomenon where if a material sample is loaded under a constant stress, the strain will slowly increase.

  Viscous behaviours can be described rheologically through the addition of a damper with viscosity μ which resists motion through viscous friction proportional to the loading velocity. Figure 3.2b shows what is commonly referred to as the Zener model. This combination of two springs and a damper organised both in series and in parallel is one of the simplest rheological models that can mimic both creep and relaxation. The 1D constitutive stress-strain relationship for the Zener model is given by

$$\sigma = E_0\epsilon + E_1(\epsilon - \epsilon_i), \tag{3.2}$$

  where ϵ_i denotes the inelastic strain over the damper. What should be highlighted here is that a defining feature of viscoelasticity is its equilibrium relation. If loading takes place sufficiently slowly, the stress-strain curve will show an elastic response. Conceptually speaking, in the case of the Zener model, the elastic behaviour is governed by the upper spring with stiffness E_0.

- **Plasticity:** *rate-independent material behaviour with hysteresis.* Continuum plasticity theories have their background in experiments carried out on metals. In the 1860's for example, Tresca [31] observed that once a threshold shear stress is reached, a metal will begin to "flow" and develop permanent deformations. The classical theory of plasticity expands from the idea that after a region of linear elasticity, a stress limit is reached and the material enters a region of plastic flow. The stress limit is commonly referred to as the yield limit and will be denoted by σ_y. From a rheological perspective, plasticity requires the introduction of a Coulomb friction element, which only shows deformation once the yield stress is reached. Further, the stress in the friction device can not be higher in absolute value than σ_y. Figure 3.2c shows a rheological model for plasticity with hardening. The constitutive relationship can then be expressed generically as

$$\sigma = E\left(\epsilon - \epsilon_p\right). \tag{3.3}$$

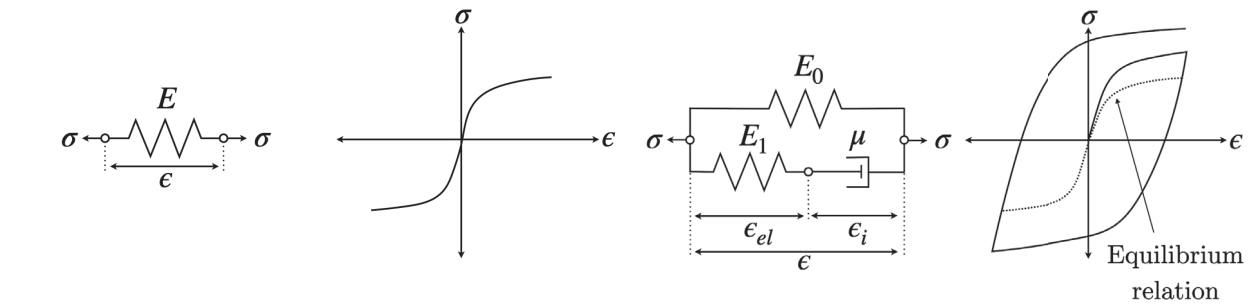

(a) *Elasticity.* (b) *Viscoelasticity.*

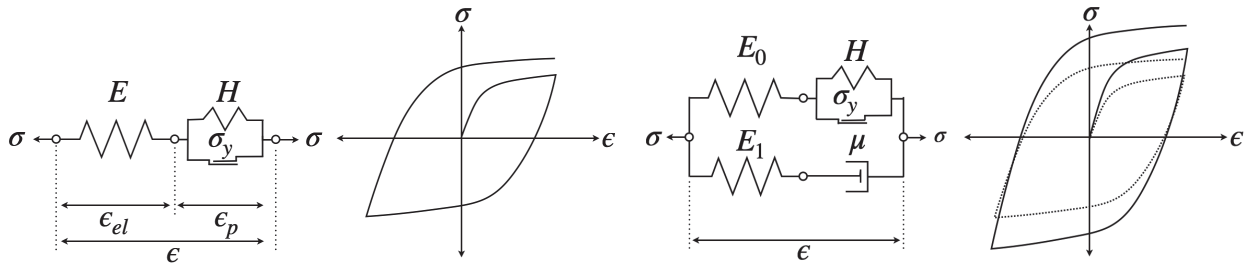

(c) *Plasticity.* (d) *Viscoplasticity.*

Figure 3.2: *The four material classifications according to Haupt [30].*

A traditional plasticity model also requires the introduction of additional information. Firstly, a yield surface, ϕ_p is needed where $\phi_p < 0$ represents an elastic response and $\phi_p = 0$ a plastic response. Further, flow rules which govern the development of the plastic strain and any internal hardening variables must also be introduced.

- **Viscoplasticity:** *rate-dependent material behaviour with equilibrium hysteresis.* Viscoplasticity is the most inclusive. It embraces all of the previously mentioned material theories: elastic, plastic and viscous behaviours. The rheological model shown in Figure 3.2d combines both elastic springs, a Coulomb friction element and a viscous dampers. The main feature that allows for the differentiation of viscoelasticity and viscoplasticity relates to the equilibrium relation. When a viscoplastic material model is loaded sufficiently slowly, the constitutive behaviour continues to show hysteresis. Viscoplasticity will not be discussed or used further in this work.

While inelastic models (plasticity, viscoelasticity, viscoplasticity) allow for predicting non-linear behaviours due to permanent strain development, their unloading behaviour is related to the elastic stiffness. Again, it is clear from Figure 3.1, that 3D-woven composites show a progressive degradation in stiffness. The most straightforward way to model stiffness reduction and the non-linearity it causes, is through the use of continuum damage theories, the basis of which was introduced by Kachanov [32] and Rabotnov [33]. Once again, their work was carried out on metallic materials. The foundational idea of continuum damage theory is that diffuse cracking reduces the effective load carrying area

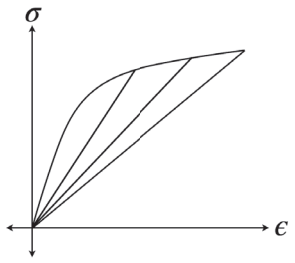

Figure 3.3: *Illustration of unloading behaviour for a standard continuum damage model.*

within a material. This in turn causes a reduction in stiffness. The stiffness reduction is typically represented with a damage variable d. The most standard representation of elastic damage in 1D is

$$\sigma = (1 - d)E\epsilon. \tag{3.4}$$

In this respect when $d = 0$, the material is completely intact. On the other hand $d = 1$ signifies that the material has been completely degraded and has no remaining stiffness. Similarly, a damage variable of, for example, $d = 0.1$ would mean that the material has lost 10% of its initial stiffness.

An illustrative example of a stress-strain curve for the constitutive relationship given by Equation (3.4) is shown in Figure 3.3. The relationship is only illustrated in the positive stress-strain quadrant as the behaviour of damage models in compression is not necessarily straightforward. Some materials show what is known as the *unilateral character of damage*. When loaded in compression, the microcracks close and the material recaptures the initial elastic stiffness. Note, unlike those in Figure 3.2, the non-linearity is due to a progressive loss in stiffness. As no permanent strains develop, the stress-strain curve will always pass through the origin.

By combining inelastic and continuum damage models, a wide range of behaviours related to experimentally observed phenomena of 3D-woven composites can be predicted. The choice of material models, their combination and what phenomena are important can be challenging to make. Careful consideration should be given to the type of experimental tests that are available, what non-linear behaviours are seen and how they can be represented by different constitutive models.

3.2 Viscoelasticity and 3D-Woven Composites

Traditionally, viscoelasticity is introduced in its simplest form using a 1D rheological model known as the Maxwell model. Shown in Figure 3.4, this involves a serial coupling of a viscous damper and elastic spring. Figure 3.4 shows the stress-strain and relaxation behaviour of such a model with a spring with an elastic stiffness $E = 1$ N/m^2 and a damper with a viscosity $\mu = 10^3$ Ns/m^2. The model is loaded to 1% strain in one second and then held constant. The relaxation behaviour is plotted in both a linear and logarithmic time scale. Maxwell models are said to show a characteristic relaxation time

$\tau = \mu/E$. From the peak stress σ_0, it can be shown that the initial rate of change will be $\dot{\sigma} = \sigma_0 E/\mu$. If the stress was to continue to decrease at this rate, it would reach a zero-stress state at time $\tau = \mu/E$. This is shown with a dashed line in Figure 3.4. The characteristic relaxation time in this case is $\tau = 10^3$ which is clear in the logarithmic time scale plot. Conceptually speaking, the characteristic relaxation time is a good measure of when the majority of the stress has relaxed from the system.

The simple nature of the Maxwell model does have its drawbacks. As a linear viscoelastic model with one viscous property μ, the range of possible behaviours that it can capture is limited. Most notably, the model is unable to show creep in a realistic way or show complex relaxation behaviours. Further, it will always relax to zero stress. These challenges can be overcome by considering increasingly complex combinations of spring and damper elements. For example, a Kelvin-Voigt model which has a spring and damper in parallel shows a more realistic creep behaviour. The Zener model is obtained by adding a spring in parallel to a Maxwell element, as shown in Figure 3.5. It gives both realistic creep and relaxation behaviour. Further, due to the added spring the model will never relax completely to zero stress. The total stress in the model will be a combination of the stress in the spring element and Maxwell element. In this case the results are shown for a given parameter set defined by $E_0 = 2$ Nm^2, $E_1 = 1$ Nm^2 and $\mu = 10^3$.

It is also possible to chain multiple Maxwell elements together in parallel to allow for more complex relaxation behaviour, see Figure 3.6. In this case, two Maxwell elements are chained together in parallel. The first element has parameters given by $E_1 = 1.5$ Nm^2 and $\mu_1 = 10^2$ while the second element is defined by $E_2 = 1$ Nm^2 and $\mu_2 = 10^3$. Again the total stress is the combination of both.

This is all to say that it is possible to design quite complex viscoelastic material behaviours by conceptually considering combinations of rheological elements each with their own relaxation behaviour. Fitting these models and their relaxation behaviour can be done with relative ease, cf. Emri and Tschoegl [34]. Combining multiple rheological elements is an approach taken by for example Nedjar [15] for capturing creep behaviour of fibre-reinforced composites with viscoelastic matrices. However, for materials with long relaxation times, many Maxwell elements in parallel are required. This can lead to quite

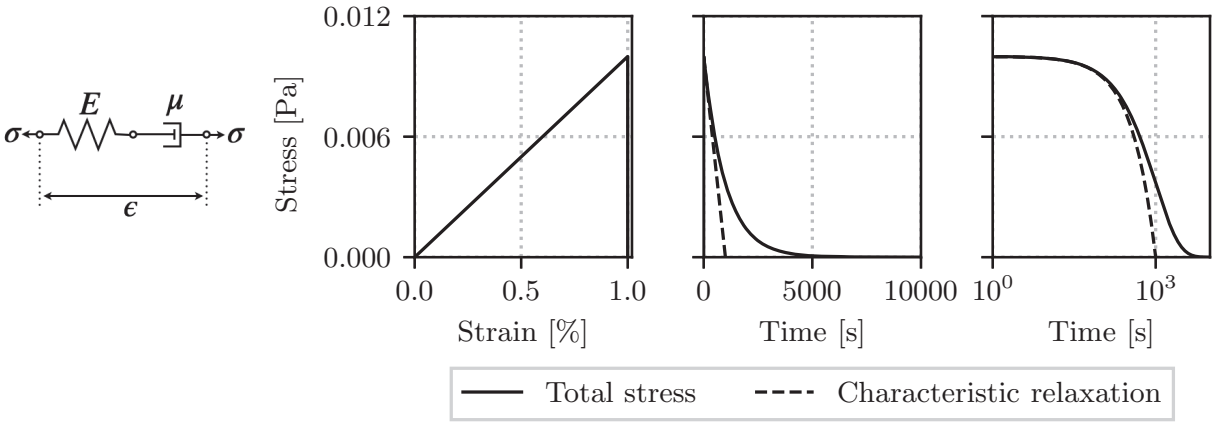

Figure 3.4: *Loading and relaxation behaviour of a Maxwell element where* $E = 1$ N/m^2 *and* $\mu = 10^3$ Ns/m^2.

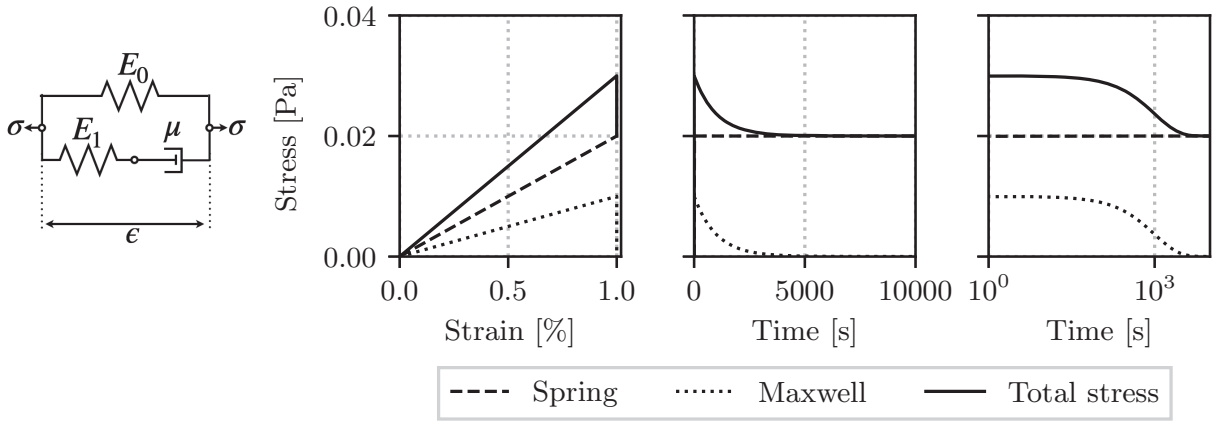

Figure 3.5: *Loading and relaxation behaviour of a Zener element where* $E_0 = 2$ N/m^2, $E_1 = 1$ Nm^2 *and* $\mu = 10^3$ Ns/m^2.

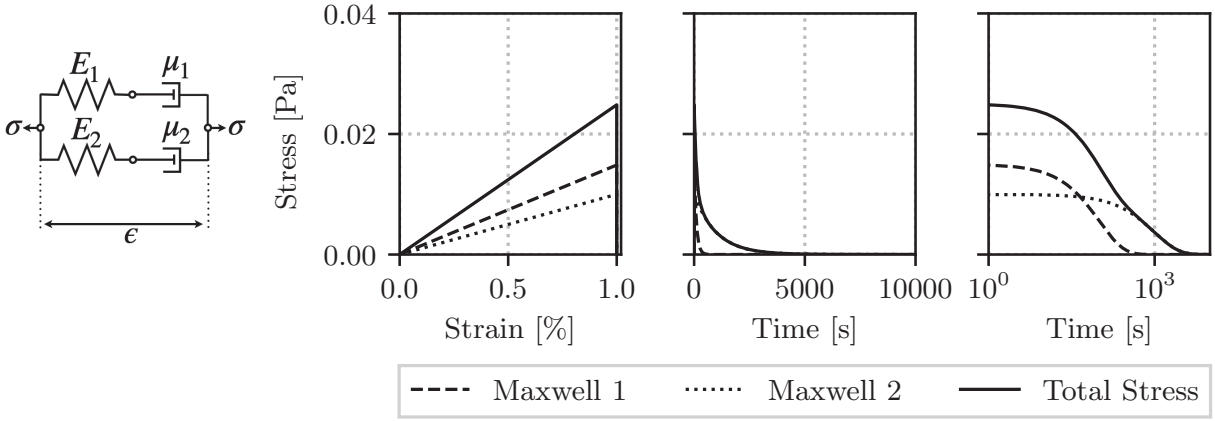

Figure 3.6: *Loading and relaxation behaviour of a Maxwell model with two elements where* $E_1 = 1.5$ N/m^2, $E_2 = 1$ Nm^2, $\mu_1 = 10^2$ Ns/m^2 *and* $\mu_1 = 10^3$ Ns/m^2.

complex systems of differential equations to resolve. Further, these systems can require the identification of a large number of parameters. They can also be challenging to work with when considering multiaxial loading scenarios and anisotropic materials, which show different viscous behaviours depending on loading mode.

One alternative is then to use Spectral formulations, see for example Maire [35] who developed a model to describe viscous behaviour of UD fibre-reinforced composites. In a spectral model a series of Maxwell or Kelvin-Voigt elements are generalised by associating their viscous parameters to a continuous spectrum. This reduces the number of parameters and also allows the model to describe creep and relaxation in a realistic way. For continuity, it can also be pointed out that other viscoelastic modelling strategies do exist, see for example integral formulations proposed by Schapery [36] and fractional theories described well by Müller et al. [37] and Enelund et al. [38].

When it comes to viscoelastic modelling of 3D-woven composites, a number of examples (at different scales) can be found in the literature. In these examples it is assumed that a region of pure elasticity does not exist, and the material shows a viscoelastic response from the very beginning. Both Conejos et al. [39] and Hirsekorn et al. [40] use a

two scale homogenisation technique to predict the viscoelastic behaviour of 3D-woven composites. On the microscale they assume that within the yarns the individual fibres are surrounded by an isotropic viscoelastic matrix. This is homogenised to predict the behaviour of the consolidated yarns. It is then assumed once more that these yarns are themselves surrounded by isotropic viscoelastic matrix pockets. In Hirsekorn et al. [40], the viscoelasticity of the matrix pockets is described using what amounts to a generalised Maxwell model with multiple elements. Their model in particular, was able to predict the relaxation behaviour of the composite as well as the temperature dependence of the mechanical behaviour of the composite.

Moving up the scales *The Onera Damage Model for Polymer Matrix Composites* [41] considers anisotropic viscoelastic material behaviour on the macroscale. They adopt a spectral approach to describe the development of viscoelastic strain. The model is able to predict the non-linear behaviour of 3D-woven composites due to viscous effects. Their results show good agreement to experiments carried out on elementary test coupons as well as more complex structures.

3.2.1 A 1D Non-Linear Viscoelastic Model

One of the main contributions of **Paper B** is the development of a viscoelastic extension to the framework introduced in Section 2.2. Again, it was assumed that a region of linear elasticity does not exist and that all non-linearity is due to viscoelastic behaviour of the matrix. A Norton power-law model [42] was adopted in order to describe the development of viscoelastic strain. It will first be described in one dimension, before the extension to three dimensions is introduced.

For the one-dimensional case the Norton model is essentially a Maxwell element with a non-linear viscous damper. The constitutive one-dimensional equation is then

$$\sigma = E\left(\epsilon - \epsilon_i\right), \tag{3.5}$$

where the viscous strain development is defined by

$$\dot{\epsilon}_i = \frac{1}{t_*}\left(\frac{|\sigma|}{\kappa}\right)^n \operatorname{sgn}\left(\sigma\right). \tag{3.6}$$

In a Maxwell element, the viscoelastic strain in the damper develops as $\dot{\epsilon}_i = \sigma/\mu$, i.e. there is a linear relationship with the stress. In a Norton model, this relationship is now non-linear. The range of possible behaviours expands by introducing additional parameters (i.e. t_*, κ^n, n) that can be tuned to give the desired response.

3.2.2 Extending to 3D

In order to incorporate viscoelasticity in an anisotropic manner, **Paper B** proposes that a division can be made between shear and reinforcement related behaviours. Then, assuming an additive split of the strain into an elastic and viscoelastic part, the constitutive framework from Equation (2.18) can be extended such that

$$\boldsymbol{\sigma} = \mathbb{E}_m : (\boldsymbol{e} - \boldsymbol{e}_i) + (\mathbb{E}_{f1} + \mathbb{E}_{f2} + \mathbb{E}_{f3}) : \left(\boldsymbol{\epsilon} - \epsilon_{v1}\boldsymbol{A}^1 - \epsilon_{v2}\boldsymbol{A}^2 - \epsilon_{v3}\boldsymbol{A}^3\right) \tag{3.7}$$

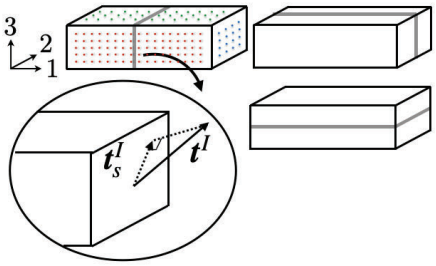

Figure 3.7: *Illustration of the three slip planes defined by the reinforcement architecture, and the projected shear stress* $\boldsymbol{t}_s^I$.

Here $\boldsymbol{e}_i$ describes the viscoelastic strain in shear, and $\epsilon_{vI}\boldsymbol{A}^I$ the viscoelastic strain in each reinforcement direction $I = 1, 2, 3$. By construction, the total viscoelastic strain is then

$$\boldsymbol{\epsilon}_i = \boldsymbol{e}_i + \epsilon_{v1}\boldsymbol{A}^1 + \epsilon_{v2}\boldsymbol{A}^2 + \epsilon_{v3}\boldsymbol{A}^3 \tag{3.8}$$

As the **FiberDuk** material only shows prominent non-linearity in shear and under tensile loading in the horizontal weft direction (cf. Figure 2.3) focus is given to determining $\boldsymbol{e}_i$ and $\epsilon_{v2}\boldsymbol{A}^2$. That is, it is assumed that $\epsilon_{v1} = \epsilon_{v3} = 0$. However, the presented framework is general and allows for the addition of viscous phenomena in a modular fashion based on loading direction. In the event that a material shows prominent non-linearity in multiple reinforcement directions, a similar process can be followed.

Turning to the Norton model, the evolution of inelastic strain in the horizontal weft reinforcement direction can be expressed as

$$\dot{\epsilon}_{v2}\boldsymbol{A}^2 = \frac{1}{t_*^r}\left(\frac{\left|\boldsymbol{\sigma} : \boldsymbol{A}^2\right|}{\kappa^r}\right)^{n^r} \operatorname{sgn}\left(\boldsymbol{\sigma} : \boldsymbol{A}^2\right)\boldsymbol{A}^2. \tag{3.9}$$

Note that here, this means that ϵ_{v2} gives the magnitude of the inelastic strain while $\boldsymbol{A}^2$ gives the direction.

In order to describe the viscoelastic strain development in shear, a crystal plasticity inspired approach was considered. It allows for modelling localised slip behaviour in planes defined by the reinforcement architecture. This is illustrated in Figure 3.7. The shear behaviour in these planes can then be assumed to be driven by the total projected shear stress $\boldsymbol{t}_s^I = \boldsymbol{\sigma}\cdot\boldsymbol{a}^I - (\boldsymbol{\sigma} : \boldsymbol{A}^I)\,\boldsymbol{a}^I$ which is also illustrated in Figure 3.7.

Note in this case I indicates one of the three slip planes shown in Figure 3.7. Using a Norton style model for the development of viscoelastic strain in shear then gives that

$$\dot{\boldsymbol{e}}_i = \sum_{I=1}^{3} \underbrace{\frac{1}{t_*^I}\left(\frac{\left|\boldsymbol{t}_s^I\right|}{\kappa^I}\right)^{n^I}}_{Magnitude} \underbrace{\boldsymbol{m}^I}_{Direction}, \tag{3.10}$$

where the norm of the shear traction can (after some manipulations) be expressed as

$$\left|\boldsymbol{t}_s^I\right| = \sqrt{\boldsymbol{s} : \mathbb{A}^I : \boldsymbol{s}}. \tag{3.11}$$

Once again, it is possible to differentiate the magnitude and direction of the viscoelastic strain development. Finally, the direction of viscoelastic strain development is chosen to be of associate type, where

$$\boldsymbol{m}^I = \frac{\partial \left| \boldsymbol{t}_s^I \right|}{\partial \boldsymbol{s}} = \frac{\mathbb{A}^I : \boldsymbol{s}}{\sqrt{\boldsymbol{s} : \mathbb{A}^I : \boldsymbol{s}}}. \tag{3.12}$$

Note that it is only the shear stress $\boldsymbol{s}$ that drives the inelasticity in shear.

As previously discussed, in **Paper B** it was assumed that only loading in the horizontal weft reinforcement direction as well as in shear show viscous behaviour. Further, it was assumed, due to a lack of experimental results, that the material behaviour in all three shear slip planes can be described by the same viscous properties. It should be highlighted however, that one benefit of this model is its modularity. The model can be modified to allow different viscous behaviours in each reinforcement direction and in each shear plane. Further, the required parameters can be fit independently from experimental tests for each loading mode.

Identifying the parameters for each loading mode requires an identification routine. In **Paper B** this was realised using MATLAB's *fminsearch* which uses the Nelder Mead optimisation method [43]. Within *fminsearch's* objective function, the commercial finite element program Abaqus is used. A user material UMAT file containing the implemented viscoelastic material model is opened and the viscous parameters are changed in each optimisation iteration. The UMAT as well as an input file containing the tensile or shear specimen geometry is submitted. Once the job is completed, the resulting force-displacement data is extracted and compared to the experimental results. Finally, the error between the simulation results and experimental results can be computed.

3.2.3 Required Experimental Tests and Model Results

This 3D viscoelastic model was developed under the assumption that all initial non-linearity is due to the viscous behaviour of the matrix. To fully calibrate the proposed model, monotonic tensile tests are required in each reinforcement direction and shear test are required in each shear plane. This leads to a very similar discussion as that presented in Section 2.3, for characterising the elastic behaviour of 3D-woven composites. Well established test standards exist for characterising the in plane behaviour ([19], [20], [21], [22], [23]), i.e. the warp, horizontal weft and in-plane shear directions. The out-of-plane tensile and shear behaviour is more challenging to characterise. Once again, a mesoscale model of a representative unit cell which accounts for rate-dependent behaviour could be very promising. Unfortunately a unit cell model of this nature was not available during the course of this research work.

As previously discussed it is assumed in **Paper B** that the only viscous behaviour shown by the **FiberDuk** material is related to loading in the horizontal weft direction and in in-plane shear. This means that a total of six viscous properties must be determined. Note however, that it is not possible to uniquely determine t_*^r and $(\kappa^r)^{n^r}$ and t_*^I and $(\kappa^I)^{n^I}$. As such it is convenient to prescribe $\kappa^r = 1$ MPa and $\kappa^I = 1$ MPa to maintain a dimensionless quantity within the brackets. The calibrated viscoelastic parameters are summarised in Table 3.1 The obtained force-displacement curve fits are shown in Figures

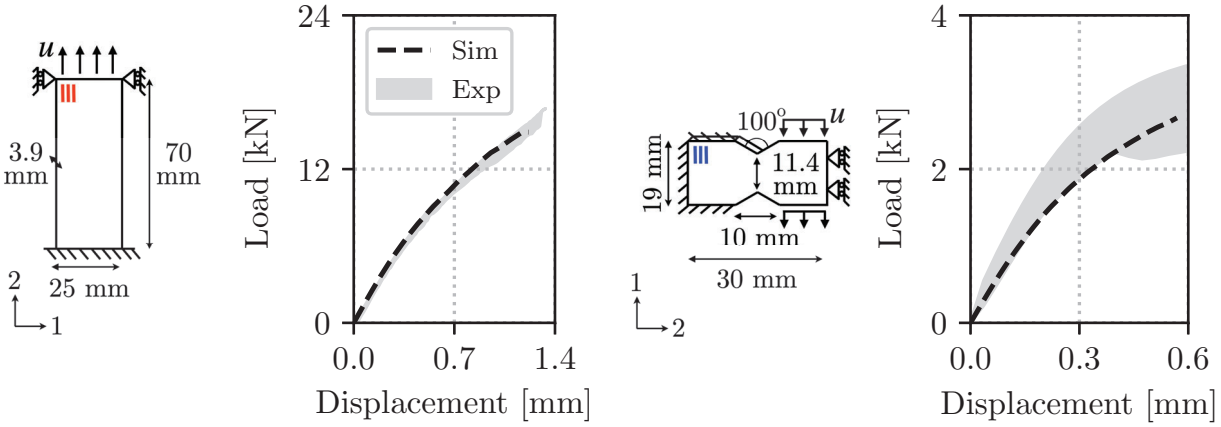

(a) *Horizontal weft loading.* (b) *In-plane shear loading.*

Figure 3.8: *Experimental and simulated force-displacement curves using the calibrated parameters summarised in Table 3.1 as well schematics of the FE models used in the calibration routine.*

3.8a and 3.8b along with schematics illustrating the dimensions and boundary conditions applied to the FE models in the calibration routine. The non-linear behaviour of the Iosipescu shear test was fit until the first experimentally observed load drop.

Following the approach in **Paper B** should be done with some caution. The model's limitations and places for improvement are discussed further in Section 3.4. It is however noted once more, that one of the largest assumptions that must be made is that the material's non-linearity is strictly due to the viscous effects of the polymer matrix. To truly quantify the viscous behaviour of a material, creep and/or relaxation tests and/or monotonic loading at different strain rates should be used. What follows in the next section is a different approach to predicting the non-linear behaviour of 3D-woven composites, in which the assumption of rate-dependence is abandoned.

Table 3.1: Viscous parameters for the **FiberDuk** material.

Horizontal Weft	t_*^r	$3.75{\cdot}10^7$ [s]	n^r	1.72 [-]	κ^r	1 [MPa]
Shear plane $I = 2$	t_*^2	$6.46{\cdot}10^5$ [s]	n^2	1.54 [-]	κ^2	1 [MPa]

3.3 Damage, Plasticity and 3D-Woven Composites

If material rate-dependence is not a concern, a promising choice is then to combine plasticity and continuum damage models. In a simple one-dimensional case, it is assumed that the strain can be additively decomposed into an elastic and plastic part, i.e. $\epsilon = \epsilon_p + \epsilon_{el}$. The constitutive behaviour of a model combining damage and plasticity theory will then

take the form

$$\sigma = (1 - d)\, E\, (\epsilon - \epsilon_p)\,. \tag{3.13}$$

Even in the 1D case, a string of modelling choices are required. For a plasticity model on its own, a yield surface must be defined based on the type of hardening that is desired. Internal hardening variables are also required, the number and type depending on the hardening laws. Either associative or non-associative flow rules must also be introduced in order to describe the development of the plastic strain and hardening variables. For a 1D continuum damage model, the damage variable d is typically defined as a function of a strain measure. In the case of brittle damage models, this is generally the elastic strain. For ductile damage models on the other hand the plastic strain can also be used. Regardless of strain measure, a damage initiation threshold should be introduced, and a relationship to describe how the damage develops is needed. Finally, the interaction between the development of plastic strain and damage must be considered. As discussed by Grassl and Jirásek [44] for example, the plastic part of the model can be expressed in terms of the damaged stress or undamaged stress.

There are a number of cases of continuum damage mechanics being used to model the non-linear behaviour of 3D-woven composites. The majority of the examples take a mesoscale view of the problem. As discussed by Lomov et al. [45], most authors then initiate damage based on multiple failure criteria for the matrix and yarns. The latter is commonly described by criteria for UD composites. Subsequently, the constituent stiffness properties (matrix and yarn respectively) are progressively degraded according to the prevailing damage modes through multiple damage evolution laws.

Green et al. [46] use a continuum damage approach to account for all non-linearity in their mesoscale model. This includes damage to both the matrix and yarns. They use their model to highlight how important it is to develop a realistic representation of the mesoscale 3D-weave architecture. An idealised version of the weave architecture produced results which were overly stiff and strong, when compared to tensile experimental tests along the reinforcement directions. A mesoscale model with a more realistic representation of the weave structure showed better agreement to experimental results.

Both Topalidis et al. [26] and El Said et al. [47] add an additional source of non-linearity to their mesoscale models. Along with continuum damage, they use a pseudo-plasticity model to capture the non-linear shear behaviour of the yarns and matrix. This is done using an empirical formula relating shear stress and strain. In particular, El Said et al. combine both a macroscale and mesoscale approach by subdividing a test geometry into different subdomains. In order to minimise the computational cost, part of the structure is modelled on the macroscale assuming anisotropic linear elasticity, where each material point is assigned unique elastic properties. These properties are based on a Voronoi tessellation of the subscale architecture and takes into account material directions and fibre density. The highly loaded regions however, are modelled on the mesoscale, using the combined pseudo-plasticity and continuum damage approach as outlined above.

Once again, moving to a fully macroscale approach, the *Onera Damage Model for Polymer Matrix Composites* [41] also employs a continuum damage model. As previously discussed, they assume that the initial non-linear behaviour is due to the viscous behaviour of the matrix. At a later stage it is then assumed that damage begins to play a role in

the non-linear behaviour of the 3D-woven composite. As such multiple damage variables are then used to degrade pertinent components in the stiffness tensor.

3.3.1 A 1D Elasto-Plastic Damage Model

One of the main focuses of **Paper C**, was to develop an elasto-plasticity and continuum damage model with a clear calibration scheme. Further, the intention was to ensure that the model is only as complex as the available experimental results show is necessary. For this reason, an approach more closely related to Ladeveze and LeDantec [48] has been considered. It is then possible to associate all stiffness reducing mechanisms with the damage model, while the development of permanent strain is strictly handled by the plasticity model. The overall approach will first be described in 1D, before the extension to a 3D model is introduced.

The first concept that must be introduced, is the idea of effective stress, which will be denoted $\tilde{\sigma}$ from this point foreword. Consider the bar illustrated in Figure 3.9. The microcracks cause a reduction in load carrying area of the material. While the material globally is subjected to a stress σ, the undamaged material surrounding the cracks will feel a higher effective stress $\tilde{\sigma}$. The relationship between the two is described using a damage variable d where

$$\sigma = (1 - d)\,\tilde{\sigma}. \tag{3.14}$$

It is further assumed, that plasticity solely acts on the undamaged material. This in turn means that the yield surface can be constructed as a function of the effective stress. As the restriction has been made to only consider the positive stress-strain quadrant, isotropic hardening is assumed to be sufficient. In 1D, this means that the plastic yield surface takes the form

$$\phi_p = |\tilde{\sigma}| - \sigma_y - \kappa\,(k) \leq 0. \tag{3.15}$$

The yield stress σ_y as well as the isotropic hardening stress κ[1] can be determined from experimental testing. This will be discussed in more detail later in this section. From Equation (3.15) it is seen that κ is expressed as a function of what is referred to as an internal hardening variable k. It is a strain like quantity that monitors the evolution of the internal mechanism that leads to hardening.

Typically, the evolution of the plastic strain and internal hardening variables are defined using flow rules. These state that ϵ_p and k will develop in a direction normal to the yield surface. In this case it is convenient to define their development as

$$\dot{\epsilon}_p = \dot{\lambda}\frac{\partial \phi_p}{\partial \tilde{\sigma}} = \dot{\lambda}\,\mathrm{sgn}\,(\tilde{\sigma}) \tag{3.16}$$

$$\dot{k} = \dot{\lambda}\frac{\partial \phi_p}{\partial \kappa} = -\dot{\lambda}. \tag{3.17}$$

[1]Note that this κ and the parameters κ^r and κ^I introduced in Section 3.2.2 are not related to one another. They do however represent similar mechanisms, i.e. the resistance to the development of inelastic strain.

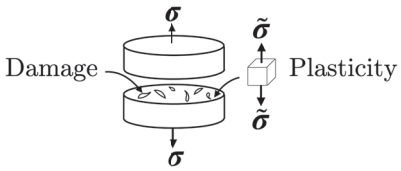

Figure 3.9: *An illustration of the stress and effective stress.*

Generally, $\dot{\lambda}$ is referred to as the plastic multiplier and λ signifies the magnitude of accumulated, equivalent plastic strain. Equations (3.16) and (3.17) then mean that the internal hardening variable and the plastic strain will grow proportionally to one another. Finally, the loading conditions for the plasticity model are

$$\dot{\lambda} \geq 0, \quad \phi_p \leq 0, \quad \dot{\lambda}\phi_p = 0. \tag{3.18}$$

In words, Equation (3.18) describes two possible model behaviours. The model can show an elastic response, where the material is not yielding and the plastic strain is not developing ($\phi_p < 0$ and $\dot{\lambda} = 0$). Otherwise the material is yielding and plastic strain is developing ($\phi_p = 0$ and $\dot{\lambda} \geq 0$).

It is now possible to define the damage model. Here an approach using a damage surface is adopted. In a similar vein to a yield surface, it dictates if damage is developing ($\phi_d = 0$) or if it is not ($\phi_d < 0$). As previously discussed, damage growth is typically linked to a strain measure. In this case an energy measure often referred to as the damage driving force is considered and denoted Y. The damage driving force is formulated based on thermodynamic argumentation, which is described in more detail in **Paper C**. For the 1D constitutive expression in Equation (3.13) the damage driving force is given by the effective elastic strain energy

$$Y = \frac{1}{2} E \epsilon_{el}^2. \tag{3.19}$$

The damage surface is then expressed as

$$\phi_d = Y - \eta(d) \leq 0. \tag{3.20}$$

The development of the damage is controlled by η, which can be determined experimentally. This will be discussed in more detail below. Finally, as with the plasticity model, a set of loading conditions can be defined where

$$\dot{d} \geq 0, \quad \phi_d \leq 0, \quad \dot{d}\phi_d = 0. \tag{3.21}$$

The loading conditions also enforce damage irreversibility, i.e. they ensure the material can not heal.

What remains is to determine σ_y and propose expressions for $\kappa(k)$ and $\eta(d)$ based on experimental data. Due to the formulation of the damage and plasticity models, this

can be done with relative ease. Consider the 1D illustrative tensile stress-strain curve with unloading cycles in Figure 3.10, which also shows the proposed calibration routine. Calibrating the plasticity and damage models therefore requires the following steps:

1. Determine where damage and plasticity should initiate, which can be at different locations. This is a somewhat delicate choice. The simplest option is to choose this point visually as the location where the curve begins to show non-linearity. From this point it is then possible to determine the yield stress σ_y as well as compute the initial elastic stiffness $E_{(0)}$ and the damage driving force at damage onset $Y_{(0)}$. Note here that the subscripts indicate unloading cycle number.

2. At the first unloading cycle, extrapolate the unloading curve to the strain axis. Compute the stiffness $E_{(1)}$ and the remaining permanent strain $\epsilon_{p(1)}$.

3. From the plastic strain, compute the elastic strain $\epsilon_{el(1)} = \epsilon_{(1)} - \epsilon_{p(1)}$. Compute the damage driving force at the first unloading cycle $Y_{(1)} = 1/2E_{(0)}\epsilon^2_{el(1)}$. Then compute the damage $d_{(1)} = 1 - E_{(1)}/E_{(0)}$ and plot the damage and damage driving force at the first unloading cycle.

4. Compute the effective stress at the first unloading cycle $\tilde{\sigma}_{(1)} = \sigma_{(1)}/(1-d_{(1)})$. From the effective stress, compute the isotropic hardening stress $\kappa_{(1)} = \tilde{\sigma}_{(1)} - \sigma_y$. Plot the isotropic hardening stress against the plastic strain

5. Repeat for all subsequent unloading cycles. Based on the damage vs driving force curve and hardening stress vs plastic strain curve, propose a function to describe each 1D relationship.

Following the completion of steps 1 through 5, a clear understanding of how the damage develops in the experiment with respect to the damage driving force is known. The same thing can be said about the development of the isotropic hardening stress with respect to the plastic strain. The convenience of the formulation of the flow rules given by Equations (3.16) and (3.17) can now be made more clear. As $|\epsilon_p| = -k$, the required expression for $\kappa(k)$ is equivalent to the proposed expression for $\kappa(\epsilon_p)$. Some helpful expressions that will be considered in the following sections are:

- Linear hardening: $\kappa(k) = -H_p k$. The parameter H_p is then the slope of the $\kappa - \epsilon_p$ curve.

- Exponential hardening with saturation: $\kappa(k) = \kappa_{sat}\left(1 - e^{ck}\right)$. The saturation value of the curve is then defined by κ_{sat} and c is a parameter which controls how steeply the curve approaches the saturation value.

Note that when choosing a function to represent the $\kappa - \epsilon_p$ curve, it must always pass through the origin.

Similarly, the required expression for $\eta(d)$ can also be determined with relative ease. Given the function describing the development of the damage $d(Y)$, $\eta(d)$ is found by inverting the expression. Again some helpful expressions are:

- Linear damage growth: $d(Y) = H_d\,(Y - Y_0)$. The Y-axis intercept of the curve is then Y_0 which signifies at what driving force value the damage initiates. Again, H_d is the slope of the line. In this case, inverting the damage function gives $\eta(d) = d/H_d + Y_0$.

- Exponential damage with saturation: $d(Y) = d_{sat}\left(1 - e^{-b(Y-Y_0)}\right)$, where b controls how steeply the damage curve approaches the saturation value d_{sat}. The damage onset value is given by Y_0. Inverting the damage function gives $\eta(d) = Y - \left(\frac{-\ln(1-d/d_{sat})}{b} + Y_0\right)$.

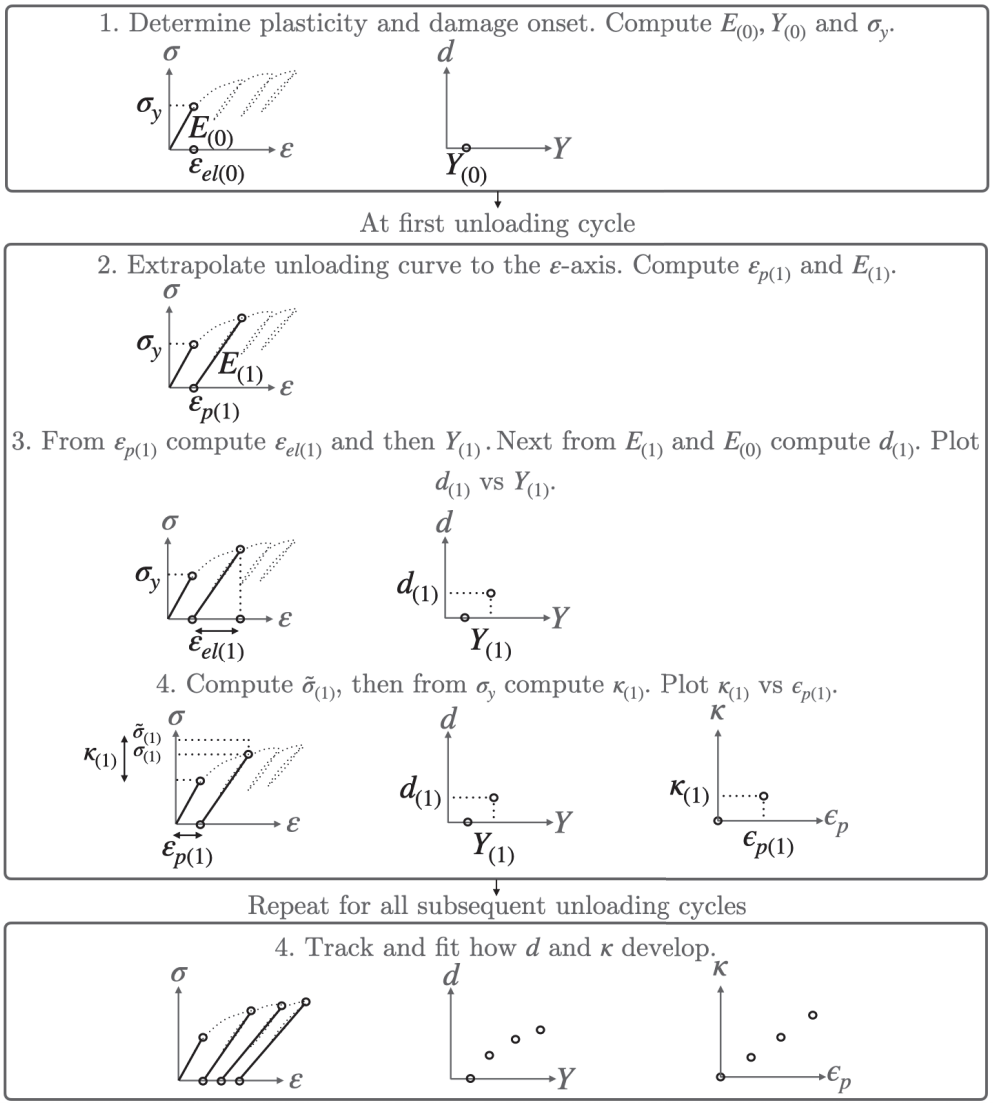

Figure 3.10: *A flow chart of the proposed parameter identification routine for the elasto-plasticity and damage model.*

3.3.2 Extending to 3D

Developing a full, orthotropic, elasto-plastic and progressive damage model in three dimensional space is not a trivial task. A full coupling of all potential phenomena and orthotropic directions is possible from a theoretical point of view. This however would require not only numerous material parameters, but also a complex in-depth testing campaign and calibration procedure. With this in mind **Paper C** prioritises capturing the non-linear behaviour of 3D-woven composites when loaded in the reinforcement directions and in shear.

Paper C combines the constitutive framework from Equation (2.18) with the 1D elasto-plastic damage model outlined in Section 3.3.1. Each term in the constitutive framework largely governs the behaviour in one of the reinforcement directions or in shear. The problem can therefore be conceptualised as four independent elasto-plastic damage models. This means that four damage variables can be introduced, each with their own damage surface. They are denoted d_s in shear as well as d_1, d_2 and d_3 in the warp, horizontal weft and vertical weft directions respectively. Further, four yield surfaces can be considered, which control plastic strain development in each reinforcement direction and shear. Then, the constitutive framework becomes

$$\boldsymbol{\sigma} = (1 - d_s)\,\mathbb{E}_m : (\boldsymbol{e} - \boldsymbol{e}_p) + \sum_{I=1}^{3} (1 - d_I)\,\mathbb{E}_{fI} : (\boldsymbol{\epsilon} - \boldsymbol{\epsilon}_p)\,. \tag{3.22}$$

The four damage surfaces, and their loading conditions are defined by

$$\phi_{ds} = Y_s - \eta_s(d_s) \leq 0 \tag{3.23}$$

$$\phi_{dI} = Y_I - \eta_I(d_I) \leq 0 \text{ for } I = 1, 2, 3 \tag{3.24}$$

and

$$\dot{d}_s \geq 0, \quad \phi_{ds} \leq 0, \quad \dot{d}_s \phi_{ds} = 0 \tag{3.25}$$

$$\dot{d}_I \geq 0, \quad \phi_{dI} \leq 0, \quad \dot{d}_I \phi_{dI} = 0 \text{ for } I = 1, 2, 3. \tag{3.26}$$

The subscripts s, 1, 2 and 3 again denote the damage surfaces and loading conditions in the shear, warp, horizontal weft and vertical weft directions respectively. The strain measures controlling damage growth are the damage driving forces. Their thermodynamic motivation is described in more detail in **Paper C**, but here it is simply stated that

$$Y_s = \frac{1}{2}\boldsymbol{e}_{el} : \mathbb{E}_m : \boldsymbol{e}_{el} \quad \text{and} \quad Y_I = \frac{1}{2}\boldsymbol{\epsilon}_{el} : \mathbb{E}_{fI} : \boldsymbol{\epsilon}_{el} \text{ for } I = 1, 2, 3. \tag{3.27}$$

The four yield surfaces are once again defined with effective stress measures. In shear, the magnitude of the effective shear stress $\tilde{\boldsymbol{s}}$ is used, i.e.

$$\frac{1}{\sqrt{2}}|\tilde{\boldsymbol{s}}| = \frac{1}{\sqrt{2}}\sqrt{\tilde{\boldsymbol{s}} : \tilde{\boldsymbol{s}}}. \tag{3.28}$$

In the reinforcement directions, the magnitude of the effective normal stress in each reinforcement direction is used. This is denoted and computed as

$$|\tilde{T}^I| = |\tilde{\boldsymbol{\sigma}} : \boldsymbol{A}^I|. \tag{3.29}$$

The four yield surfaces along with their respective hardening variables and flow rules can then be expressed as

$$\phi_{ps} = \frac{1}{\sqrt{2}} |\tilde{\boldsymbol{s}}| - \tau_y - \kappa_s(k_s) \leq 0 \tag{3.30}$$

$$\phi_{pI} = |\tilde{T}^I| - \sigma_{yI} - \kappa_I(k_I) \leq 0 \text{ for } I = 1, 2, 3, \tag{3.31}$$

$$\dot{\boldsymbol{e}}_p = \dot{\lambda}_s \frac{\partial \phi_{ps}}{\partial \tilde{\boldsymbol{\sigma}}} = \dot{\lambda}_s \frac{\tilde{\boldsymbol{s}}}{\sqrt{2}|\tilde{\boldsymbol{s}}|} \tag{3.32}$$

$$\dot{\boldsymbol{\epsilon}}_{pI} = \dot{\lambda}_I \frac{\partial \phi_{p,I}}{\partial \tilde{\boldsymbol{\sigma}}} = \dot{\lambda}_I \text{sgn}(\tilde{T}^I) \boldsymbol{A}^I \text{ for } I = 1, 2, 3 \tag{3.33}$$

$$\dot{k}_s = \dot{\lambda}_s \frac{\partial \phi_{p,s}}{\partial \kappa_s} = -\dot{\lambda}_s \tag{3.34}$$

$$\dot{k}_I = \dot{\lambda}_I \frac{\partial \phi_{p,I}}{\partial \kappa^I} = -\dot{\lambda}_I \text{ for } I = 1, 2, 3. \tag{3.35}$$

Note also, that since $\boldsymbol{A}^I : \boldsymbol{A}^J = 0$ and $\boldsymbol{A}^I : \boldsymbol{e} = 0$, the total plastic strain is then

$$\boldsymbol{\epsilon}_p = \boldsymbol{e}_p + \sum_{I=1}^{3} \boldsymbol{\epsilon}_{p,I}. \tag{3.36}$$

Finally, the loading conditions are

$$\dot{\lambda}_s \geq 0, \quad \phi_{p,s} \leq 0, \quad \dot{\lambda}_s \phi_{p,s} = 0 \tag{3.37}$$

$$\dot{\lambda}_I \geq 0, \quad \phi_{p,I} \leq 0, \quad \dot{\lambda}_I \phi_{p,I} = 0 \text{ for } I = 1, 2, 3. \tag{3.38}$$

To fully calibrate this model, the yield stresses in shear τ_y and in each reinforcement direction σ_{yI} must be determined. Functions which define the development of the isotropic hardening stresses $\kappa_s(k_s)$ and $\kappa_I(k_I)$ are also needed along with expressions for $\eta_s(d_s)$ and $\eta_I(d_I)$. These can be determined from experimental tests with the same process outlined in Section 3.3.1 independently for each loading mode.

3.3.3 Required Experimental Tests and Model Results

The elasto-plastic and continuum damage model developed in **Paper C** and presented in Section 3.3.2 can be calibrated based on uniaxial tests with unloading cycles. Specifically, a tensile test with unloading is required in each of the reinforcement directions along with a test with unloading cycles in shear. Once again, parameter identification is possible with relative ease for the in-plane properties. Figures 3.11, 3.12 and 3.13 show experimentally obtained stress-strain curves for the **FiberDuk** material. Due to limitations in the test campaign, only one cyclic test was performed for each case. The parameter identification

routine outlined in Figure 3.10 has been carried out, where the obtained results are also shown in the same figures.

Under tensile loading in the warp direction, it is clear in Figure 3.11 that there is no detectable loss of stiffness as the test progresses. In fact, the stiffness increases slightly. Tracking the inelastic strain shows that it is necessary to account for plasticity. However, the test also indicates that in the warp direction, linear isotropic hardening is sufficient. The numerical values of the hardening modulus H_1 and yield stress σ_{y1} are given in Table 3.3.

Following the calibration procedure in the horizontal weft direction gives the results in Figure 3.12. The material shows a noticeable degradation in stiffness which is well described by an exponential curve with saturation. Consider the DIC images obtained during this test, shown in Figure 3.14. Each image is taken at the start of an unloading cycle. Damage and cracking begin to appear inside the yarns running horizontally. This spreads further to multiple yarns until there is a saturation of the damage before final failure takes place. In Figure 3.12 there is also a clear development of permanent strain. Again, linear hardening is sufficient. The identified parameters for the damage model and plasticity model are given in Tables 3.2 and 3.3 respectively.

Finally, an Iosipescu shear test with unloading cycles is shown in Figure 3.13. Once again, the material shows a progressive degradation in stiffness that can be described by an exponential damage evolution with softening. The development of permanent strain in this case however also needs to be described using an exponential hardening curve with saturation. This is summarised in Tables 3.2 and 3.3.

The model has been implemented with the identified parameters in an Abaqus user material routine (UMAT). The model fit considering each uniaxial loading mode is shown in Figure 3.15. For in-plane loading in the warp, horizontal weft and shear directions, good agreement is found between the model and experimental results. However, as in the previous sections, identifying out-of-plane material parameters using standardised testing techniques is not straightforward. The use of mesoscale models to overcome this challenge is explored further in **Paper E**.

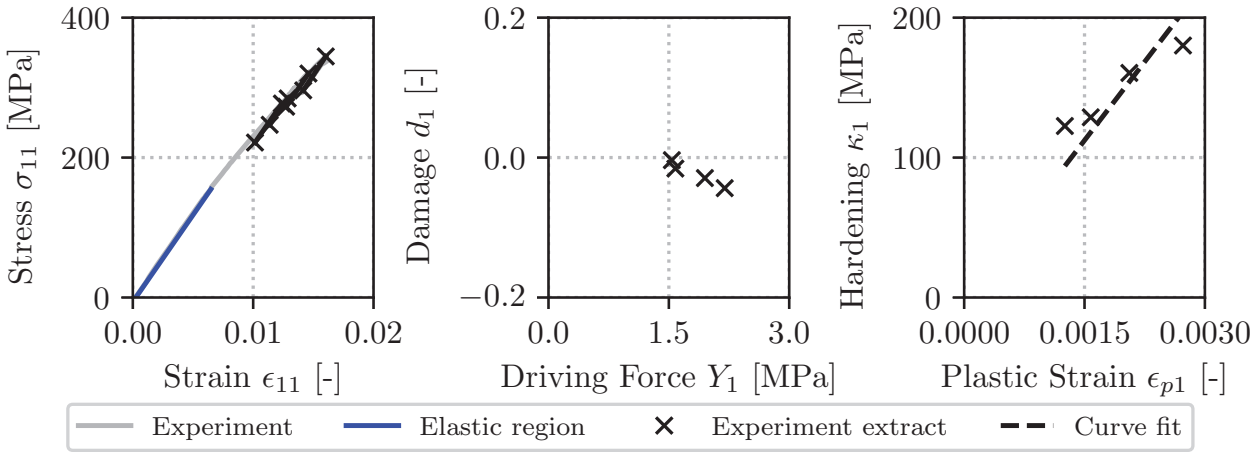

Figure 3.11: *Parameter identification routine carried out on uniaxial test in the warp direction.*

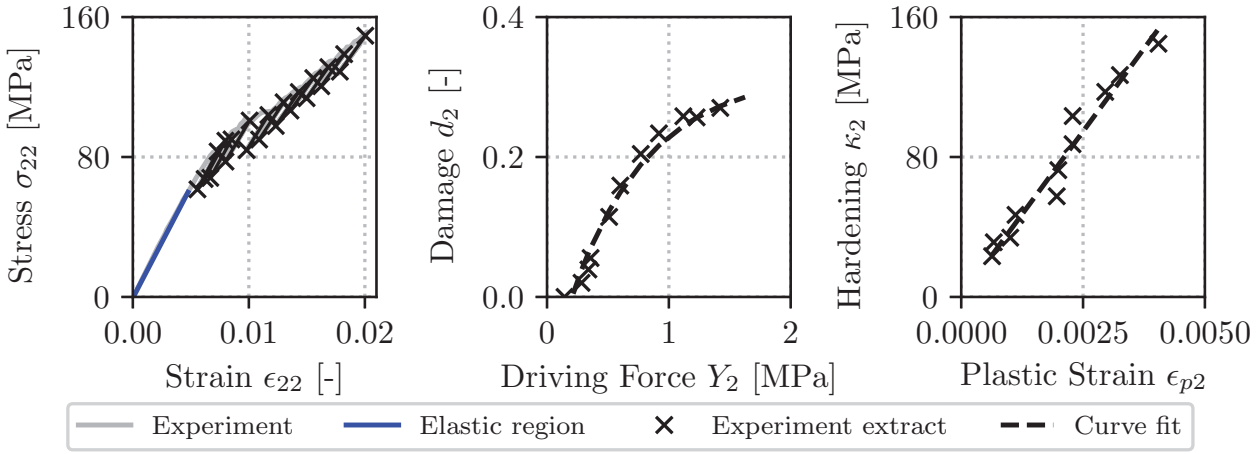

Figure 3.12: *Parameter identification routine carried out on uniaxial test in the horizontal weft direction.*

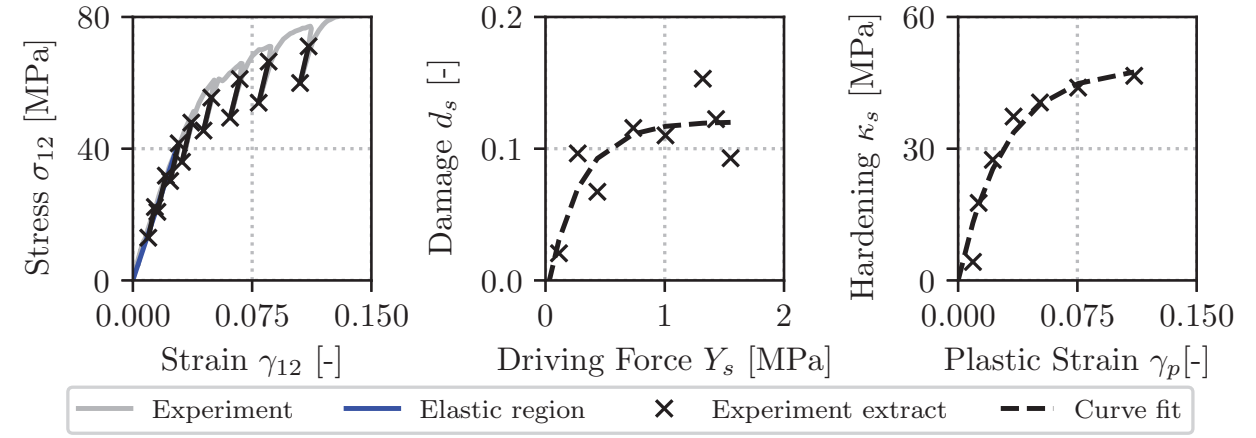

Figure 3.13: *Parameter identification routine carried out on uniaxial test in the in-plane shear direction.*

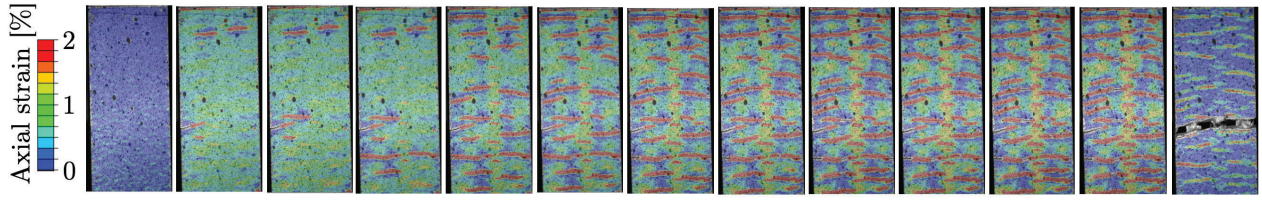

Figure 3.14: *DIC images of the cyclic tensile test in the horizontal weft direction. The images are taken at the beginning of each unloading cycle. The colour bar indicates the axial strain.*

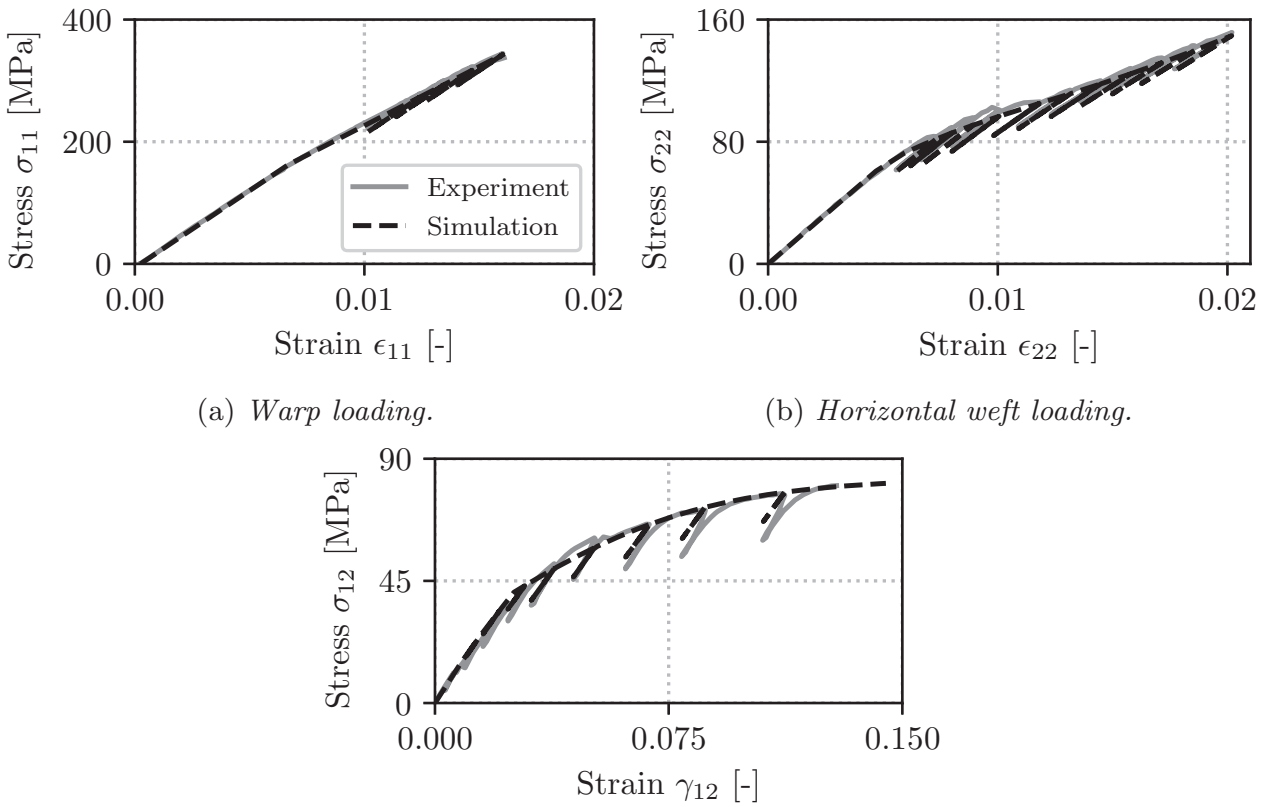

(a) *Warp loading.*

(b) *Horizontal weft loading.*

(c) *In-plane shear loading.*

Figure 3.15: *Comparison of the model predictions and experimental test results.*

Table 3.2: The damage parameters.

Direction	Damage variable	Parameters
Warp	$d_1 = 0$	-
Horizontal weft	$d_2 = d_{sat,2}\left(1 - e^{-b_2(Y_2 - Y_{0,2})}\right)$	$Y_{0,2} = 0.20$ [MPa] $b_2 = 2.20$ [1/MPa] $d_{sat,2} = 0.29$ [-]
Shear	$d_s = d_{sat,s}\left(1 - e^{-b_s(Y_s - Y_{0,s})}\right)$	$Y_{0,s} = 0.03$ [MPa] $b_s = 3.63$ [1/MPa] $d_{sat,s} = 0.12$ [-]

Table 3.3: The plasticity parameters.

Direction	Hardening law	Parameters
Warp	$\kappa_1 = -H_1 k_1$	$H_1 = 81.8$ [GPa] $\sigma_{y,1} = 161$ [MPa]
Horizontal weft	$\kappa_2 = -H_2 k_2$	$H_2 = 37.8$ [GPa] $\sigma_{y,2} = 59.9$ [MPa]
Shear	$\kappa_s = \kappa_{sat,s}\left(1 - e^{c_s k_s}\right)$	$\kappa_{sat,s} = 48.6$ [MPa] $\tau_y = 45.4$ [MPa], $c_s = 33.8$ [-]

3.4 Limitations and Future Work

There are limitations that exist, and should be dealt with cautiously for both the viscoelastic and combined elasto-plastic damage approaches. A number of these limitations are shared by both models. To begin with, the use of the constitutive framework developed in Section 2.2, provides a convenient basis to conceptualise the anisotropy of 3D-woven composites. The governing behaviours in each reinforcement direction and in shear can be considered and characterised separately. This, however, means that the shear behaviour is completely decoupled from the reinforcement behaviour. It has been shown in UD laminated composites, the apparent shear stiffness and strength increase under hydrostatic loads. See for example Shin and Pae [49]. Whether or not the shear response of the **FiberDuk** or **BAM** material is coupled to hydrostatic pressure, and the impact of multiple reinforcement directions, has not been quantified. Therefore for validation purposes, the testing campaign of the **FiberDuk** material also involved cyclic off-axis tensile testing at 10° to the horizontal weft direction. Both the viscoelastic and combined elasto-plastic damage modelling approaches showed good agreement to the experimental off-axis results, cf. Figure 3.16. The figure also indicates the boundary conditions and specimen size used in the considered finite element model. This hints toward the fact that under moderate combined normal and shear loading, the models perform well.

While the shear and reinforcement related behaviours are completely decoupled, the reinforcement related non-linear behaviour are coupled. It is not inconceivable that damage and/or permanent strain growth in one reinforcement direction will impact the characteristics of another reinforcement direction. The non-linear behaviour of the **FiberDuk** material in each reinforcement direction can be characterised with relative certainty from standardised experimental tests. How the material behaves under complex multiaxial loading scenarios however, is not so straightforward to consider.

One of the main goals of the **VIRTEST-3D** project was in fact to help answer these questions. The project is still underway, however multiple off-axis tensile tests will be carried out at different orientations. This will induce different combinations of tensile normal and shear loading to gain a deeper understanding of how different non-linear phenomena are coupled to one another. The 3D-woven mesoscale model of the **BAM** material will also be loaded multiaxially to help understand the couplings between

different non-linear mechanisms. Finally, the mesoscale model will also be used to address the limited out-of-plane shear behaviour. As it stands now, both the viscoelastic and elasto-plastic damage model assume that the non-linear shear behaviour of the 3D-woven composites is equivalent in each shear plane.

The lack of out-of-plane shear data is not the only challenge or limitation related to characterising the non-linear shear behaviour of 3D-woven composites. Consider the stress-strain curve of the in-plane Iosipescu test in Figure 2.3c. While the initial behaviour is consistent, once damage and inelastic phenomena begin to develop, a strong variation in test results is apparent. One of the main challenges with this test relates to the size of the representative unit cell, which is notably large given the size of the gauge region and region of uniform shear strain. This means that the placement of the yarns within this gauge region can impact how and where different non-linear phenomena localise and develop.

Further, in a homogeneous, small strain setting, it is assumed that the shear behaviour is symmetric in each shear plane. This means that the 12-shear and 21-shear behaviour should be equivalent. From Figure 3.17 it is clear that is not the case. The woven mesostructure creates a material with a strong directional preference for strain localisation oriented by the warp yarns. When the warp yarns are oriented vertically however, the material shows a clear vertical shear strain localisation in the gauge region. For this reason, the shear behaviour in both the viscoelastic and elasto-plastic damage approach was calibrated using an Iosipescu test with vertically oriented warp yarns. In a traditional continuum mechanics framework, accounting for such behaviour is not possible. It requires the consideration of for example, micropolar theories, cf. Hasanyan [50].

The nature of a macroscale model also means that it is not possible to capture strain localisation. See for example Figure 3.14, which shows a selection of DIC images of the cyclic tensile test in the horizontal weft direction for the **FiberDuk** material. The colour index represents the resulting axial strain field of the experiment and simulation. When simulating a tensile test, the model will simply predict a constant strain distribution. It

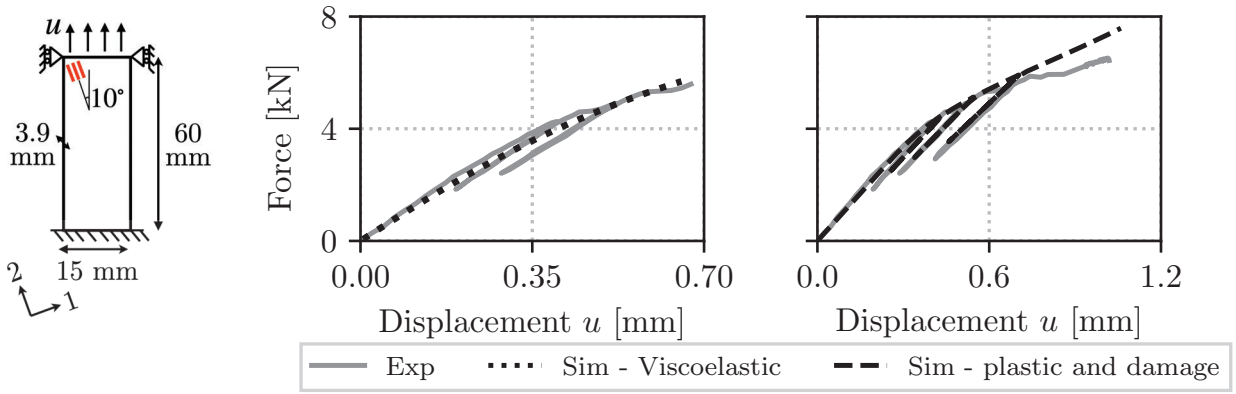

Figure 3.16: *Comparison of the experimental and simulation results for a* 10° *off-axis tensile test. Both the predicted behaviour of the viscoelastic as well as the elasto-plastic and damage approach are shown. The considered boundary conditions of the finite element model are also shown along with the specimen dimensions.*

can be noted that while macroscale models can provide a good fit of the global response can be obtained, an equally exact comparison of the axial and shear strain distributions is more challenging.

Turning to the limitations of the viscoelasticity model on its own, it should once again be pointed out, that the Norton model is essentially a Maxwell model with a non-linear viscous damper. This means that given enough time, it will relax to a state of zero stress. To further improve the model, additional testing should be done to characterise the relaxation and creep behaviour of the material. Rheologically speaking, it would then be possible to, add additional springs to prevent complete relaxation in the reinforcement directions. As it stands now, the model is calibrated using monotonic tensile and shear tests. This has produced a model which shows a strong strain rate dependence, likely more so than what is reasonable for a 3D-woven composites. This model is therefore limited to being used to predict tests carried out in a very narrow band of applicable loading rates.

The elasto-plasticity and damage model has its own challenges and limitations. First, consider the Voigt form of the damaged stiffness tensor from Equation (3.22). When the local reinforcement directions are oriented along the global coordinate axes,

$$\underline{\underline{\mathbb{E}}} = \begin{bmatrix} (1-d_1)C_{11} & (1-d_1)(1-d_2)C_{12} & (1-d_1)(1-d_3)C_{13} & 0 & 0 & 0 \\ (1-d_1)(1-d_2)C_{12} & (1-d_2)C_{22} & (1-d_2)(1-d_3)C_{13} & 0 & 0 & 0 \\ (1-d_1)(1-d_3)C_{13} & (1-d_2)(1-d_3)C_{23} & (1-d_3)C_{33} & 0 & 0 & 0 \\ 0 & 0 & 0 & (1-d_s)C_{44} & 0 & 0 \\ 0 & 0 & 0 & 0 & (1-d_s)C_{55} & 0 \\ 0 & 0 & 0 & 0 & 0 & (1-d_s)C_{66} \end{bmatrix}. \tag{3.39}$$

The elastic components of the stiffness tensor, i.e. those shown in Equation (2.1) are denoted as C_{ij} for simplicity. One limitation that becomes apparent, is that even as damage develops, the orthotropy of the stiffness tensor is maintained. Further, as the damage variables grow, the 3D stress-strain constitutive relationship diverges from the

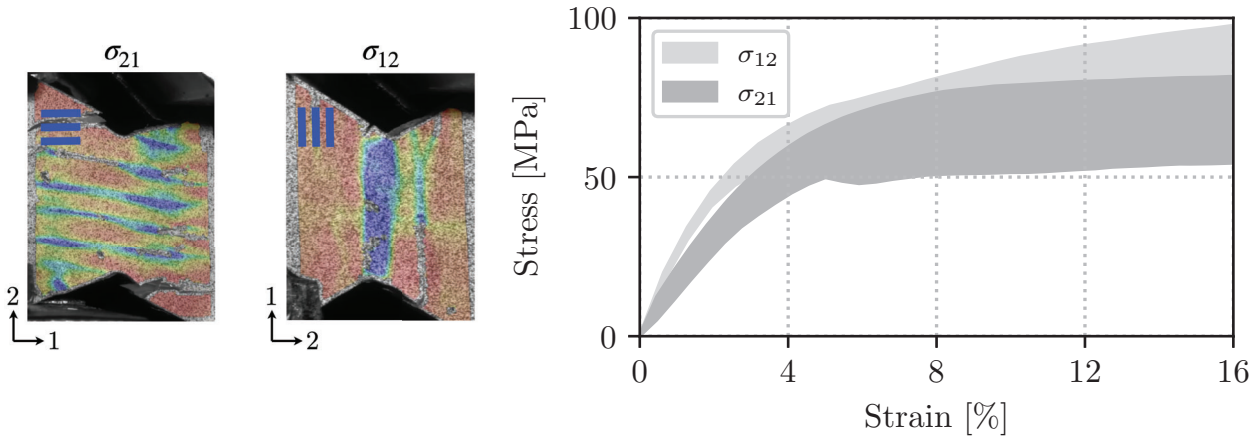

(a) *DIC images of the shear strain field localisation.*

(b) *Experimental spread of the stress-strain curves.*

Figure 3.17: *Comparing the shear behaviour of an Iosipescu test with different reinforcement orientations. Horizontally oriented warp yarns corresponds to* σ_{21}*. Vertically oriented warp yarns corresponds to* σ_{12}*.*

idealised 1D problems used to calibrate the model. In the event that damage saturates at higher values than what is shown in Section 3.3.3, modifications to the 1D calibrate routine should be considered.

A relatively straightforward place for improvement within the model calibration is the use of either acoustic emissions or accelerometer data. The onset of damage and plasticity as it stand now, is selected based on when the stress-strain curves show visible non-linear behaviour. Future experimental campaigns should consider using such techniques to help pinpoint damage onset. A far more challenging but crucial path for model development, is the consideration of compressive material behaviour. This must involve not only understanding the effects of crack closures under compressive loads, but also how inelastic and damage mechanisms develop in compression.

Paper B and **Paper C** take two separate approaches to predicting the non-linear behaviour of 3D-woven composites. In **Paper B** it is assumed that all non-linearity is due to viscous effects. **Paper C** on the other hand assumes that it is due to a combination of plasticity and damage. In reality, it is possible that the non-linear behaviour of 3D-woven composites is due to all three mechanisms. Developing a viscoplastic model of this nature however, would require characterising and differentiating between both rate dependent and rate independent properties. One interesting test to consider for future campaigns is that introduced by Zscheyge et al. [51]. They use a so called *stepwise loading-unloading test with relaxation and retardation periods*. The test routine is illustrated in Figure 3.18a. It involves:

1. A displacement controlled loading period to a certain strain limit.
2. A stress relaxation period at this strain level.
3. A force controlled unloading period to an external force of zero.
4. A strain retardation period at zero force.
5. Repeating steps 1 through 4 at higher strain levels.

Figure 3.18b shows an illustrative 1D stress-strain curve produced by such a testing method. The non-linearity due to rate-independent inelasticity, rate-dependent inelasticity and damage can be quantified directly through this single test.

4 Region III: Failure Initiation, Softening and Final Failure

In a tensile test along one of the reinforcement directions, 3D-woven composites often show a region in which both inelastic and damage mechanism develop in a progressive and controlled manner. Eventually, the reinforcement yarns will snap, which leads to an aggressive and abrupt final failure of the tensile specimen. However, as discussed by Laurin et al. [52], on the structural scale, especially for test samples containing geometric singularities, this is not the case. Although failure may initiate in one location of the

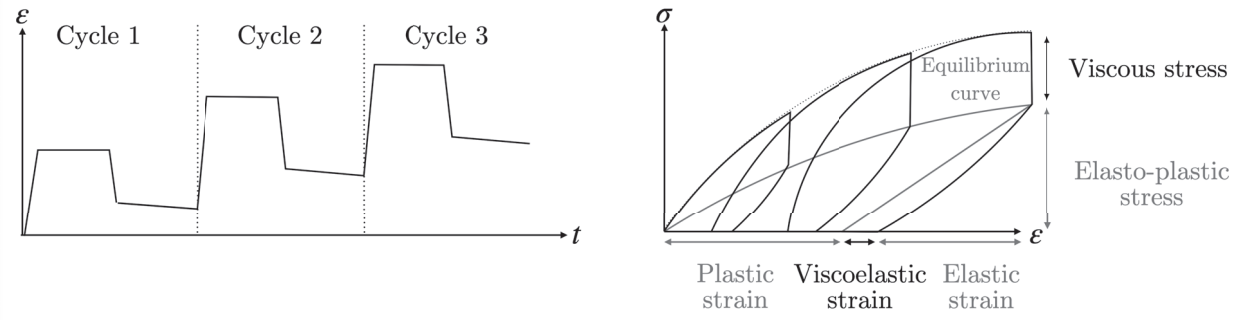

(a) *Strain-time plot.* (b) *Stress-strain plot.*

Figure 3.18: *Illustration of the stepwise loading-unloading test with relaxation and retardation periods. The stress-strain plot shows both a schematic of a resulting curve from an experiment as well as how to obtain the equilibrium relation which is used to understand how the rate-independent part of a model can be developed.*

component, this does not necessarily mean that the component itself has failed. More importantly, it is then necessary to predict both local failure initiation and describe the softening behaviour at the locations where failure has initiated. Otherwise it is likely that the overall stiffness of the component will be overestimated.

4.1 Non-Local Damage Models

Standard continuum damage models, as introduced in Section 3.1, are referred to as local damage models. The damage variables are strictly dependent on the local strain field history at each material point. The main advantage of local damage models is their simplicity. They are relatively straightforward to conceptualise, calibrate and implement. Local damage models, however, have one major downfall. They should not be used in a rate independent form to soften the constitutive material model, i.e. there should not be a decrease in stress.

To illustrate why this is a problem, consider the bar shown in Figure 4.1a, which is discussed by Jirásek and Bažant [53]. It is exhibiting a displacement u on the right hand boundary. The material is assumed to show linear elasticity up to a peak stress σ_{max}, followed by linear softening. This is illustrated in Figure 4.1b. Equilibrium relationships require that the axial force and therefore stress remain uniform along the bar. Upon loading, as long as the stress remains below σ_{max}, everything is perfectly fine. Once the maximum stress is reached, the challenges start. For a given stress $\bar{\sigma}$, there are now two possible strain values, illustrated in Figure 4.1b, which satisfy the constitutive equations. Conceptually, this is reasonable. A cross section of the bar will either be undamaged and unload along the elastic path or be damaged and unload along the softening branch of the constitutive stress-strain curve.

The main issue here is the fact that no information is given to quantify the length of the damaged cross section. When the stress is completely relaxed, the force-displacement behaviour has an infinite number of possible solutions, cf. Figure 4.1c. The post-peak branches are bound by the limit cases of a fully damaged bar on the right, or a bar with

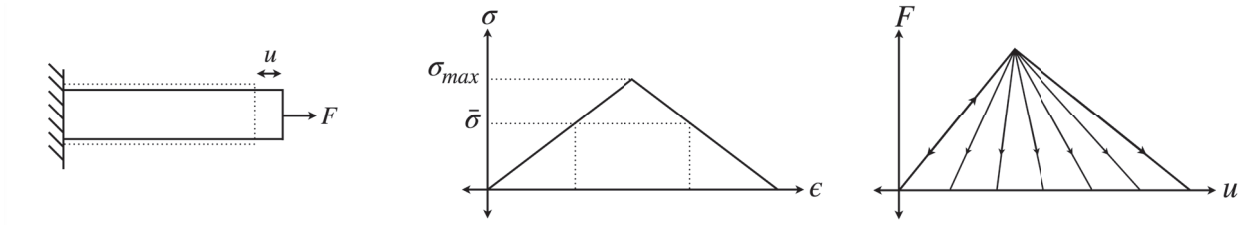

(a) *Illustration of a bar experiencing uniaxial tension.* (b) *Stress-strain diagram with linear softening.* (c) *Illustration of possible post-peak branches.*

Figure 4.1: *Schematic illustrating the challenges associated with the use of a local damage model to cause softening.*

an infinitely small damaged zone on the left. All cases in between describe varying sizes of the damaged zone.

Mathematically, this problematic feature is described as a loss of ellipticity of the governing equations, cf. [54]. The boundary value problem becomes ill-posed and as such, there is no longer a unique solution. Numerically, in a finite-element problem this manifests itself as a pathological mesh dependence. The strain softening, i.e. damage, will localise in a single row of elements (in simple examples where the crack path is well defined). As the mesh is refined, the damaged region decreases. The post-peak branch of the force-displacement curve will approach the elastic solution with an abrupt failure and the amount of dissipated energy will progressively decrease.

One straightforward method to circumvent some of these challenges is to add viscous regularisation to the damage variables, see for example Ladevèze [55]. While this is relatively easy to implement, there is a trade-off. The viscous effects cause a delay in the onset and development of damage while also adding an additional dissipative mechanism. A compromise must then be made between adding enough viscous damping to minimise the pathological mesh dependence but not so much such that the artificial dissipation becomes unphysical.

Another option is to regularise the problem using the crack band method introduced by Bažant and Oh [56]. The crack band method introduces a length parameter (typically the characteristic length of the finite element) to achieve a constant energy release per unit crack area regardless of element dimension. It should in fact be noted that in their mesoscale model for 3D-woven composites, El Said et al. [47] as well as Topalidis et al. [26] employ such an energy regularisation to mitigate mesh dependencies. The crack band method is not foolproof. In circumstances where the localisation aligns with the finite element discretisation it does allow for the correct energy dissipating and mesh convergent force-displacement results. However, the width and orientation of the numerically resolved localised damage zone as well as the dissipated energy, is still dependent on the size and orientation of the finite element mesh. See for example Mukhopadhyay and Hallett [57], Leong et al. [58] or Främby and Fagerström [59].

To truly resolve these issues related to mesh dependence and strain softening, non-local damage theories are needed. As the name suggests, non-local theories abandon the idea that the stress at a certain point is only dependent on the strain and state variables at that point. One of the earlier examples of such a model was proposed by Pijaudier-Cabot and Bažant [60]. Sometimes referred to as an integral-type non-local model, they propose

that the strain measure controlling damage growth be replaced with its weighted spatial average over a representative volume. On the plus side, these models are fairly easy to conceptualise. Kinematic and equilibrium relations remain the same, and the stress and strain keep their standard meaning. In a commercial FE code however, they are more challenging to implement as you need to be able to access information stored in neighbouring integration points.

A close relative to the integral-type non-local models are the gradient enhanced approaches, see e.g. Peerlings et al. [61]. As the name suggests, these approaches account for non-local effects by adding a gradient enhancement to the strain measure used to drive damage development. While traditional gradient enhanced models have their foundations in damage mechanics, another method known as the phase-field approach begins from a discontinuous description of the damage field. See for example [62] or [63]. Within the phase-field framework, a discrete crack is approximated using a scalar continuous field variable that localises into a band of defined width. As discussed by de Borst and Verhoosel [64] gradient enhanced and phase-field approaches come from different points of departure. However, they are almost identical in terms of their mathematical structure. Both can be implemented in commercial FE software as user-defined elements.

Non-local damage approaches have been applied to 3D-woven composite materials on the macroscale. Marcin [65] for example combined a gradient enhanced model with viscous regularisation. They considered an open hole plate under tensile loading, manufactured using a 3D-woven ceramic matrix composite. When only considering a gradient enhanced approach, they found that the force-displacement behaviour showed snap-back after reaching the peak load. The presence of snap-back required the use of the more advanced arc-length solution method to resolve the problem. Strictly using a viscous regularisation on the other hand leads to a far more progressive material softening, with much higher energy dissipation and a strong dependence on the local loading rate. Combining both methods minimised the inconveniences of both approaches, while producing a more realistic post peak behaviour. More recently, Médeau [66] and Laurin et al. [52] evaluated and compared various regularised and non-local damage models. This included a phase-field modelling approach for damage and strength predictions of 3D-woven polymer matrix composites. Their model was able to successfully simulate and reproduce the observed failure behaviours of compact tension as well as single-edge notched beam specimens.

A phase-field approach is also proposed in **Paper D** to predict local softening and final failure of 3D-woven composites. It is largely an extension of the elasto-plastic damage model presented in Section 3.3. In particular, the phase-field is formulated such that it can evolve in an anisotropic manner, and accommodate a fracture toughness that depends on the final mode of failure. This will be discussed in Section 4.3.2. First however, phase-field models will be briefly introduced for isotropic materials that show brittle fracture.

4.2 Isotropic Phase-Field Modelling of Brittle Fracture

The point of departure for phase-field models is Griffith's fracture theory, cf. Zehnder [67] for example. It considers fracture as an interaction between the elastic energy stored

in the bulk material and the amount of energy required to generate a new crack surface. The internal potential energy of a solid body can then be described with contributions from the strain energy of the bulk material E and the fracture energy W, where

$$\Pi^{int} = E + W. \tag{4.1}$$

Consider first the fracture energy. For a discrete crack with a surface described by Γ, illustrated in Figure 4.2a, inside a domain with volume Ω, this is described as

$$W = \int_{\Gamma} g_c \, \mathrm{d}\Gamma. \tag{4.2}$$

The property g_c is referred to as the critical energy release rate or fracture toughness. It represents the amount of energy associated with the formation of one unit of new crack surface. As previously stated however, this represents a discrete description of the damage. The material is either completely intact or completely damaged. In order to go from a discrete description of fracture to one which describes a smooth transition between a fully intact material, a phase-field $\bar{d}$ is introduced. As with the continuum damage models, it is assumed that $\bar{d} = 1$ signifies that the material is completely damaged while $\bar{d} = 0$ signifies that the material is intact.

To describe this transition in more detail, it is convenient to once again return to considering a bar problem illustrated in Figure 4.2b. The bar has a volume Ω with a crack defined by the cross-sectional area Γ. A diffuse description of the crack can then be represented with a number of functions. As discussed by Wu [68], some standard examples found in the literature are:

- **AT2**: $\bar{d}(x) = e^{-|x|/l_c}$. The abbreviation AT refers to Ambrosio-Tortorelli [69]. This is one of the most widely adopted descriptions of the crack phase-field functions. It has been used by for example Bourdin et al. [70], Kuhn et al. [71].
- **AT1**: $\bar{d}(x) = \left(1 - \frac{|x|}{2l_c}\right)^2$. The AT1 geometric crack function has been used by for example Pham et al. [72] and Bourdin et al. [73].
- **PFCZM**: $\bar{d}(x) = 1 - \sin\left(\frac{|x|}{l_c}\right)$. Here the abbreviation stands for *Phase-Field Regularised Cohesive Zone Model*. It was presented and advocated for by Wu [74].

They are illustrated in Figure 4.3a. Note that they all involve the introduction of a length scale parameter l_c which defines the length over which the phase-field is diffused. One of the largest advantages of adopting the AT2 geometric crack function relates to the fact that it is automatically bound between zero and one. More specifically, the AT2 function satisfies the boundary conditions

$$\bar{d}(x) \in [0, 1], \;\; \bar{d}(\pm\infty) = 0 \;\text{ and }\; \bar{d}(0) = 1. \tag{4.3}$$

As the phase-field is now described as a non-discrete diffuse damage band, the integral definition of the fracture energy W must be modified. This is done using what is referred to as a crack density function γ. The aim is then to be able to express

$$W = \int_{\Gamma} g_c \, \mathrm{d}\Gamma = \int_{\Omega} g_c \gamma(\bar{d}, \nabla\bar{d}) \, \mathrm{d}\Omega. \tag{4.4}$$

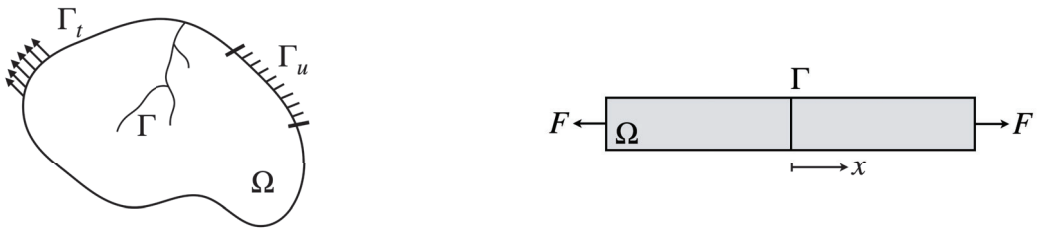

(a) *A cracked domain with volume* Ω. (b) *A cracked bar with volume* Ω.

Figure 4.2: *Illustration of the considered domains and their boundaries.*

Since it is the most common option, consider again the 1D, AT2 description of the phase-field geometry. The crack density function can be formulated by first considering that in 1D, $\bar{d}(x) = e^{-|x|/l_c}$ is the solution for the homogeneous differential equation

$$\bar{d}(x) - l_c^2 \bar{d}''(x) = 0 \tag{4.5}$$

with the boundary conditions in Equation (4.3). Equation (4.5) however, represents the strong form of the equation. In the variational approach to fracture, a functional is sought after such that the minimisation condition gives the ordinary differential equation in Equation (4.5). In this case, it is

$$I\left(\bar{d}\right) = \frac{1}{2}\int_\Omega \left(\bar{d}^2 + l_c^2 \bar{d}'^2\right)\, \mathrm{d}\Omega \tag{4.6}$$

with the additional property that $I\left(d = e^{-|x|/l_c}\right) = l_c\Gamma$.

Therefore

$$W = \int_\Gamma g_c\, \mathrm{d}\Gamma = \int_\Omega g_c \frac{1}{2l_c}\left(\bar{d}^2 + l_c^2 \bar{d}'^2\right)\, \mathrm{d}\Omega = \int_\Omega g_c \gamma\left(\bar{d}, \bar{d}'\right)\, \mathrm{d}\Omega. \tag{4.7}$$

Generalising to multiple dimensions, the crack density function can then be expressed as

$$\gamma\left(\bar{d}, \nabla\bar{d}\right) = \frac{1}{2l_c}\bar{d}^2 + \frac{l_c}{2}\left|\nabla\bar{d}\right|^2. \tag{4.8}$$

A similar argumentation strategy can be followed when considering either the AT1 or PFCZM geometric phase-field expressions.

Turning to the strain energy, the next step takes inspiration from continuum damage mechanics. It is assumed once again that as the phase-field grows, the material looses stiffness. This loss of stiffness is expressed through some form of degradation function $g(\bar{d})$. Then

$$E = \int_\Omega g(\bar{d})\Psi\, \mathrm{d}\Omega. \tag{4.9}$$

For a linear elastic material with a fourth order elastic stiffness tensor $\mathbb{E}$,

$$\Psi = \frac{1}{2}\boldsymbol{\epsilon} : \mathbb{E} : \boldsymbol{\epsilon}. \tag{4.10}$$

This corresponds to a constitutive stress-strain relationship given by

$$\boldsymbol{\sigma} = g(\bar{d})\mathbb{E} : \boldsymbol{\epsilon}. \tag{4.11}$$

Unlike traditional local damage models, the degradation function must satisfy the following conditions:

- $g(0) = 1$ signifying an intact state and $g(1) = 0$ signifying a completely damaged state.
- $g'(\bar{d}) < 0$ i.e. the degradation function must decrease monotonically.
- $g'(1) = 0$ which ensures that the phase-field driving force vanishes when $\bar{d} = 1$. This is in fact one of the major differences to gradient enhanced damage models. It ensures that the damage zone does not continue to broaden orthogonally in the wake of the crack tip.

A few common examples include:

1. **Quadratic polynomial**: $g(\bar{d}) = \left(1 - \bar{d}\right)^2$. This degradation function is widely used for brittle fracture. It was introduced by Bourdin et al. [75] and is plotted in Figure 4.3b.
2. **Cubic polynomial**: $g(\bar{d}) = 3\left(1 - \bar{d}\right)^2 - 2\left(1 - \bar{d}\right)^3$. Karma et al. [76] introduced this degradation function. It is plotted in Figure 4.3b. The use of a cubic polynomial means that $g(\bar{d})$ shows a less abrupt drop when the phase-field begins developing. This means that the material will show a more defined initial elastic region.
3. **Quartic polynomial**: $g(\bar{d}) = 4\left(1 - \bar{d}\right)^3 - 3\left(1 - \bar{d}\right)^4$. Introduced by Kuhn et al. [71], the quartic function again slows the onset of the stiffness degradation. This is illustrated in Figure 4.3b.

As it is the most common choice, the quadratic polynomial will be considered from this point forward.

To prevent material healing, irreversibility of the phase-field during loading and unloading must be ensured. One option introduced by Miehe et al. [77], and the approach taken here, is to introduce a history variable where

$$\mathcal{H}_\Psi = \max_{\tau \in [0,t]} \Psi(\epsilon_{el}). \tag{4.12}$$

This represents the maximum total elastic energy obtained in the loading process. It allows for the decoupling of the governing system of equations and the use of a staggered solution scheme, which is considered computationally robust for phase-field models. Note, however, that enforcing irreversibility with a history variable in this manner is not applicable for the AT1 and PFCZM geometric crack functions.

As shown by Molnár and Gravouil [78], the functional used to solve for the phase-field is then given by

$$\Pi^{int} \approx \Pi^{\bar{d}} = \int_\Omega \left[g_c \gamma(\bar{d}, \nabla\bar{d}) + g(\bar{d})\mathcal{H}_\Psi \right] \, \mathrm{d}\Omega. \tag{4.13}$$

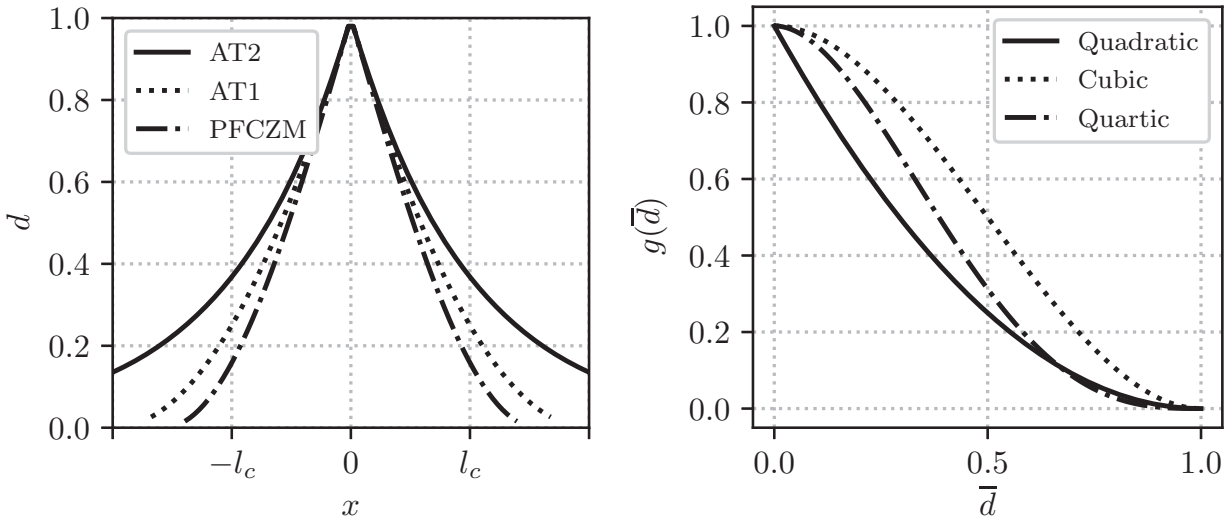

(a) *Geometric crack functions.* (b) *Degradation functions.*

Figure 4.3: *Illustration of common geometric crack functions and degradation functions for phase-field models.*

Assuming the external component of the potential energy can be formulated as

$$\Pi^{ext} = \int_{\Omega} \boldsymbol{b} \cdot \boldsymbol{u} \, \mathrm{d}\Omega + \int_{\Gamma_u \cup \Gamma_t} \boldsymbol{t} \cdot \boldsymbol{u} \, \mathrm{d}\Gamma \tag{4.14}$$

with body force $\boldsymbol{b}$ and boundary traction $\boldsymbol{t}$, then for a fixed $\bar{d}$ the displacement field can be solved from

$$\Pi^{u} = \int_{\Omega} \left[g(\bar{d})\Psi - \boldsymbol{b} \cdot \boldsymbol{u} \right] \, \mathrm{d}\Omega - \int_{\Gamma_u \cup \Gamma_t} \boldsymbol{t} \cdot \boldsymbol{u} \, \mathrm{d}\Gamma. \tag{4.15}$$

The strong form of the governing equations can be found by taking the variation of both energies, $\delta\Pi^{\bar{d}}$ and $\delta\Pi^{u}$. Then

$$\nabla \boldsymbol{\sigma} + \boldsymbol{b} = 0 \quad \text{in} \quad \Omega \quad \text{and} \quad \boldsymbol{\sigma} \cdot \boldsymbol{n} = \bar{\boldsymbol{t}} \text{ on } \Gamma_t, \quad \boldsymbol{u} = \bar{\boldsymbol{u}} \text{ on } \Gamma_u \tag{4.16}$$

and

$$\frac{g_c}{l_c} \left(\bar{d} - l_c^2 \Delta \bar{d} \right) = 2 \left(1 - \bar{d} \right) \mathcal{H}_{\Psi} \quad \text{and} \quad \nabla \bar{d} \cdot \boldsymbol{n} = 0 \text{ on } \Gamma, \tag{4.17}$$

where the Laplacian operator $\Delta(\bullet) = \nabla \cdot \nabla(\bullet)$ and $\boldsymbol{n}$ is the outward facing normal. The constitutive stress-strain relation is

$$\boldsymbol{\sigma} = g(\bar{d}) \mathbb{E} : \boldsymbol{\epsilon}. \tag{4.18}$$

Phase-field modelling approaches are continuously growing in popularity. For more information on phase-field models, their development, uses and implementation Wu et al. [68] is strongly recommended. Further, for information on how to implement such a model

in commercial software see Molnár and Gravouil [78]. Phase-field models have a number of important benefits. In their purest form, as they are based on energy minimisation, they require no predefined assumptions on the crack location. Multiple cracks can initiate, propagate, branch and coalesce automatically. Further, and importantly for 3D-woven composites, this can be handled and implemented with relative ease in three dimensions (although it is computationally expensive).

4.3 Extending to Anisotropic Ductile Fracture of 3D-Woven Composites

A phase-field approach is proposed in **Paper D** to predict softening and final failure of 3D-woven composites. It builds on the anisotropic elasto-plastic damage model presented in Section 3.3. In this work, focus is given to three key challenges related to phase-field modelling of 3D-woven composites. They are:

1. **Failure initiation**: In the traditional approach outlined in Section 4.2, the phase-field begins developing immediately. In the current model the aim is to trigger the softening response, i.e. the phase-field, following a region of progressive damage and inelasticity. For this reason, a failure criterion must be introduced.

2. **Anisotropic failure**: The phase-field should develop in such a way that the fracture toughness can vary depending on the final mode of failure.

3. **Ductile fracture**: The energy functional is no longer strictly dependent on the elastic strain. A number of modelling choices then need to be made to account for the plasticity and continuum damage variables and their impact on phase-field development.

Each of these aspects will be discussed in a dedicated subsection before the strong form of the governing equations is stated.

4.3.1 Failure Initiation

Predicting failure initiation in fibre-reinforced composites is an ongoing research area. The most straightforward option is to use maximum stress or strain criteria. These however do not account for stress or strain interactions. Some of the earliest proposed criteria for UD composites that could account for such interactions were Tsai-Hill [79] and Tsai-Wu [80]. While different failure fractions are calculated according to the orthotropic nature of the material, for Tsai-Hill and Tsai-Wu they all accumulate to a single failure criterion. However, in UD composites, it has been proven to be quite important to distinguish between failure modes (fibre tension, fibre compression, matrix tension and matrix compression) using multiple criteria simultaneously. Further, the predicted failure mode determined by the criterion taking the highest value, is used to determine which stiffness components are degraded. Failure criteria for UD composites have continued to grow in complexity and completeness. See for example Cuntze and Freund [81], Pinho et al. [82] and Carrere [83]. Further, the criteria presented by Pinho et al. [82] commonly

referred to as LaRC05 can for example, account for pressure dependence, non-linear shear behaviour and in-situ effects.

In **Paper A** the application of LaRC05 to 3D-woven composites, is explored. The LaRC05 criteria, and many of its counterparts, are stress based and require that the criteria be computed in rotated frames of reference. It becomes apparent quite quickly, that the lack of a clear plane of material isotropy dominated by the properties of the matrix produces erroneous results. For this reason in **Paper A**, it is proposed that a set of strain-based criteria are used instead, which produces qualitatively more reasonable results.

As the research project progressed, it became increasingly apparent that the use of multiple failure criteria, each controlling the stiffness degradation of different components due to different failure modes, may be unnecessary. When failure initiates and propagates, this represents a complete loss of material integrity. For this reason, a single strain-based failure criterion is proposed in **Paper D**. Failure is therefore assumed to initiate when

$$FI = \left(\frac{\boldsymbol{\epsilon} : \boldsymbol{A}^1}{\epsilon_{1,max}}\right)^2 + \left(\frac{\boldsymbol{\epsilon} : \boldsymbol{A}^2}{\epsilon_{2,max}}\right)^2 + \left(\frac{\boldsymbol{\epsilon} : \boldsymbol{A}^3}{\epsilon_{3,max}}\right)^2 + \left(\frac{2|\boldsymbol{e}|}{\sqrt{2}\gamma_{max}}\right)^2 = 1. \tag{4.19}$$

The maximum strain values are denoted as $\epsilon_{1,max}$, $\epsilon_{2,max}$, $\epsilon_{3,max}$ and γ_{max} for the warp, horizontal weft, vertical weft and shear directions, respectively. When failure is initiated, the corresponding energy density Ψ_{init} is recorded and used as a threshold value to ensure the phase-field will not develop until a certain energy density is overcome.

The specific energy density for this model formulation will be discussed in more detail in Section 4.3.3. Using the threshold value, the history variable introduced in Equation (4.12) can instead be expressed as

$$\mathcal{H}_\Psi = \max_{\tau \in [0,t]} \langle \Psi - \Psi_{init} \rangle \tag{4.20}$$

where $\langle \bullet \rangle$ denotes a Macaulay bracket. Once again, the history variable enforces phase-field irreversibly and allows for an algorithmic decoupling of the governing system of equations.

4.3.2 Anisotropic Failure

Enforcing failure mode dependent critical energy release rates, can generally be done in two ways. The first option is to consider multiple phase-fields each linked to their own energy measure. This method is considered by for example Bleyer and Alessi [84] as well as Dean et al. [85]. Another possibility is the use of a single phase-field, with an anisotropic crack density function. This has been proposed by for example Teichtmeister et al. [86] and is also the approach adopted in **Paper D**.

The anisotropy of the crack density function is enforced using a structural tensor $\boldsymbol{A}^d$ where

$$\gamma\left(\bar{d}, \nabla\bar{d}\right) = \frac{1}{2l_c}\bar{d}^2 + \frac{l_c}{2}\nabla\bar{d} \cdot \boldsymbol{A}^d \cdot \nabla\bar{d}. \tag{4.21}$$

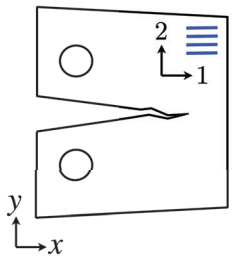

Figure 4.4: *Schematic showing a crack propagating in the direction of the warp yarns for a CT specimen.*

The structural tensor $\boldsymbol{A}^d$ is defined using the structural tensors which indicate the three reinforcement directions. Specifically

$$\boldsymbol{A}^d = \alpha_1 \boldsymbol{A}^1 + \alpha_2 \boldsymbol{A}^2 + \alpha_3 \boldsymbol{A}^3, \tag{4.22}$$

where the parameters α_1, α_2 and α_3 allow for directional dependent variations in the effective length scale parameter and critical energy release rate.

To demonstrate the influence that α_1, α_2 and α_3 have on the effective fracture toughness and length scale parameters, consider the case of a crack propagating in the warp direction (aligned with the x-axis) shown in Figure 4.4. The structural tensor is then

$$\boldsymbol{A}^d = \begin{bmatrix} \alpha_1 & 0 & 0 \\ 0 & \alpha_2 & 0 \\ 0 & 0 & \alpha_3 \end{bmatrix} \tag{4.23}$$

If the length scale of the phase-field is sufficiently small in comparison to the length of the crack and a location sufficiently far away from the crack tip is considered, the crack density function can be simplified. In this case

$$\frac{\partial \bar{d}}{\partial x} \approx \frac{\partial \bar{d}}{\partial z} \approx 0. \tag{4.24}$$

In turn, the crack density function can be expressed as

$$\gamma(\bar{d}, \nabla \bar{d}) = \frac{1}{2l_c}\bar{d}^2 + \frac{l_c \alpha_2}{2}\left(\frac{\partial \bar{d}}{\partial y}\right)^2. \tag{4.25}$$

Following the same steps in reverse from Equation (4.7) to the definition of the AT2 geometric crack function, means that Equation (4.25) corresponds to the phase-field value along the y-axis

$$\bar{d} = d^{-|y|/\sqrt{\alpha_2}\, l_c}. \tag{4.26}$$

Loading in the horizontal weft direction will therefore give an *effective* length scale $l_{c,2} = \sqrt{\alpha}_2 l_c$. Using similar argumentation, the dissipated energy per unit crack length in this loading mode is

$$g_{c,2} = \frac{g_c}{2l_c}\int_{-\infty}^{\infty} \left(\bar{d}^2 + \alpha_2 l_c^2 \bar{d}'^2\right) \mathrm{d}x. \tag{4.27}$$

Inserting Equation (4.26) and solving the integral gives

$$g_{c,2} = g_c\sqrt{\alpha_2}. \tag{4.28}$$

Analogously, the effective critical energy release rate and length scale for the warp and vertical weft directions are $l_{c,1} = \sqrt{\alpha}_1 l_c$, $g_{c,1} = g_c\sqrt{\alpha_1}$, $l_{c,3} = \sqrt{\alpha}_3 l_c$ and $g_{c,3} = g_c\sqrt{\alpha_3}$ respectively.

4.3.3 Ductile Failure and Strong Form

In brittle materials, it is assumed that the formation of a macroscale crack is the main dissipative mechanism and source of non-linearity. Further, it is assumed that the use of a scalar measure, e.g. a phase-field, can sufficiently describe this material degradation. This is generally not a fair assumption for 3D-woven composites. They can show nucleation and growth of subscale damage as well as extensive inelastic deformation prior to the formation and propagation of a macroscale crack. This is known as ductile fracture.

With ductile fracture, the energy functional no longer contains strictly an elastic contribution. For the constitutive relationship given by Equation (3.22), the corresponding energy density is

$$\Psi = (1 - d_s)\Psi_{os} + \Psi_{ps} + \sum_{I=1}^{3}(1 - d_I)\Psi_{oI} + \Psi_{pI}. \tag{4.29}$$

The elastic contributions are then

$$\Psi_{os} = \frac{1}{2}\boldsymbol{e}_{el} : \mathbb{E}_m : \boldsymbol{e}_{el}, \tag{4.30}$$

$$\Psi_{oI} = \frac{1}{2}\boldsymbol{\epsilon}_{el} : \mathbb{E}_{f,I} : \boldsymbol{\epsilon}_{el}, \tag{4.31}$$

while the plastic hardening contributions are denoted Ψ_{pI} and Ψ_{ps} in the reinforcement directions and shear respectively. For the **FiberDuk** material, according to the calibrated hardening responses in Table 3.3,

$$\Psi_{ps} = -\frac{\kappa_{sat,s}}{c_s}\left(c_s k_s - e^{(c_s k_s)} + 1\right), \tag{4.32}$$

$$\Psi_{p1} = \frac{1}{2}H_1 k_1^2, \tag{4.33}$$

$$\Psi_{p2} = \frac{1}{2}H_2 k_2^2. \tag{4.34}$$

A review of phase-field modelling of ductile fracture can be found in Alessi et al. [87]. But it is highlighted here, that in terms of degrading the energy density, there are two main options. The first, considered by for example Duda et al. [88] and Ambati et al. [89], degrade only the elastic part. As a consequence, the energy functional would take the form

$$E = \int_\Omega \left(g(\bar{d})\Psi_o + \Psi_p\right)\,\mathrm{d}\Omega. \tag{4.35}$$

Ambati et al. term this approach as *brittle fracture in elasto-plastic solids*. The yield surface and hardening modulus remain unaffected by the phase-field development. This in turn means that at some point the plastic strain saturate and the deformation becomes dominated by recoverable elastic strain. The next choice, and the one adopted in **Paper D** degrades the elastic and plastic contributions, see for example Miehe et al. [90] or Borden et al. [91]. Therefore,

$$E = \int_{\Omega} g(\bar{d}) \left[(1 - d_s)\Psi_{os} + \Psi_{ps} + \sum_{I=1}^{3} (1 - d_I)\Psi_{oI} + \Psi_{pI} \right] \mathrm{d}\Omega. \tag{4.36}$$

In the case of brittle fracture, the governing equations are formulated based on the minimisation of a potential energy. For ductile fracture however, Borden et al. [92] propose instead a microforce derivation of the governing equations in terms of a general energy potential. Following the later approach, the strong form of the governing equations for the model proposed in **Paper D** are

$$\nabla \boldsymbol{\sigma} + \boldsymbol{b} = 0 \quad \text{in} \quad \Omega \quad \text{and} \quad \boldsymbol{\sigma} \cdot \boldsymbol{n} = \bar{\boldsymbol{t}} \text{ on } \Gamma_t, \quad \boldsymbol{u} = \bar{\boldsymbol{u}} \text{ on } \Gamma_u \tag{4.37}$$

and

$$\frac{g_c}{l_c} \left(\bar{d} - l_c^2 \left(\nabla \otimes \nabla \bar{d} \right) : \boldsymbol{A}^d \right) = 2 \left(1 - \bar{d} \right) \mathcal{H}_{\Psi} \quad \text{and} \quad \boldsymbol{n} \cdot \boldsymbol{A}^d \cdot \nabla \bar{d} = 0 \text{ on } \Gamma. \tag{4.38}$$

In these equations, the internal body force, outward normal, traction and displacement field are denoted by $\boldsymbol{b}$, $\boldsymbol{n}$, $\boldsymbol{t}$ and $\boldsymbol{u}$ respectively. The constitutive stress strain relationship is expressed by

$$\boldsymbol{\sigma} = g(\bar{d}) \left((1 - d_s)\mathbb{E}_m : \boldsymbol{e}_{el} + \sum_{I=1}^{3} (1 - d_I)\mathbb{E}_{f,I} : \boldsymbol{\epsilon}_{el} \right). \tag{4.39}$$

4.4 Required Experimental Tests and Model Results

Calibrating the phase-field model extension proposed in **Paper D** requires characterising macroscale crack propagation in 3D-woven composites. More specifically, values must be determined for g_c, l_c, α_1, α_2, α_3 as well as the maximum strain values $\epsilon_{1,max}$, $\epsilon_{2,max}$, $\epsilon_{3,max}$ and γ_{max}. Dedicated experimental test results describing the failure of the **FiberDuk** or **BAM** material were not available over the course of the research project. However, test results available in the literature will be discussed. The assumptions made to obtain the material properties applied to the **FiberDuk** material in **Paper D** will also be introduced. These properties are summarised in Table 4.1.

Identification standards for the propagation of macroscopic cracks do exist for various materials. These materials include metals (ASTM E399 [93]) and plastics (ASTM D5045 [94]). More recently a test standard has even been proposed to characterise the translaminar fracture toughness of laminated composites (ASTM E1922 [95]). The test standards generally use specimens which induce stress gradients such as the compact tension (CT) and single-edge notched beam (SENB) test sample with the goal of identifying

the critical energy release rate g_c. Extending such test standards to 3D-woven composites is not straightforward, as the material is neither isotropic nor homogeneous.

A detailed experimental investigation and discussion concerning the estimation of the critical energy release rate of 3D-woven composites has been carried out by Médeau et al. [96]. Their experimental campaign tested CT specimens of various sizes on a highly unbalanced weave. Focus was therefore given to characterising failure in the weft direction, as this provides a clean and straight crack guided by the warp yarns running horizontally. It is also the weaker material axis and therefore provides a conservative measure of the critical energy release rate. The main highlight of the investigation carried out by Médeau et al., is the proof of invalidity of Linear Elastic Fracture Mechanics (LEFM) for 3D-woven composites. They noted that when the crack tip propagated a significant region containing different non-linearities could be observed. This in turn led to a size dependency on the measured g_c value which diverged from the LEFM solution as the specimen size was decreased.

The study carried out by Médeau et al. indicates that the traditional definition of g_c as a material parameter according to LEFM is not valid. In the present case, it is therefore proposed to allow for the local damage-plasticity model to account for the plasticity and initial (diffuse) damage development while letting the phase-field describe the localised damage development and final crack formation. To demonstrate the capabilities of this combination of damage models, a prototype value of $gc = 15$ kJ/m^2 is selected for the **FiberDuk** material. This estimation is based on the critical energy release rate reported by Pinho et al. [97] for tensile fibre failure of a laminated composite, and scaled according to the difference in stiffness. To determine α_1, α_2 and α_3 it is once again assumed that the critical energy release rate scales approximately with the stiffness in each reinforcement direction, i.e. $\alpha_1 = 1$ and $\alpha_2 = \alpha_3 = 0.25$.

Selecting an appropriate length scale parameter for a phase-field model is also a delicate task. The profile and width of the phase-field is determined directly by l_c. The argument can then be made that the length scale is a material parameter and is tied to a physical measure which relates to the phenomena controlling the failure of the composite. However, it is also shown by Médeau [66], that as l_c increases the apparent critical energy release rate, shown by a simulation, will be less than the value introduced into the model. As discussed by Bourdin et al. [75], this relates to Γ-convergence. For a sufficiently small l_c, the correct energy release rate will be displayed by the model. However, selecting a very small length scale parameter to guarantee Γ-convergence, is not a solution. In order to obtain mesh independent results, the discretisation must be fine enough to resolve the phase-field. Molnár and Gravouil [78] for example, recommend that the characteristic element length of the mesh $h < l_c/2$. To account for the discrepancies in the apparent g_c, Bourdin et al. [62] have also argued that a correction can be made such that g_c in Equation 4.7 is replaced with

$$g_c \rightarrow \left(1 + \frac{h}{4l_c}\right) g_c. \tag{4.40}$$

Due to a lack of experimental data and again, as a starting point for the development of the phase-field model in **Paper D**, the length scale parameter l_c is chosen to represent the approximate width of the horizontal weft yarns running transversely to the loading

direction in a tensile specimen loaded in the warp direction, i.e. $l_c = 2.5$ mm.

Finally, the maximum strain values used in the failure initiation criterion introduced in Equation (4.19) are selected based on the in-plane tensile and shear experimental results presented in Figure 2.3. In the case of tensile loading along the warp and horizontal weft yarns, the strain at failure can be read directly from the stress-strain curves where $\epsilon_{1,max} = 1.6\%$ and $\epsilon_{2,max} = 2.0\%$. In shear, the maximum strain value is selected as the point at which the stress-strain curve plateaus and large, visible shear cracks appear in the experiment. This corresponds to $\gamma_{max} = 15\%$. A promising avenue for determining an appropriate out-of-plane maximum strain $\epsilon_{3,max}$ value is once again to use a mesoscale analysis.

The phase-field model developed in **Paper D** has been implemented as a user element in Abaqus. The results from the implementation show a number of promising features. Figure 4.5 compares four different force displacement curves obtained for a model of the CT specimen shown in Figure 4.5a. Solid lines show the resulting force displacement behaviour using the anisotropic damage density function where either the warp (blue) or weft (red) yarns are oriented vertically in the loading direction. The material's higher elastic stiffness in the warp direction is clearly apparent when comparing the initial region of each curve before the load drop. Following the load drop, the effects of the anisotropic phase-field density function are noticeable. The lower effective energy release rate in the horizontal weft direction manifests itself as a steeper and more abrupt drop in load. Figure 4.5b also shows the resulting behaviour when a traditional isotropic crack density function is used. This is equivalent to setting $\boldsymbol{A}^d = \boldsymbol{I}$. In both cases the numerical values of g_c and l_c have been selected such that they are equivalent to the theoretical anisotropic properties.

It can be seen that, as the deformation progresses, the anisotropic density function gives behaviours which correspond well to the theoretical response obtained with an equivalent isotropic phase-field density function (for each separate load case). At the respective initial load drops however, there are considerable differences. Most likely, these differences are explained by the fact that the theoretical effective values produced by the anisotropic density function (i.e. Equation (4.21)) require the assumption that only the phase-field gradient running transversely to the crack growth direction is significant. However, in the case of an initial notch, from which the phase-field initiates and grows, this assumption is not valid.

Another noteworthy phenomenon that the model shows is the interaction of the plasticity and local damage models in a zone in front of the localised phase-field. Figure 4.6 displays a number of contour plots taken at different displacement values. Before the phase-field initiates at the notch tip, a process zone is apparent where both d_2 and k_2 show substantial growth. Further, this zone appears to advance ahead of the phase-field crack tip.

4.5 Limitations and Future Work

The largest limitation related to the development of the phase-field model in **Paper D** relates to the lack of experimental results. Dedicated tests to characterise macroscale crack

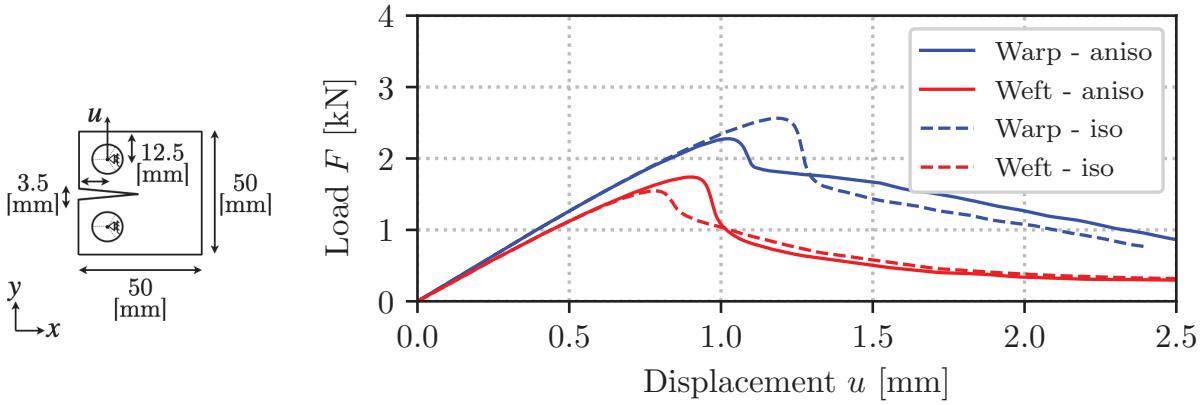

(a) *Boundary conditions and dimensions*

(b) *Force-displacement curves.*

Figure 4.5: *Comparison of the force-displacement curves for a CT specimen with both the anisotropic phase-field crack density function as well as an isotropic crack density function. For the isotropic density function g_c and l_c are chosen as the theoretical effective values $g_{c,I} = g_c\sqrt{\alpha_I}$ and $l_{c,I} = l_c\sqrt{\alpha_I}$.*

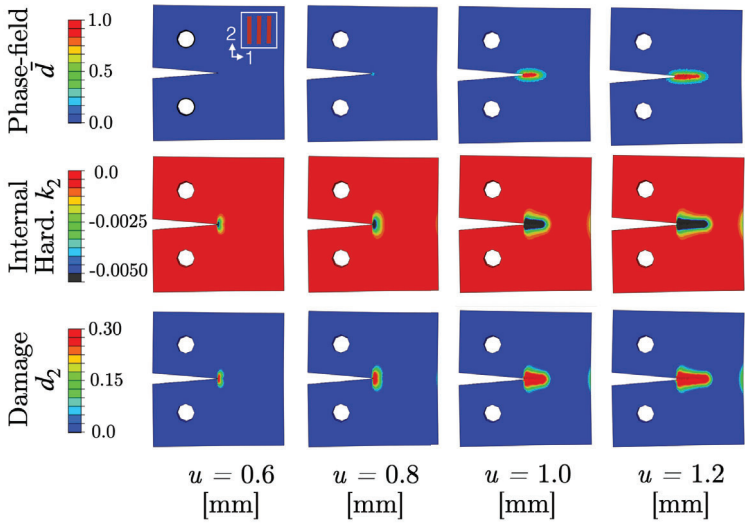

Figure 4.6: *Contour plots showing the development of different parameters at different displacement values for a compact tension specimen with the weft yarn running vertically using the anisotropic density function.*

Table 4.1: Parameters for the anisotropic phase-field model.

Phase-field	g_c	15 [kJ/m^2]	l_c	2.5 [mm]		
	$\alpha_1 1$	1 [-]	α_2	0.25 [-]	α_3	0.25 [-]
Maximum strain	$\epsilon_{1,max}$	1.6 [%]	$\epsilon_{2,max}$	2.0 [%]	γ_{max}	15 [%]

propagation in 3D-woven composites were not available. Nevertheless, the model shows promising characteristics. It has the ability to accommodate critical energy release rates that depend on the final mode of failure. The model also clearly shows the development of a propagating, diffuse damage and plasticity zone ahead of the crack.

A relatively simple maximum failure criterion is suggested to trigger the onset of the phase-field. Again, to propose improvements or modifications, further tests are required. The off-axis tests that will be carried out in the **VIRTEST-3D** project will help provide insight on how the interaction of tensile normal and shear loads affects the failure strain of the material. It should also be noted, that the maximum shear strain for the **FiberDuk** material in **Paper D** was estimated based on an Iosipescu shear test. This is not ideal, as in this test final failure is caused by the rotation and eventual rupture of reinforcement yarns. This type of phenomena can not be described in a small strain setting. A promising future development of the macroscale model would be an extension to a finite strain setting.

Even in the event that the theoretical value of g_c is known through experimental testing, it is challenging to implement an equivalent behaviour in a phase-field model. Linse et al. [98] show that discrepancies in the dissipated energy also stem from the consideration of test specimens with finite length, as well as the use of a history variable to enforce irreversibility of the phase-field. Instead they recommend an approach where the phase-field is simply fixed at a value close to one, once a threshold is reached.

Further, the model presented in **Paper D** has not been developed to handle compressive loading. Bourdin et al. [75] have shown that for isotropic materials, without further modifications, a phase-field model gives unrealistic crack patterns in compression. To avoid such situations, and prevent interpenetration of cracks in compression, the energy density is split and only the tensile component is used to drive the phase-field development. See for example Miehe et al. [63] or Moës et al. [99].

Standard phase-field models, as described in Section 4.2, will behave in a way that is representative of LEFM where the critical energy release rate can take on the traditional definition of a material parameter. The apparent dissipated energy will remain constant regardless of specimen size. The phase-field formulation presented in **Paper D** does however show a process zone ahead of the phase-field crack tip where the local damage and plasticity models evolve. A promising area for further development is determining whether or not such a model can mimic the size effects shown by Médeau et al. [96] for 3D-woven composites.

5 Conclusions and Outlook

Composite materials with 3D-woven reinforcements have shown a number of promising characteristics. In order to encourage their widespread adoption in industry however, efficient modelling techniques are needed. In terms of computational efficiency, macroscale models perform the best. They consider the material on a structural level as a homogeneous, anisotropic solid. This work has developed a macroscale phenomenologically based model to describe how 3D-woven composites deform and eventually fail under mechanical tensile and shear loads. This fulfills research objective number one. The non-linear deformation

behaviours of 3D-woven composites are due to a number of physical mechanisms. The development of the model framework has focused on capturing the mechanisms that lead to inelasticity and energy absorption. This took place in three main steps.

First, a modelling framework for 3D-woven composites was proposed and formulated based on an orthotropic stiffness tensor described using structural tensors. This framework divides the constitutive stress-strain relationship into four terms which govern either the shear behaviour of the material or the behaviour in each reinforcement direction. Further, the framework is thermodynamically consistent, general and flexible. It has also been shown that the framework for allows for various non-linear behaviours to be added in a modular fashion depending on loading direction.

As a second step, to determine an appropriate model formulation, the use of various constitutive modelling techniques was explored within the proposed framework. This included a viscoelastic approach (**Paper B**) as well as a combined elasto-plasticity and continuum damage approach (**Paper C**). The use of a viscoelastic model does allow for the prediction of rate-dependent material behaviour. However, to identify the required model parameters, experimental testing at multiple strain rates and/or creep or relaxation tests should be used. However, it can be concluded that given the cyclic experimental results that became available later in the project, the use of the combined elasto-plasticity and damage model shows the most promising results. In fact, using standard tensile and shear tests with unloading cycles made it possible to track both the development of permanent strain as well as stiffness reductions. The elasto-plasticity and damage model in particular, was developed in such a way that the damage and plasticity laws can be identified directly from the uniaxial cyclic stress–strain curves without the need for complex calibration schemes.

The third and final step involved the introduction of a phase-field model to capture failure initiation and softening of the constitutive response (**Paper D**). The model provided a regularisation of the localised damage, thereby avoiding any spurious mesh-dependence of the model. To activate the evolution of the phase-field, it was proposed that a criterion based on macroscopic strains be used. A strain-based criterion was selected based on the conclusion from **Paper A** that macroscopic strains are much more suitable than macroscopic stresses to represent the loading on the individual material constituents in a 3D-woven composite. Furthermore, the use of an anisotropic crack density function gives the possibility to tune the fracture toughness depending on loading mode. In a compact tension example the model also showed the development of a propagating, diffuse damage and plasticity zone ahead of the phase-field crack.

In order to facilitate knowledge transfer to industry, the developed models have been implemented in the commercial finite element software Abaqus. In the case of the viscoelastic model as well as the combined elasto-plastic and continuum damage model, this required the implementation of a user-material routine (UMAT). The phase-field extension on the other hand required the implementation of an Abaqus user-element (UEL).

A 10° off-axis tensile test was used to validate the model behaviour of both the viscoelastic approach as well as elasto-plastic and damage approach. This off-axis test induces a moderate combination of normal and shear loading on the specimen. In both cases, the model prediction showed good agreement to the experimental results. However,

to understand the applicability of the model to more complex multi-axial load cases, further testing is required. This will be explored in a future test campaign that will be carried out as part of the **VIRTEST-3D** project, where multiple off-axis angles will be considered. As a complement to such physical tests, this work explored the possibility to also include numerical results, obtained from mesoscale analyses, for the calibration and validation of the macroscale damage model. Preliminary results from **Paper E** indicate possibilities with such an approach, as demonstrated by the application to a 2D-woven composite material.

There are a number of promising avenues for the further development of the considered macroscale model. In order to predict the behaviour of large, structural components, the macroscale model must be able to describe the compressive behaviour of 3D-woven composites. This would require exploring the way permanent strains, stiffness reducing mechanisms, rate dependent behaviours and failure take place under compressive loading. Furthermore, although the current proposed model is considered to be sufficiently detailed to capture the observed behaviours in the experimental results that are available, its ability to predict damage and permanent strain growth under multiaxial loading scenarios remains to be investigated more in detail. In addition, carrying out a test campaign based on the so called *stepwise loading-unloading test with relaxation and retardation periods*, could also provide valuable information to understand how both rate-dependent and rate-independent constitutive models can be combined to describe the behaviour of 3D-woven composites. Initial testing has also shown that under some loading modes, e.g. in the Iosipescu shear test, the reinforcement yarns rotate and re-orient themselves. In the future a model extension to a finite strain setting could be considered to capture such behaviours.

References

[1] L. Tong, A. P. Mouritz, and M. K. Bannister. *3D Fibre Reinforced Polymer Composites*. Elsevier Science, 2002.

[2] F. Stig and S. Hallström. Assessment of the mechanical properties of a new 3D woven fibre composite material. *Composites Science and Technology* 69 (2009), 1686–1692.

[3] A. E. Bogdanovich. Advancements in manufacturing and applications of 3-D woven preforms and composites. *ICCM International Conferences on Composite Materials* (2007).

[4] N. Khokar, F. Winberg, and S. Hallström. Novel 3D preform architecture for performance and reliability of structural beams. *ICCM International Conferences on Composite Materials* (2015), 19–24.

[5] S. Kazemahvazi, N. Khokar, S. Hallstrom, H. N. Wadley, and V. S. Deshpande. Confluent 3D-assembly of fibrous structures. *Composites Science and Technology* 127 (2016), 95–105.

[6] A. P. Mouritz, M. K. Bannister, P. J. Falzon, and K. H. Leong. Review of applications for advanced three-dimensional fibre textile composites. *Composites Part A: Applied Science and Manufacturing* 30 (1999), 1445–1461.

[7] T. J. Whitney and T. Chou. Modeling of 3-D angle-interlock textile structural composites. *Journal of Composite Materials* 23 (1988), 890–911.
[8] E. De Luycker, F. Morestin, P. Boisse, and D. Marsal. Simulation of 3D interlock composite preforming. *Composite Structures* 88 (2009), 615–623.
[9] S. Nathan. *Positive reinforcement: 21st century 3D weaving*. 2015.
[10] T. Gereke and C. Cherif. A review of numerical models for 3D woven composite reinforcements. *Composite Structures* 209 (2019), 60–66.
[11] F. Stig. "A modelling framework for composites containing 3D reinforcement". PhD thesis. KTH Royal Institute of Technology, 2012.
[12] E. Mcmullin. *What do Physical Models Tell us?* Vol. 52. North-Holland Publishing Company, 1968, pp. 385–396.
[13] U. Kocks, C. N. Tomé, and H.-R. Wenk. *Plasticity Modeling in Minerals and Rocks*. Cambridge University Press, 2000, pp. 560–596.
[14] A. Spencer. *Continuum Theory of the Mechanics of Fibre-Reinforced Composites*. Springer-Verlag, 1984.
[15] B. Nedjar. A time dependent model for unidirectional fibre-reinforced composites with viscoelastic matrices. *International Journal of Solids and Structures* 48 (2011), 2333–2339.
[16] M. Vogler, R. Rolfes, and P. P. Camanho. Modeling the inelastic deformation and fracture of polymer composites-Part I: Plasticity model. *Mechanics of Materials* 59 (2013), 50–64.
[17] P. P. Camanho, A. Arteiro, A. R. Melro, G. Catalanotti, and M. Vogler. Three-dimensional invariant-based failure criteria for fibre-reinforced composites. *International Journal of Solids and Structures* 55 (2015), 92–107.
[18] S. Yushanov and A. Bogdanovich. Manufacturing and Property Analysis of a Novel Class of 3-D Woven Composites. *Journal of Thermoplastic Composite Materials* 12 (1999), 70–82.
[19] *ASTM D3039: Standard Test Method for Tensile Properties of Polymer Matrix Composite Materials*.
[20] *ISO 527-4: Plastics — Determination of Tensile Properties — Part 4: Test Conditions for Isotropic and Orthotropic Fibre-Reinforced Plastic Composites*.
[21] *AITM 1-0007: Fiber Reinforced Plastics - Determination of Plain, Open Hole and Filled Hole Tensile Strength*.
[22] *ASTM D5379: Standard Test Method for Shear Properties of Composite Materials by the V-Notched Beam Method*.
[23] *ASTM D7078: Standard Test Method for Shear Properties of Composite Material by V-Notched Rail Shear Method*.
[24] Y. M. Tarnopol'skii and T. Kinics. *Static Test Methods for Composites*. Van Nostrand Reinhold Company, 1981.
[25] K. B. Pettersson and J. M. Neumeister. A tensile setup for the IDNS composite shear test. *Composites Part A: Applied Science and Manufacturing* 37 (2006), 229–242.
[26] I. Topalidis, B. El Said, A. J. Thompson, J. Keulen, and S. R. Hallett. A numerical study of the effect of draping on the mechanical properties of 3D woven composites. *ICCM International Conferences on Composite Materials* (2019).

[27] E. M. Woo, J. C. Seferis, and R. S. Schaffnit. Viscoelastic characterization of high performance epoxy matrix composites. *Polymer Composites* 12 (1991), 273–280.
[28] S. Saseendran, M. Wysocki, and J. Varna. Evolution of viscoelastic behavior of a curing LY5052 epoxy resin in the glassy state. *Advanced Manufacturing: Polymer & Composites Science* 2 (2016), 74–82.
[29] L. Bardella. A phenomenological constitutive law for the nonlinear viscoelastic behaviour of epoxy resins in the glassy state. *European Journal of Mechanics, A/Solids* 20 (2001), 907–924.
[30] P. Haupt. *Continuum Mechanics and Theory of Materials*. Springer, 2002.
[31] H. Tresca. *Mémoires sur l'écoulement des corps solides*. Imprimerie Impériale, 1868.
[32] L. Kachanov. Time of the rupture process under creep conditions. *Nank S. S. R. Otd Tech Nauk* 8 (1958), 26–31.
[33] Y. Rabotnov. *Creep Problems in Structural Members*. North-Holland Publishing Company, 1969.
[34] I. Emri and N. W. Tschoegl. Generating line spectra from experimental responses. Part I: Relaxation modulus and creep compliance. *Rheologica Acta* 32 (1993), 311–322.
[35] J. F. Maire. "Etude théorique et expérimentale du comportement de matériaux composites en contraintes planes." PhD thesis. Université de Franche- Comté, 1992.
[36] R. Schapery. On the characterization of nonlinear viscoelastic materials. *Polymer Engineering and Science* 9 (1969), 295–310.
[37] S. Müller, M. Kästner, J. Brummund, and V. Ulbricht. A nonlinear fractional viscoelastic material model for polymers. *Computational Materials Science* 50 (2011), 2938–2949.
[38] M. Enelund, L. Mähler, K. Runesson, and B. L. Josefson. Formulation and integration of the standard linear viscoelastic solid with fractional order rate laws. *International Journal of Solids and Structures* 36 (1998), 2417–2442.
[39] F. Conejos, E. Balmes, B. Tranquart, E. Monteiro, and G. Martin. Viscoelastic homogenization of 3D woven composites with damping validation in temperature and verification of scale separation. *Composite Structures* 275 (2021), 114375.
[40] M. Hirsekorn, L. Marcin, and T. Godon. Multi-scale modeling of the viscoelastic behavior of 3D woven composites. *Composites Part A: Applied Science and Manufacturing* 112 (2018), 539–548.
[41] A. Hurmane, A. Mavel, P. Paulmier, and F. Laurin. Combined experimental and modelling approaches for strength analysis of 3D woven composites: from elementary coupons to complex aeronautical structures. *AerospaceLab Journal* 12 (2016), 1–11.
[42] F. Norton. *The Creep of Steels at High Temperatures*. McGraw-Hill Book Company, 1929.
[43] J. Nelder and R. Mead. A Simplex Method for Function Minimization. *The Computer Journal* 7 (1965), 308–313.
[44] P. Grassl and M. Jirásek. Damage-plastic model for concrete failure. *International Journal of Solids and Structures* 43 (2006), 7166–7196.

[45] S. V. Lomov, D. S. Ivanov, I. Verpoest, M. Zako, T. Kurashiki, H. Nakai, and S. Hirosawa. Meso-FE modelling of textile composites: Road map, data flow and algorithms. *Composites Science and Technology* 67 (2007), 1870–1891.

[46] S. D. Green, M. Y. Matveev, A. C. Long, D. Ivanov, and S. R. Hallett. Mechanical modelling of 3D woven composites considering realistic unit cell geometry. *Composite Structures* 118 (2014), 284–293.

[47] B. El Said, F. Daghia, D. Ivanov, and S. R. Hallett. An iterative multiscale modelling approach for nonlinear analysis of 3D composites. *International Journal of Solids and Structures* 132-133 (2018), 42–58.

[48] P. Ladeveze and E. LeDantec. Damage modelling of the elementary ply for laminated composites. *Composites Science and Technology* 43 (1992), 257–267.

[49] E. S. Shin and K. D. Pae. Effects of Hydrostatic Pressure on In-Plane Shear Properties of Graphite/Epoxy Composites. *Journal of Composite Matérials* 26 (1992), 828–868.

[50] A. D. Hasanyan. "Nonlinear Micropolar Models for Composite Materials: Theory and Computation". PhD thesis. University of Michigan, 2018.

[51] M. Zscheyge, R. Böhm, A. Hornig, J. Gerritzen, and M. Gude. Rate dependent non-linear mechanical behaviour of continuous fibre-reinforced thermoplastic composites – Experimental characterisation and viscoelastic-plastic damage modelling. *Materials and Design* 193 (2020), 108827.

[52] F. Laurin, V. Medeau, S. Mousillat, and J. Rannou. "Damage and strength prediction of 3D woven composite structures: experimental characterization, size effect and modelling". *9th International Conference on Composites Testing and Model Identification*. Luleå, Sweden, 2019.

[53] M. Jirásek and Z. Bažant. *Inelastic Analysis of Structures*. John Wiley & Sons Ltd, 2002.

[54] N. S. Ottosen and R. Matti. *The Mechanics of Constitutive Modeling*. Elsevier Ltd, 2005.

[55] P. Ladevèze. A damage computational method for composite structures. *Computers and Structures* 44 (1992), 79–87.

[56] Z. Bažant and B. Oh. Crack band theory for fracture of concrete. *Matériaux et construction* 16.3 (1983), 155–177.

[57] S. Mukhopadhyay and S. R. Hallett. A directed continuum damage mechanics method for modelling composite matrix cracks. *Composites Science and Technology* 176 (2019), 1–8.

[58] K. H. Leong, J. Zhi, H. P. Lee, V. B. Tan, and T. E. Tay. Adaptive multi-fidelity (AMF) modelling of progressive damage in notched composite laminates. *Composites Part A: Applied Science and Manufacturing* 154 (2022), 106790.

[59] J. Främby and M. Fagerström. An adaptive shell element for explicit dynamic analysis of failure in laminated composites Part 2: Progressive failure and model validation. *Engineering Fracture Mechanics* 244 (2021), 107364.

[60] G. Pijaudier-Cabot and Z. P. Bazant. Nonlocal damage theory. *Journal of Engineering Mechanics* 113 (1987), 1512–1533.

[61] R. H. J. Peerlings, R. de Borst, W. . M. Brekelmans, and J. H. P. de Vree. Gradient enhanced damage for quasi-brittle materials. *International Journal for Numerical Methods in Engineering* 39 (1996), 3391–3403.

[62] B. Bourdin, G. A. Francfort, and J. J. Marigo. The variational approach to fracture. *Journal of Elasticity* 91 (2008), 5–148.

[63] C. Miehe, F. Welschinger, and M. Hofacker. Thermodynamically consistent phase-field models of fracture: Variational principles and multi-field FE implementations. *International Journal for Numerical Methods in Engineering* 83 (2010), 1273–1311.

[64] R. de Borst and C. V. Verhoosel. Gradient damage vs phase-field approaches for fracture: Similarities and differences. *Computer Methods in Applied Mechanics and Engineering* 312 (2016), 78–94.

[65] L. Marcin. "Modélisation du comportement, de l'endommagement et de la rupture de matériaux composites à renforts tissés pour le dimensionnement robuste de structures". PhD thesis. Université Bordeaux, 2010.

[66] V. Médeau. "Rupture des composites tissés 3D : de la caractérisation expérimentale à la simulation robuste des effets d'échelle". PhD thesis. Université De Toulouse, 2019.

[67] A. T. Zehnder. "Griffith Theory of Fracture". *Encyclopedia of Tribology*. Ed. by Q. J. Wang and Y.-W. Chung. Boston, MA: Springer US, 2013, pp. 1570–1573.

[68] J.-Y. Wu, V. P. Nguyen, C. T. Nguyen, and D. Sutula. Phase field modelling of fracture. *Advances in Applied Mechanics* 53 (2020), 1–183.

[69] L. Ambrosio and V. M. Tortorelli. Approximation of functional depending on jumps by elliptic functional via t-convergence. *Communications on Pure and Applied Mathematics* 43 (1990), 999–1036.

[70] B. Bourdin, C. J. Larsen, and C. L. Richardson. A time-discrete model for dynamic fracture based on crack regularization. *International Journal of Fracture* 168 (2011), 133–143.

[71] C. Kuhn, A. Schlüter, and R. Müller. On degradation functions in phase field fracture models. *Computational Materials Science* 108 (2015), 374–384.

[72] K. Pham, H. Amor, J.-J. Marigo, and C. Maurini. Gradient damage models and their use to approximate brittle fracture. *International Journal of Damage Mechanics* 20 (2011), 618–652.

[73] B. Bourdin, J.-J. Marigo, C. Maurini, and P. Sicsic. Morphogenesis and Propagation of Complex Cracks Induced by Thermal Shocks. *Phys. Rev. Lett.* 112.1 (Jan. 2014), 14301.

[74] J. Y. Wu. A unified phase-field theory for the mechanics of damage and quasi-brittle failure. *Journal of the Mechanics and Physics of Solids* 103 (2017), 72–99.

[75] B. Bourdin, G. A. Francfort, and J. J. Marigo. Numerical experiments in revisited brittle fracture. *Journal of the Mechanics and Physics of Solids* 48 (2000), 797–826.

[76] A. Karma, D. A. Kessler, and H. Levine. Phase-Field Model of Mode III Dynamic Fracture. *Phys. Rev. Lett.* 87 (July 2001), 45501.

[77] C. Miehe, M. Hofacker, and F. Welschinger. A phase field model for rate-independent crack propagation: Robust algorithmic implementation based on operator splits. *Computer Methods in Applied Mechanics and Engineering* 199 (2010), 2765–2778.

[78] G. Molnár and A. Gravouil. 2D and 3D Abaqus implementation of a robust staggered phase-field solution for modeling brittle fracture. *Finite Elements in Analysis and Design* 130 (2017), 27–38.

[79] V. D. Azzi and S. W. Tsai. Anisotropic strength of composites. *Experimental Mechanics* 5 (1965), 283–288.

[80] S. W. Tsai and E. M. Wu. A general theory of strength for anisotropic materials. *Journal of Composite Materials* 5 (1971), 58–80.

[81] R. G. Cuntze and A. Freund. The predictive capability of failure mode concept-based strength criteria for multidirectional laminates. *Composites Science and Technology* 64 (2004), 343–377.

[82] S. T. Pinho, R. Darvizeh, P. Robinson, C. Schuecker, and P. P. Camanho. Material and structural response of polymer-matrix fibre-reinforced composites. *Journal of Composite Materials* 46 (2012), 2313–2341.

[83] N. Carrere, F. Laurin, and J. F. Maire. Micromechanical-based hybrid mesoscopic three-dimensional approach for non-linear progressive failure analysis of composite structures - Part B: Comparison with experimental data. *Journal of Composite Materials* 47 (2013), 743–762.

[84] J. Bleyer and R. Alessi. Phase-field modeling of anisotropic brittle fracture including several damage mechanisms. *Computer Methods in Applied Mechanics and Engineering* 336 (2018), 213–236.

[85] A. Dean, P. K. Asur Vijaya Kumar, J. Reinoso, C. Gerendt, M. Paggi, E. Mahdi, and R. Rolfes. A multi phase-field fracture model for long fiber reinforced composites based on the Puck theory of failure. *Composite Structures* 251 (2020), 112446.

[86] S. Teichtmeister, D. Kienle, F. Aldakheel, and M. A. Keip. Phase field modeling of fracture in anisotropic brittle solids. *International Journal of Non-Linear Mechanics* 97 (2017), 1–21.

[87] R. Alessi, M. Ambati, T. Gerasimov, S. Vidoli, and L. De Lorenzis. "Comparison of phase-field models of fracture coupled wiht plasticity". *Advances in Computational Plasticity*. Springer, 2018, pp. 1–22.

[88] F. P. Duda, A. Ciarbonetti, P. J. Sánchez, and A. E. Huespe. A phase-field/gradient damage model for brittle fracture in elastic-plastic solids. *International Journal of Plasticity* 65 (2014), 269–296.

[89] M. Ambati, T. Gerasimov, and L. De Lorenzis. Phase-field modeling of ductile fracture. *Computational Mechanics* 55.5 (2015), 1017–1040.

[90] C. Miehe, M. Hofacker, L. M. Schänzel, and F. Aldakheel. Phase field modeling of fracture in multi-physics problems. Part II. Coupled brittle-to-ductile failure criteria and crack propagation in thermo-elastic-plastic solids. *Computer Methods in Applied Mechanics and Engineering* 294 (2015), 486–522.

[91] M. J. Borden, T. J. Hughes, C. M. Landis, A. Anvari, and I. J. Lee. A phase-field formulation for fracture in ductile materials: Finite deformation balance law derivation, plastic degradation, and stress triaxiality effects. *Computer Methods in Applied Mechanics and Engineering* 312 (2016), 130–166.

[92] M. Borden, T. Hughes, C. Landis, A. Anvari, and I. Lee. "Phase-Field Formulation for Ductile Fracture". *Advances in Computational Plasticity*. Springer, 2018, pp. 45–70.

[93] *ASTM E399: Standard Test Method for Linear-Elastic Plane-Strain Fracture Toughness of Metallic Materials.*

[94] *ASTM D5045: Standard Test Methods for Plane-Strain Fracture Toughness and Strain Energy Release Rate of Plastic Materials.*

[95] *ASTM E1922: Standard Test Method For Translaminar Fracture Toughness Of Laminated And Pultruded Polymer Matrix Composite Materials.*

[96] V. Médeau, F. Laurin, J. Rannou, A. Hurmane, H. Quillent, and F. Lachaud. Robust characterization of crack propagation in 3D woven composites and evidences of size dependency. *Composite Structures* 225 (2019), 111175.

[97] S. T. Pinho, P. Robinson, and L. Iannucci. Fracture toughness of the tensile and compressive fibre failure modes in laminated composites. *Composites Science and Technology* 66 (2006), 2069–2079.

[98] T. Linse, P. Hennig, M. Kästner, and R. de Borst. A convergence study of phase-field models for brittle fracture. *Engineering Fracture Mechanics* 184 (2017), 307–318.

[99] N. Moës, C. Stolz, P.-E. Bernard, and N. Chevaugeon. A level set based model for damage growth: The thick level set approach. *International Journal for Numerical Methods in Engineering* 86 (2011), 358–380.

[100] S. W. Tsai and E. M. Wu. A General Theory of Strength for Anisotropic Materials. *Journal of Composite Materials* 5 (1971), 58–80.

[101] L. Tong, P. Tan, and G. P. Steven. Effect of yarn waviness on strength of 3D orthogonal woven CFRP composite materials. *Journal of Reinforced Plastics and Composites* 21 (2002), 153–173.

[102] C. Kuhn, T. Noll, and R. Müller. On phase field modeling of ductile fracture. *GAMM Mitteilungen* 39.1 (2016), 35–54.